Electrode Arrays, Test Fixture, and System Concept for High-Bandwidth Capacitive Imaging

by

Tyler Thomas Hamer

S.B., Massachusetts Institute of Technology (2014)

Submitted to the Department of Mechanical Engineering
in partial fulfillment of the requirements for the degree of

Master of Science in Mechanical Engineering

at the

MASSACHUSETTS INSTITUTE OF TECHNOLOGY

February 2017

Author .....
Department of Mechanical Engineering
January 15, 2016

Certified by .....
David L Trumper
Professor
Thesis Supervisor

Certified by .....
Jeffrey H Lang
Professor
Thesis Supervisor

Accepted by .....
Rohan Abeyaratne
Chairman, Department Committee on Graduate Theses
Graduate Officer

Electrode Arrays, Test Fixture, and System Concept for High-Bandwidth Capacitive Imaging

by

Tyler Thomas Hamer

Submitted to the Department of Mechanical Engineering
on January 15, 2016, in partial fulfillment of the
requirements for the degree of
Master of Science in Mechanical Engineering

Abstract

Spot defects are a leading source of failure in the fabrication of integrated circuits (ICs). Thus, the IC industry inspects for defects at multiple stages of IC fabrication, especially the fabrication of IC photomasks. However, existing non-invasive imaging methods cannot image a modern photomask in a reasonable time-frame. Electroquasistatic (EQS) sensors are arrays of electrode pairs that capacitively couple to targets they sweep over. Utilizing high measurement frequencies and a number of parallel scanning electrode pairs, EQS sensors have been suggested as a potential high speed alternative for defect detection in IC fabrication.

This thesis continues the investigation into EQS sensors for high speed imaging by exploring EQS sensors driven with high excitation frequencies. We develop electrode arrays that can be driven with high excitation frequencies and construct high frequency EQS sensors by attaching them to high frequency drive electronics. We also fabricate a test fixture for positioning these sensors relative to and sweeping them across targets on a conductive base. As the sensors sweep across targets, their impedance is measured from 1 - 500 MHz using an impedance analyzer and is later converted into the capacitance between the sensor's electrode array and the target. Capacitance changes are produced by a variable air gap and by a dielectric step, confirming these sensors can detect changes in a target's geometric and material properties with high excitation frequencies. Finally, we present concepts for a high speed measurement system which utilizes these sensors.

Thesis Supervisor: David L Trumper
Title: Professor

Thesis Supervisor: Jeffrey H Lang
Title: Professor

Acknowledgments

Without the help and support of so many people, this project would not have been possible. As a result, I would like to take this opportunity to thank those who aided me in this endeavor.

I would like to thank my advisors on this project, Prof. David Trumper and Prof. Jeff Lang. Both of them have not only been an incredible source of knowledge, but also incredible sources of inspiration and guidances for both this project and life in general. Under them, I have learned to simultaneously consider the small-and big-picture when approaching a problem so that no detail maybe overlooked. Further, they've taught me how to maintain integrity despite hardships that can arise along the way.

In addition, I want to thank Dr. Theodore Lyszczarz from MIT Lincoln Laboratory and our lab's administrator, Laura Zaganjori. Both of them helped me obtain equipment for the project which I am extremely thankful for. Further, Dr. Lyszczarz's input was invaluable in navigating the RF (Radio Frequency) domain.

I want to give special thanks to Rakesh Kumar who I worked side-by-side with me on this project and Matthew D'Asaro who shared his love and knowledge of radio frequency equipment. Rakesh did a tremendous job designing the drive electronics for the EQS sensors and modeling the sensors. Rakesh and I spent quite a few hours together in front of the impedance analyzer which I will not forget. Matt identified and helped specify equipment we needed, allowing this project moving forward.

I would also like to thank my lab mates for their support and friendship. Despite having done my undergraduate studies at MIT, I was still quite lost when I first joined the Precision Motion Control Lab. Jun Young Yoon was an unbelievable help in getting settled in the lab and always a source of encouragement and help afterwards. Lei Zhou, Minkyun Noh, and Brij Bhushan have always been there for me, from tossing ideas around and helping me figure stuff out to just having a good laugh. Lei is such a joy to be around and is always happy to take time out of her day to explain things to me. Minkyun has told me so many stories from his master's studies and has

given me so much encouragement in finishing mine. Brij has constantly pushed me to be a better engineer. All the questions he has asked have allowed me to fine tune my understanding in engineering. Luis Soenksen has been a great friend and a great inspiration. I cannot thank him enough for his advice in writing papers and studying for quals with me. As I write this, I look forward to seeing you on the other side of that. Lastly, Philip Daniel was great to TA 2.14/2.140 with. I'll always remember getting lunch and trying to figure out what the resistor across the input terminals of op amp circuit did in the second quiz.

Lastly I want to thank my friends and family. Aaron Ramirez, Alex Flores, Alex Hahn, Alicia Glazia, Anton Hunt, Brady Enstad, Charles Guan, Charlie Wheeler, Chris Merian, Chris Poulton, Chris Sarna, Daniel Gonzalez, David Luciano, Erica Waller, Hugh Berglind, Ido Efrati, Jack Greenfield, Jamison Go, Jeremy Kaplan, Jeremy Wright, Jaswanth Madhavan, Jaz Harris, Jonny Slocum, Jordan Ugalde, Josh Nation, Josh Wiens, Kalin Malouf, Keith Martinez, Lukas Porz, Madeline Jenkins, Marcel Thomas, Max Ockner, Mia Stevens, Mic Byrne, Mike Zakarian, Natalie Dostie, Neerja Aggarwal, Nick Demas, Rebecca Li, Robert Hummel, Sandy Bayona, Sarah Mayner, Shawn Zhang, Steven Guitron, Stuart Baker, Tylor Hess, Victor Gutierrez, Xinkun Sheena Nie, Zaid Zayyad, and Zachary Decker all kept me sane during this project. Without such good friends, I'm not quite sure I would have survived. My siblings Robert and April were constant sources of love and support, reminding me how lucky am I to be in such a loving family. Lastly, my parents were not just sources of love, but also the reason this was all possible. My love of learning and ability to sink hours of hard work into a project comes from them and for that I am forever grateful.

Contents

List of Figures

List of Tables

Chapter 1

Introduction

Opens and shorts caused by spot defects are a leading source of failure in the fabrication of integrated circuits (ICs) [1]. To address spot defects, the IC industry uses two approaches simultaneously. First, the IC industry has developed and uses a set of geometric rules for making ICs more tolerant to spot defects [2]. Second, the IC industry inspects for defects at multiple stages during IC fabrication. One stage of particular importance to scan for defects is during the fabrication of IC photomasks [3]. A fatal defect in a photomask will cause every IC produced from it to fail. However the two primary methods of non-invasive imaging, Atomic Force Microscopy (AFM) and Scanning Capacitance Microscopy (SCM), cannot image a modern photomask in a reasonable time-frame.

Recent investigations into electroquasistatic (EQS) sensors suggests that EQS sensors maybe capable of detecting contaminant particles on a photomasks [4] and thus could be used as a potential high speed alternative for detecting defects. This thesis, in conjunction with Rakesh Kumar's Masters thesis [5], continues the investigation of EQS sensors as an alternative imaging method for detecting defects in the fabrication of ICs. In particular, this thesis presents the design and fabrication of electrode arrays that can be driven with high excitation frequencies and thus could potentially image a target at high-bandwidth. Rakesh Kumar presents the electronics for driving these electrode arrays at high frequencies. The design and development of test fixtures for testing EQS sensors constructed from these electrode arrays and their high

frequency drive electronics are presented here. Experiments conducted jointly with Rakesh Kumar show these EQS sensors are able to detect changes in the material and geometric properties of a scanned target using high excitation frequencies. However, these studies have not been conducted at high-bandwidth, due to impedance analyzer throughput limitations. Finally, a concept for a high-bandwidth imaging system utilizing these EQS sensors is presented.

1.1 Existing Imaging Methods

Two of the methods that the IC industry currently uses for scanning modern photomasks are Atomic Force Microscopy (AFM) and Scanning Capacitance Microscopy (SCM) [6, 7]. First developed at Stanford in 1986 by Binnig and Quate [8], AFM systems work by monitoring the force between a sharp-tipped cantilever beam (stylus) and a target. To create an image, a statically deflected (contact mode) or oscillating (tapping mode) stylus is moved over the surface of a target. As the target's surface changes, the stylus deflects different amounts in the static case or the oscillations of the stylus change in amplitude and/or frequency in the oscillating case. Originally these deflections or changes in oscillation were detected by a scanning tunneling microscope (STM) [8], but are today, typically detected by reflecting a weak laser off the back of the stylus into photodiodes to form an optical lever [9]. Finally these deflections or changes in oscillation are related back to force or force gradient respectively, using the stiffness of the stylus, and used to create a topographical image of the target. Using this method, AFM systems are able to achieve scan speeds up to 0.6 mm/s [10].

SCM systems, first developed at RCA Laboratories in 1984 by Matey and Blanc from a modified RCA VideoDisc player, work by monitoring the capacitance between an electrode and a target [11, 12]. As the electrode sweeps over the target, changes in the target's topography and material properties create changes in the capacitance between the electrode and target. The capacitance between the electrode and target is part of a resonant circuit whose center frequency shifts as the capacitance changes;

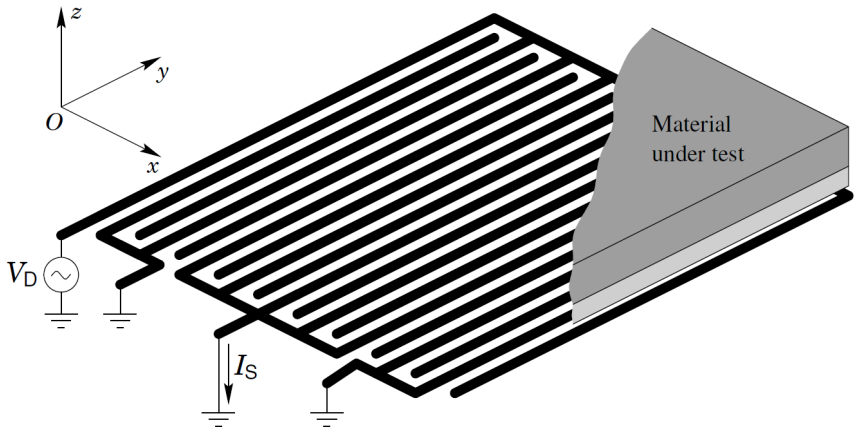

Figure 1-1: Generic EQS sensor adapted from [4] [14].

thus changes in capacitance produce shifts in the center frequency. These shifts in the center frequency produce a varying voltage in a detector which is then turned into a topographical image or image of changing material properties of the target [13]. This allows SCM systems to achieve scan speeds up to 5 m/s [12].

1.2 Electroquasistatic (EQS) Imaging

We define electroquasistatic (EQS) sensors as arrays of coplanar electrode pairs. One set of electrodes is driven by a known voltage or current and an induced corresponding current or voltage is measured on the other set of electrodes in the electrode pairs. Figure 1-1 shows a generic EQS sensor with one set of electrodes driven at voltage V_{D} and current I_{s} is measured from the other set of electrodes. The voltage and current are related by the capacitance between the two sets of electrodes. The capacitance is dependent on the geometric and material properties of the substrate the electrode's electric field passes through. Consider an ideal parallel plate capacitor with electrodes of area A, separated by distance d. Its capacitance is

$$C = \frac{\epsilon_{\mathrm{r}}\epsilon_{\mathrm{o}}A}{d}, \tag{1.1}$$

where ϵ_{o} is the permittivity of free space, and ϵ_{r} is the relative permittivity of an intervening substrate. In the case of coplanar electrodes in EQS sensors, the electric

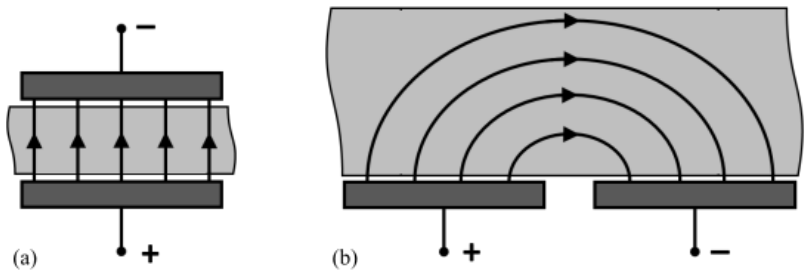

Figure 1-2: Electric field lines passing through a substrate (a) between the electrodes of a parallel plate capacitor and (b) surrounding the electrodes of a coplanar electrode pair in an EQS sensor.

field resembles a fringe field as shown in Figure 1-2, and so has a more complex relationship for capacitance. In particular, the capacitance between two electrodes of an EQS sensor depends on the penetration of the substrate surrounding them.

In 1982 at MIT, Senturia et al realized the dependence of coplanar electrodes' capacitance on the substrates surrounding the electrodes provided a convenient way to measure dielectrics and introduced EQS sensors for the first time under the name microdielectrometry sensors [15]. These initial EQS sensors used interdigitated PCB traces as electrodes and were used to measure the dielectric properties of thin films coated directly on the sensor. Later in 1988, Zaretsky conducted work on modeling EQS sensors and estimating parameters from their measured capacitance for use in electrical transformer monitoring. This modeling revealed that the depth of penetration of an EQS sensor is determined by the sensor's spatial frequency, the distance between the centers of two electrodes of the same charge, as shown in Figure 1-3 [16]. Based on this relationship between electrode spacing and depth of penetration, multiple sized EQS sensors were used together to estimate material properties such as moisture content [17, 18] and permittivity [19] at multiple depths in a substrate. In addition, macroscale EQS sensors were used to detect landmines at different depths [20]. Recently, polar interdigitated electrode arrays have been considered [14] and the use of high speed EQS sensors for imaging surface and subsurface defects in IC fabrication has been proposed [4, 21].

Using EQS sensors for imaging would work very similar to SCM systems. As the EQS sensor sweeps over the target, changes in the target's topography and material

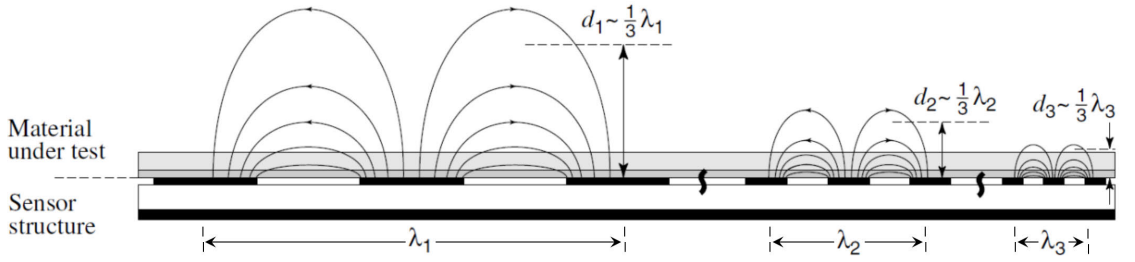

Figure 1-3: EQS sensors with multiple spatial wavelength coplanar electrode sets, adapted from [4] [14]. The electric field of each electrode set penetrates the target a fraction of the spatial wavelength, potentially allowing for sub-surface imaging.

properties create changes in the capacitance. These changes in capacitance are then picked up by a capacitance measurement circuit and then converted into an image. The main difference is that in SCM imaging, the target acts as the counterpart to the SCM electrode in forming a capacitor whereas in EQS imaging, the target acts as the dielectric of the capacitor formed by the electrode array.

1.3 Comparison of Existing Imaging Methods and EQS Imaging

EQS imaging has several potential benefits compared to AFM and SCM imaging. First, EQS imaging has the potential to image at much higher throughput. As an example of a measurement task, consider a 100 mm × 100 mm photomask with 100 nm × 100 nm sized features. To capture each feature, an image of the photomask would comprise 10^{12} pixels. Given the scan time is

$$T_{\text{Scan}} = \frac{N_{\text{Pixels}}}{N_{\text{Probes}}} \frac{l_{\text{Pixel}}}{v_{\text{Scan}}}, \tag{1.2}$$

where N_{Pixels} is the total number of photomask pixels, l_{Pixel} is the pixel size, N_{Probes} is the number of parallel scanning probe heads, and v_{Scan} is the scan speed, the fastest AFM and SCM systems would take in principle, 5.3 years [10] and 5.6 hours [12, 13] respectively, to scan the photomask.

Table 1.1: Example IC Mask Scan Times for Various Imaging Systems

Imaging System	N_{Probe}	$f_{\text{Excitation}}$ [MHz]	T_{Measure}^{-1} [MHz]	v_{Scan} [mm/s]	T_{Scan}
AFM	1	0.6	0.06	0.6	5.3 yrs
SCM	1	915	20	5000	5.6 hrs
EQS	1	1000	10	100	11.6 days
EQS	100	1000	10	100	2.8 hrs
EQS	1	10^4	100	1000	27.8 hrs
EQS	100	10^4	100	1000	16.7 mins

In order to reduce the scan time, a combination of increased scan speed and the number of parallel scanning probe heads is needed. However, the scan speeds used are the current maximum for AFM and SCM systems. As for increasing the number of probes, the concept has fairly recently been considered for AFM systems [22, 23, 24]. On the other hand, EQS sensors can take advantage of both of these strategies. To calculate the scan speed of an EQS imaging system, each pixel is assumed to be imaged under quasistatic conditions,

$$1 \text{ Pixel} \gg \frac{v_{\text{Scan}} \cdot T_{\text{Measure}}}{l_{\text{Pixel}}}, \tag{1.3}$$

where T_{Measure} is the single-probe pixel imaging time. Based on the noise levels in SCM systems [12, 13], T_{Measure} can be estimated as one hundredth of the inverse of the EQS imaging system's excitation frequency, $f_{\text{Excitation}}$. Thus by using an excitation frequency near or into the GHz range, EQS sensors could in principle achieve high scan speeds. In addition, through MEMS fabrication, EQS sensors can potentially be made with hundreds of probes. With this combination of high scan speeds and multiple probes, EQS imaging might reduce the time it takes to scan a photomask to the order of hours. Table 1.1 evaluates T_{Scan} for the example photomask for the various imaging systems. Note that in completing Table 1.1 for EQS imaging, it is assumed that satisfying (1.3) by a factor of 10 is sufficient.

Another benefit of EQS imaging over AFM and SCM imaging is the potential ability to perform sub-surface imaging. The depth an electrode pair can penetrate to

is related to the spacing between electrodes. Thus by using multiple electrode pairs with different spacing, EQS sensors can in principle image multiple depths of a target. Even with multiple probes, AFM and SCM systems can only measure interactions betweens the target's surface and each probe head, reducing the scan time, but only providing imaging of near-surface material properties.

Lastly, EQS imaging systems only require access to one side of the target. The target just needs to be close enough to the electrode array such that the electric field passes through the target and capacitively couples it to the array. SCM imaging on the other hand requires access to both sides of the target as the far side to the target needs to be grounded. This EQS system advantage simplifies the setup needed to image a target.

1.4 Thesis Scope

The scope of this thesis is to examine the potential use of EQS sensors for high-bandwidth imaging. This examination can be broken into the following objectives:

1. Design and fabricate electrode arrays capable of imaging with high excitation frequencies.

2. Attach these electrode arrays to drive/sense electronics to create high frequency EQS sensors.

3. Develop a test fixture for micron-scale positioning of the EQS sensors relative to a base, bringing the the EQS sensors in coplanar alignment with the base, and sweeping the EQS sensor over targets mounted to the base.

4. Detect changes in capacitances due to changes in the target's material and geometric properties using high excitation frequencies.

5. Propose a high speed scanning and measurement system to use the EQS sensors to potentially image at high speeds.

1.5 Thesis Summary

This first chapter presented the use of Electroquasistatic (EQS) sensors as an alternative method to Atomic Force Microscopy (AFM) and Scanning Capacitance Microscopy (SCM) for surface and sub-surface defect detection during the fabrication of integrated circuits. First, operating principles for AFM and SCM systems work were presented followed by the operating principles for and the history of EQS sensors. The advantages of EQS imaging over AFM and SCM imaging were shown along with the time it would take each of these systems to scan an example IC photomask. These scan times are summarized in Table 1.1. Lastly, the objectives of this thesis were given and each chapter summarized.

Chapter 2: Design & Fabrication of Macro-Scale EQS Electrode Arrays discusses the development of electrode arrays that can be driven with high excitation frequencies. This begins with an overview of how an electrode array should work and the design requirements it should satisfy. An electrode array constructed from the traces of the high frequency drive electronics PCB is reviewed. Due to poor performance of this electrode array, a simpler, unguarded electrode array made from two strips of wire is presented. Building on the success of this simpler electrode array, two variable spatial wavelength electrode arrays are fabricated. Finally, the minimum resolution of these electrode arrays is considered. Chapter 3: Design and Layout of Sensor Drive Electronics of Rakesh Kumar's Master Thesis presents the high frequency drive electronics these electrodes need to become high frequency EQS sensors [5].

Chapter 3: Initial Test Fixture Design and Testing presents a test fixture for positioning the EQS sensors within microns relative to an aluminum base. First the design of the test fixture is presented. Then the test fixture is used to move an EQS sensor away from the base to verify that the sensor can measure changes in the thickness of an air gap target. Next the test fixture sweeps an EQS sensor across a dielectric step and the sensor is used to detect a change in dielectric. The sensor successfully detects a change in thickness and a change in dielectric, but also detects tilt between itself and the aluminum base. These two experiments are done jointly

with Rakesh Kumar [5].

Chapter 4: Final Test Fixture Design and Testing presents a redesign and testing of the test fixture to mitigate misalignments between the EQS sensors and the aluminum base. Detectable sources of misalignment between the sensors and base are explained. Then a redesign of the test fixture to mitigate these sources of misalignment is presented. This redesigned test fixture is used to sweep both variable spatial wavelength EQS sensors horizontally and vertically across the base; the amount of horizontal and vertical tilt is measured with these sensors. The redesign of the test fixture drastically reduces the tilt between the sensors and the base.

In Chapter 5: Scanning Experiments & Results, the variable spatial wavelength EQS sensors and redesigned test fixture are used to measure a variable air gap and change in dielectric a second time. These experiments are done jointly with Rakesh Kumar [5]. The EQS sensors successfully measure the variable air gap and change in dielectric. However, drastically less tilt is detected than in the previous experiments.

Chapter 6: Concept for High Speed Imaging System discusses potential components for using the EQS sensors for high-bandwidth imaging. A concept for the hardware needed for driving and reading the capacitance measured by the sensors at high frequencies is reviewed. Following this, a concept for positioning and sweeping the sensors at high speed is discussed. Lastly, the performance of this concept system is reviewed along with fabricating the EQS sensors as integrated circuits in the future.

Finally in Chapter 7: Conclusions & Suggestions for Future Work, the design, fabrication, and testing of the EQS sensors and test fixture are reviewed. In addition, suggestions for future work into the investigation of using EQS sensors for surface and sub-surface defect detection during IC fabrication is discussed.

Chapter 2

Design & Fabrication of Macro-Scale EQS Electrode Arrays

This chapter presents the development of electrode arrays to be used with the high frequency drive electronics from Rakesh Kumar's Masters thesis [5] to construct high frequency EQS sensors. Two variable spatial wavelength EQS sensors with millimeter-scale features are produced, which can detect changes in capacitance using high excitation frequencies. These electrode arrays are shown by themselves in Figure 2-1 and attached to the drive electronics to make the EQS sensors in Figure 2-2.

The initial strategy is to construct the electrode arrays from the buried traces in the PCB housing the electrode arrays' high frequency drive electronics. However, this design could not detect changes in capacitance due its small sense area and the high levels of noise in the drive electronics. Moving forward, a simpler, unguarded electrode array with millimeter-scale features is constructed as a bench-level experiment to verify that changes in capacitance can be detected given a larger sense area. Building on the success of this simpler design with an increased sense area, the two variable spatial wavelength, guarded electrode arrays with millimeter-scale features are fabricated. Strategies for constructing these variable spatial wavelength electrode arrays and for attaching them both electrically and mechanically to their high frequency drive electronics are presented. The potential resolution of each of the electrodes ar-

rays is discussed along with the possibility of scaling the variable spatial wavelength electrode arrays down to the MEMS-scale to achieve nanometer resolution.

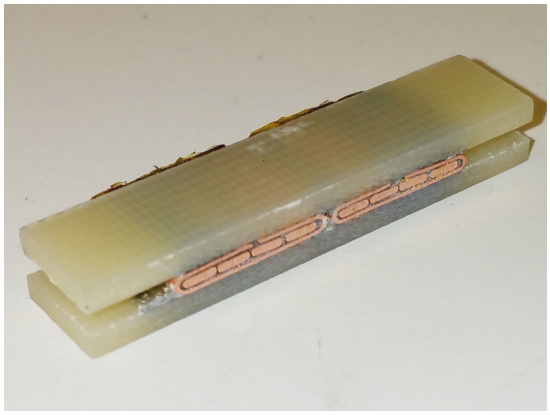

(a) 2x1 long-wavelength electrode array.

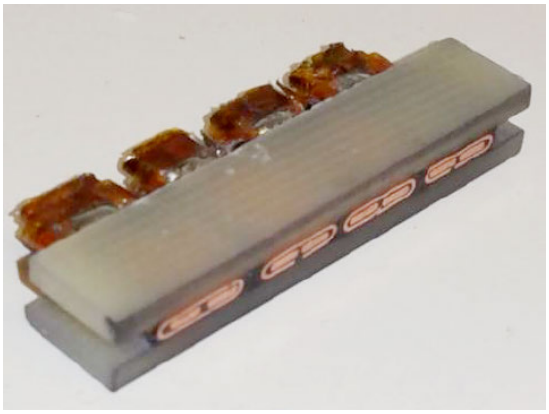

(b) 4x1 short-wavelength electrode array.

(c) 1 long-wavelength electrode pair.

(d) 2 short-wavelength electrode pairs.

Figure 2-1: The two variable spatial wavelength electrode arrays.

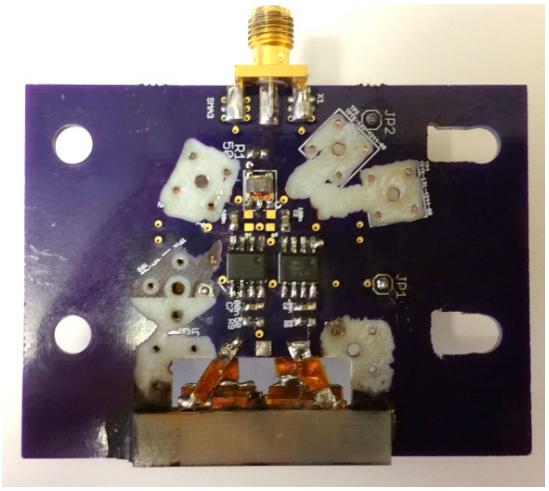

(a) Long-wavelength EQS sensor.

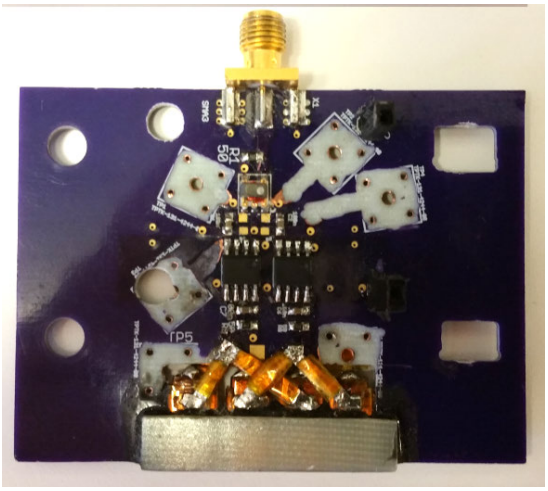

(b) Short-wavelength EQS sensor.

Figure 2-2: Both variable spatial wavelength EQS sensors.

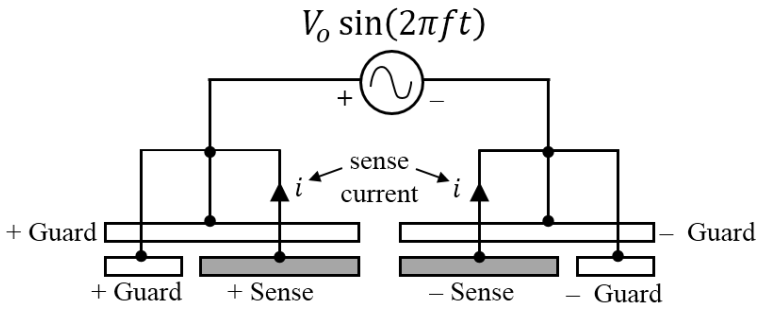

Figure 2-3: Generic layout for an electrode pair in the electrode array [4].

2.1 Electrode Array Concept

The electrode arrays consist of two parts: 1) pairs of oppositely charged sense electrodes and 2) guards electrodes surrounding each sense electrode. Figure 2-3 depicts a generic setup for an electrode pair in the electrode array. The electric field of the sense electrode pair forms a fringing electric field like in Figure 1-2b, capacitively coupling the sense electrode pair to the target as the electrode array sweeps over the target. The target acts like a dielectric in the capacitor formed by the sense electrode pair. Thus changes in the target's material and geometric properties produce changes in the capacitance across the sense electrode pair, allowing for imaging of the target's material and geometric properties.

The guard electrodes are at the same potential as the sense electrodes they surround. This helps minimize the amount the electric field near the surface of the sense electrodes bows outward. As a result, the electric field of the sense electrode pair near the surface of a target against a conductive base can be approximated as relatively straight as shown in Figure 2-4. Thus the capacitor formed by the sense electrode pair and the target can be modeled as a parallel plate capacitor with a single dielectric [5]:

$$C_{\text{Parallel-Single}} = \frac{\epsilon A}{d}, \tag{2.1}$$

where ϵ is the permittivity of the target, A is the cross-sectional area of a single sense electrode, and d is determined by how far the sense electrode pair's electric field can penetrate the target at a given point. For targets thin enough that the electric field

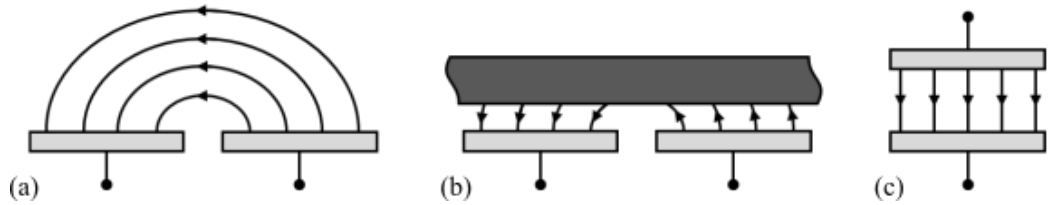

Figure 2-4: As an (a) electrode pair moves next to (b) a target against a conductive base, it begins to resemble two (c) parallel plate capacitors.

can completely penetrate them, d will be the thickness of the target at that point. For thicker targets that the electric field cannot fully penetrate, d will be the electric field's depth of penetration. The depth of penetration is determined by the target's permittivity and conductivity as well as the sense electrode pair's spatial wavelength, the width of the sense electrode pair [16].

However, the sense electrode pair is often separated from the target by another dielectric, an air gap of distance d_{air}. This can be accounted for by modeling the capacitor formed by the sense electrode pair and the target as instead a series combination of parallel plate capacitors, one for the target and one for the air gap:

$$C_{\text{Parallel-Double}} = \frac{\epsilon_{\text{air}} \epsilon A}{\epsilon_{\text{air}} d + \epsilon d_{\text{air}}} \tag{2.2}$$

where ϵ_{air} is the permittivity of air.

In practice, a small difference in potential may exist between the sense electrodes and their surrounding guard electrodes. In such a case, a small capacitance will be sensed between the sense and guard electrodes. Further, the guard electrodes cannot physically begin at the edge of the sense electrodes. There must be some space between the sense and guard electrodes. Thus even with the guard electrodes, the electric fields near the edges of the sense electrode pair still bow outward a non-negligible amount. To account for this, Rakesh Kumar used a fringing field capacitance model [5]. For a sense electrode pair against a single dielectric, the fringing near its edges is given by:

$$C_{\text{Fringe-Single}} = \frac{2\epsilon w}{\pi} \cdot \ln\left(\frac{\pi\Delta + 4d}{4d}\right), \tag{2.3}$$

where w is the perimeter of the sense electrodes and Δ is the gap between the sense

electrodes and the guard electrodes that surround them. See [5], Chapter 2 for more details.

Again, the sense electrode pair usually does not touch the target, but is separated from it by an air gap. As a result, the fringing near its edges is also more accurately given by a series combination of a fringing field capacitor for the air gap and parallel plate capacitor for the target [5]:

$$C_{\text{Fringe-Double}} = \frac{2\epsilon_{\text{air}}\epsilon wA}{2\epsilon_{\text{air}}wd + \pi\epsilon A/\ln(1+\pi\Delta/4d_{\text{air}})}. \tag{2.4}$$

The capacitance between the sense electrode pair and the target is a parallel combination of the parallel plate model's capacitance and the fringing field model's capacitance. For a single dielectric target such as an air gap, this is given by the summation of (2.1) and (2.3):

$$C_{\text{Total-Single}} = \frac{\epsilon A}{d} + \frac{2\epsilon w}{\pi} \cdot \ln\left(\frac{\pi\Delta + 4d}{4d}\right); \tag{2.5}$$

for a double dielectric target such as a constant dielectric material separated from the electrode pair by an air gap, this is given by the summation of (2.2) and (2.4):

$$C_{\text{Total-Double}} = \frac{\epsilon_{\text{air}}\epsilon A}{\epsilon_{\text{air}}d + \epsilon d_{\text{air}}} + \frac{2\epsilon_{\text{air}}\epsilon wA}{2\epsilon_{\text{air}}wd + \pi\epsilon A/\ln(1+\pi\Delta/4d_{\text{air}})}. \tag{2.6}$$

The resolution of the electrode array can be determined by modifying (1.3) for quasistatic imaging:

$$l_{\text{Feature}} - l_{\text{Probe}} \gg v_{\text{Scan}} \cdot T_{\text{Measure}} \tag{2.7}$$

where l_{Feature} is the minimum feature size the electrode array can detect and l_{Probe} is characteristic length of the electrode array in the direction being scanned. Depending on the direction of the scan, this will be either the width or thickness of an electrode pair. Figure 2-5 shows the characteristic length of a 4x1 electrode array. As v_{Scan} is reduced, l_{Feature} approaches l_{Probe}. Thus the resolution of the electrode array is roughly the dimensions of an electrode pair [12].

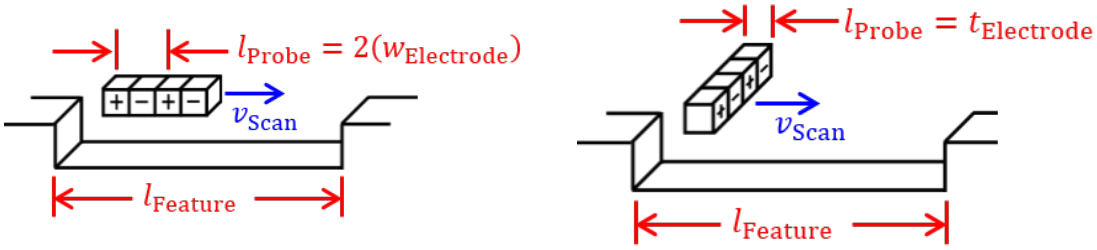

(a) l_{Probe} = width of electrode pair. (b) l_{Probe} = thickness of electrode.

Figure 2-5: Characteristic length for a 4x1 electrode array.

2.2 Electrode Array Design Requirements

In accordance with deterministic design, a list of design requirements for the electrode arrays is first compiled:

Capacitance Measured

Capacitance measured by the electrode array should be maximized to reduce the effects of noise. According to (2.1) and (2.2), capacitance for a sense electrode pair can be maximized by increasing the area of each sense electrode. In addition, the capacitance of the entire array can be increased by increasing the density of the sense electrode pairs. This translates to minimizing the area of the guard electrodes and minimizing the gaps between fellow guard electrodes, the gaps between fellow sense electrodes and gaps between guard and sense electrodes.

Resolution

The electrode array should be designed to minimize the size of smallest detectable feature (maximize resolution). According to (2.7), this means to minimize the dimensions of the sense electrode pairs parallel to the direction of scanning.

Model Integrity

Bowing of the sense electrode pairs' electric field near the electrodes' surface should be minimized such that majority of the capacitance measured can be

modeled using the parallel plate capacitor models. From (2.3) and (2.4), this can be done by minimizing the perimeter of the sense electrodes and the gap between the sense electrodes and their guard electrodes.

Manufacture & Assembly

The electrode array should be designed in such a way that it is easy and cheap to fabricate and easy to attach to its high frequency drive electronics, both electrically and mechanically.

As in most cases in engineering, the design requirements posted above have no optimal solution as some of them contradict each other. Thus trade-offs are made in designing and fabricating the electrode arrays as described below.

2.3 Buried Trace Electrode Array

The initial strategy is to construct the electrode array as part of the PCB containing the high frequency drive electronics. Constructing the electrode array this way has two major benefits. First, this reduces the complexity of fabricating the electrode array. Instead of fabricating the electrode array in-house, the electrode array can be constructed out-of-house with the precision of modern PCB fabrication techniques. In addition, this eliminates having to attach the electrode to its drive electronics mechanically as they are housed on the same board.

For the electrode array to be part of the drive electronics PCB, we decided to construct the electrode array from the buried traces on the PCB. Figure 2-6a shows an illuminated top view of a four electrode array made from the buried traces in the drive electronics PCB. To expose the electrode array's sensing surface, the side of the PCB containing the electrode array is climb milled. Figure 2-6 summarizes this construction of the electrode array.

The guard electrodes for each sense electrode are made from adjacent traces on the same layer as the sense electrode traces and on the layers above and below. All of these traces are connected by vias to form a single guard electrode around each

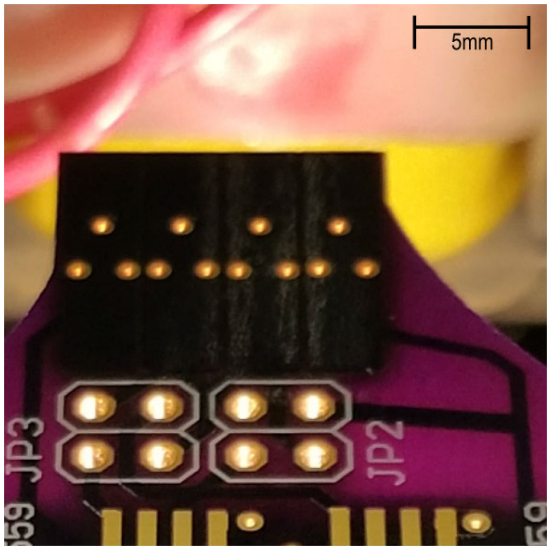

(a) Magnified view of buried traces making up a 4-electrode array.

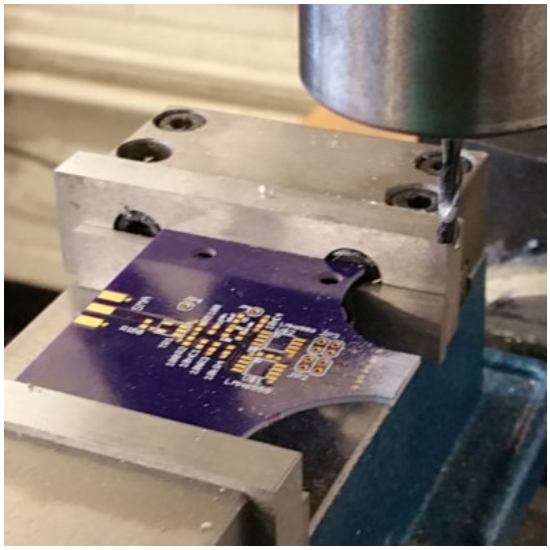

(b) Milling the PCB to expose the buried trace electrode array.

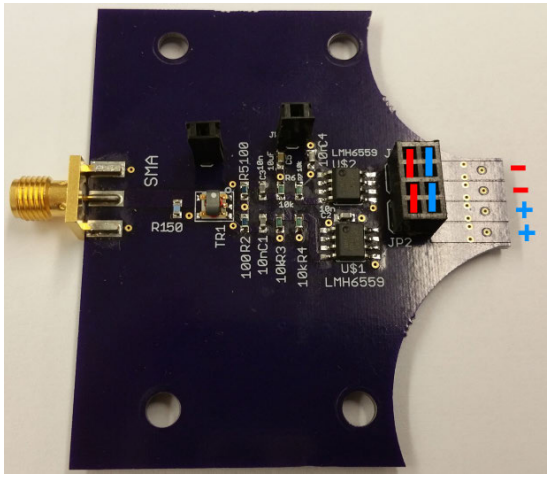

(c) Connecting the electrode array to its drive electronics with vertical jumper wires to set the electrode array pattern to negative, negative, positive, positive.

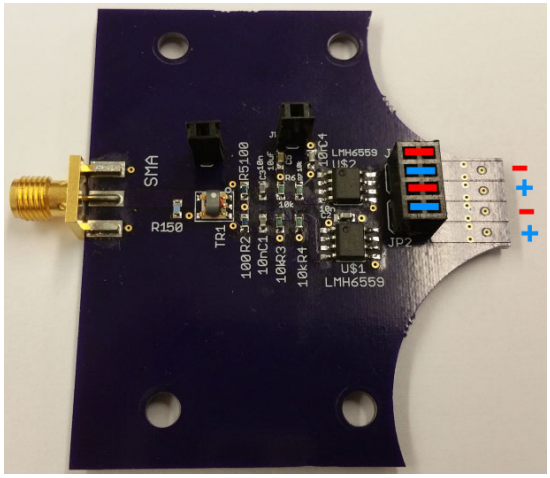

(d) Connecting the electrode array to its drive electronics with horizontal jumper wires to set the electrode array pattern to negative, positive, negative, positive.

Figure 2-6: Construction of an electrode array made from buried traces. In (c) and (d), a red line represents a jumper wire for a negative electrode and a blue line represents a jumper for a positive electrode.

sense electrode. The sense electrodes are also made from multiple traces connected by vias. There are two reasons for this. 1) This increases the area of the sense electrodes. Alternatively, metal layer thickness can be increased, but we chose a standard PCB trace thickness as using a thicker, nonstandard layer thickness would be cost prohibitive. In the same vein, the width of the sense electrode traces can be increased, but this increases the sense electrodes perimeter and thus the amount of undesired fringing which can occur. 2) These choices allow the electrode array be made symmetrically on a 4 layer PCB since the gap between the inner layers of the PCB is different than the gap between the outer and inner layers. We considered both three layer PCBs and PCBs with the same gap between each layer, but these are also nonstandard and are thus cost prohibitive.

We chose the OSH Park company to manufacture the PCB containing the electrode array and high frequency drive electronics due to their low cost. By fabricating PCBs for multiple orders on a single panel, OSH Park can offer 4 layer PCBs for \$5 per square inch. However since multiple orders are fabricated together, layer and trace thickness cannot be customized. Table 2.1 provides the layer thickness for PCBs manufactured by OSH Park, and thus the thickness of the sense and guard electrode traces and their vertical spacing. The two sense electrode traces are each 35.6 μm thick and separated by a 1190.0 μm gap, for a total stack up of 1.27 mm. By (2.7), this translates to a potential later resolution of 1.27 mm when scanning parallel to the thickness of the electrode traces. Reducing this gap would really improve the resolution, but this stack up is acceptable for a low cost first prototype.

Figure 2-7 shows the exposed face of this electrode array with the sense and guard electrode traces dimensioned and labeled. Since the sense electrode traces are so thin, we chose them to be very wide to increase their area and thus the capacitance they can measure. In particular, they are 2.34 mm wide, providing an aspect ratio of approximately 64:1. This large width also means a large perimeter and amount of fringing, but we determined this to be acceptable as it is more important for the initial prototype be able to measure a change in capacitance and not follow the parallel plate model than not be able to measure a change in capacitance. The guard electrode

Table 2.1: PCB Layer Stack Up for the Buried Trace Electrode Array

Layer	Thickness [μm]
solder resist	25.4
copper	35.6
prepreg	170.0
copper	35.6
core	1194.0
copper	35.6
prepreg	170.0
copper	35.6
solder resist	25.4

traces on the same layer as the sense electrode traces and the spacing between the sense and guard electrode traces are 0.15 mm wide as these are the minimum trace width and minimum trace spacing respectively. The outer layer guard electrode traces are 2.95 mm so they begin and end at the same location as the outer edges of the inner layer guard electrode traces.

In addition, we chose the electrode array to have four sense electrodes. There are also two reasons for this. First, by doubling the number of sense electrodes, the capacitance measured doubles. Second, by swapping the drive polarity on the inner two electrodes, the spatial wavelength and thus the depth sensed can be changed. To clarify, an electrode array with a negative, negative, positive, positive sense electrode pattern has a spatial wavelength double of an electrode array with a negative, positive, negative, positive sense electrode pattern. We implemented this by having the sense and guard electrode traces connected by jumper wires to their drive electronics instead of having them directly connected. The orientation of the jumper wires for each electrode array pattern is shown in 2-6c,d. In either orientation, scanning parallel to the width of the sense electrode pair results in a potential lateral resolution equal to the width of the electrode array, 12.25 mm.

To validate the EQS sensor made from this buried trace electrode array and its high frequency drive electronics, this buried trace EQS sensor is attached to an Agilent 4395A impedance analyzer. It is then mounted to an initial test fixture and positioned

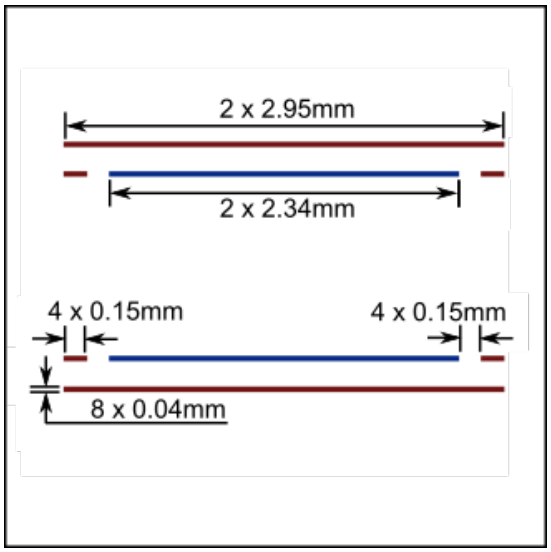

(a) Dimensions of buried traces making up a single sense electrode (blue) and single guard electrode (red).

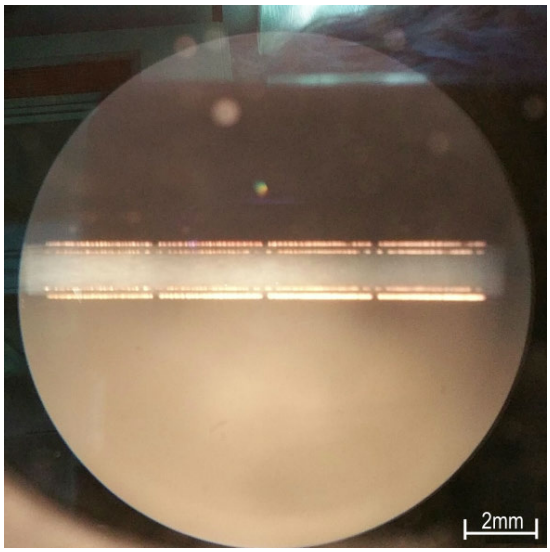

(b) Cross section of buried traces making a 4-electrode array.

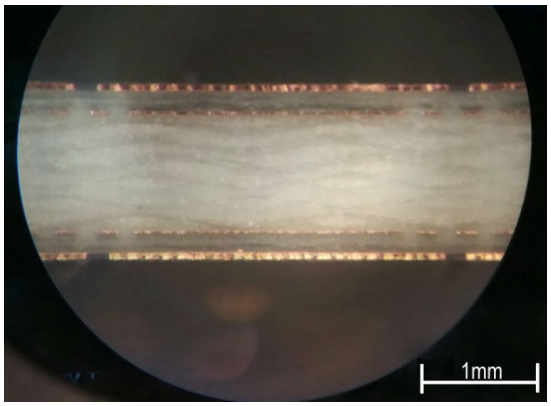

(c) Magnified cross section of traces making 1 sense and guard electrode.

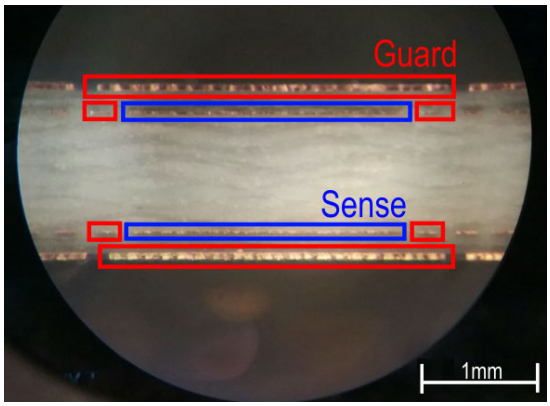

(d) Labeled magnified cross section identifying sense and guard electrodes.

Figure 2-7: Electrode array made from buried PCB traces.

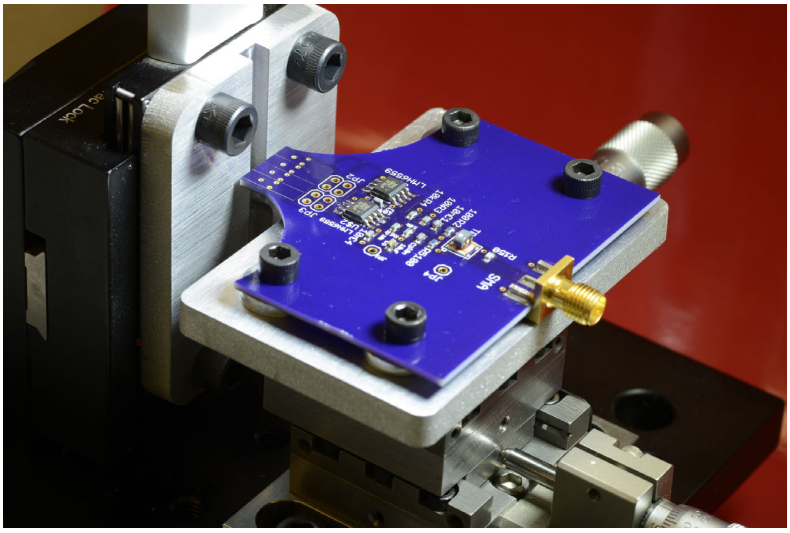

Figure 2-8: Stepping the buried trace EQS sensor away from an aluminum base to verify a change in capacitance due to a change in the thickness of an air gap target can be detected. Note: The jumper wires connecting the electrode array to the high frequency drive electronics are missing in this figure.

next to an aluminum base as shown in Figure 2-8. The design of this initial test fixture is discussed later in Section 3.2. Then the EQS sensor is stepped away from the aluminum base to produce a variable air gap target between itself and the base. By (2.5), variations in the thickness of the air gap target should cause a change in capacitance measured by the EQS sensor which in turn would change the impedance measured by the impedance analyzer.

However, variations in the thickness of the air gap target produce no observable changes in impedance on the impedance analyzer. This is likely due to a combination of there being too much noise in the high frequency drive electronics and the electrode array not measuring a large enough change in capacitance. Moving forward, reducing the noise in the EQS sensor and increasing the changes in capacitance measured are examined.

2.4 Simple Electrode Array

According to (2.1) and (2.2), a larger sense area results in a larger change in capacitance measured due to a change in the material or geometric property of a

target. Thus, we decided to perform a bench-level experiment to determine if a change in capacitance could be measured by an electrode array with a larger sense area. To do this, we decided to use a single, unguarded electrode pair with millimeter-scale features. By using both a single electrode pair and an unguarded design, the high frequency drive electronics are simplified. Having only a single electrode pair reduces the number of traces near the electrodes, reducing their parasitic effects, a possible source of noise in the drive electronics. Using an unguarded design reduces a large portion of the drive electronics circuit, as unity gain buffers are no longer needed to drive the guard electrodes at the same potential of the sense electrodes. Lastly, using a larger, unguarded single electrode pair reduces the complexity of fabrication. This is appealing as this bench-level experiment probe is made in-house.

Figure 2-9 visually summarizes all steps taken to construct the simple electrode array while Figure 2-10 shows the completed simple electrode array. AWG 9 copper wire is used to make the single, unguarded electrode pair. To do this, the copper wire is simply cut into two identical strips. Next a copy of the PCB containing the drive electronics and the buried trace electrode array is milled to remove both the previous electrode array and the drive electronics for the guard electrodes. The remaining sense drive electronics are depicted in Figure 2-11. This is done instead of designing a new PCB, as the OSH Park company only sells PCBs in sets of 3 copies, so there were two left over from the initial order.

The two sense electrode wires and the sense drive electronics PCB are positioned relative to each other using a set of gauge blocks as shown in Figure 2-9c. In particular, the PCB is positioned vertically on top of a 2.5527 mm (0.1005 in) gauge block with the two sense electrode wires next to it, but not on the gauge block. This causes the face of sense electrode pair to be offset from the PCB. This is done to guarantee that the face of the electrode array is the closest part of the sensor to the aluminum base when the sensor is positioned next to the base. In addition, we placed a 3.556 mm (0.140 in) gauge block between the sense electrode wires to keep them a fixed distance apart. The PCB and sense electrodes are position vertically instead of horizontally in order to utilize gravity as a preload.

(a) Cut two strips of AWG 9 copper wire to make the sense electrodes.

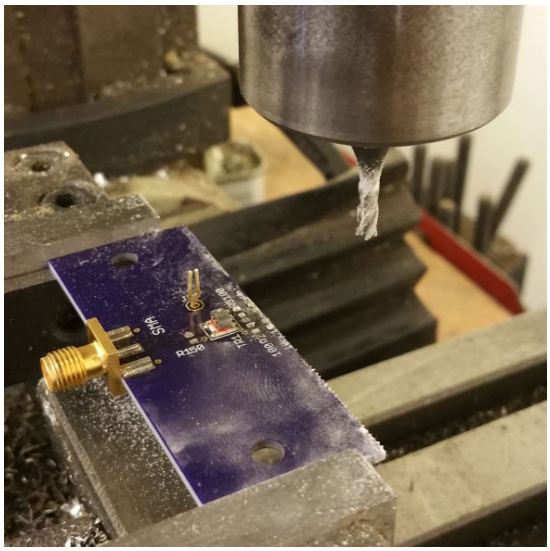

(b) Mill away the guard electrode high frequency drive electronics.

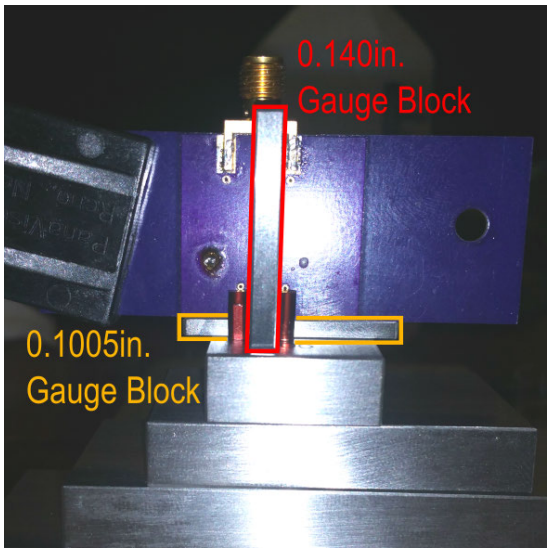

(c) Use gauge blocks to set distance between sense electrodes and to set their overhang.

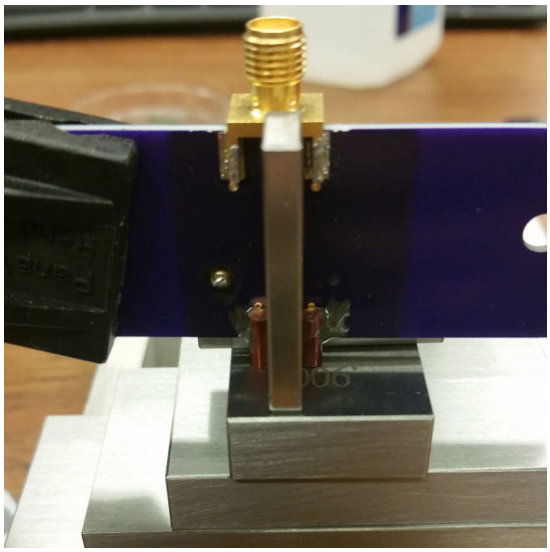

(d) Epoxy sense electrodes in place and solder them to their drive electronics. 832HT-375 high temperature epoxy should be used.

Figure 2-9: Construction of a simple electrode array from AWG 9 copper wire.

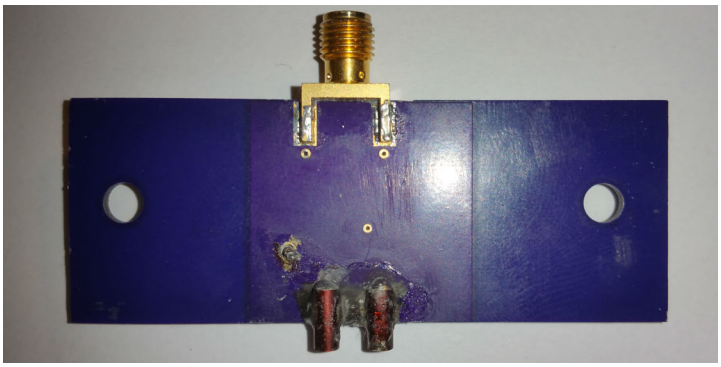

(a) Bottom view of the simple electrode array as part of the simple EQS sensor.

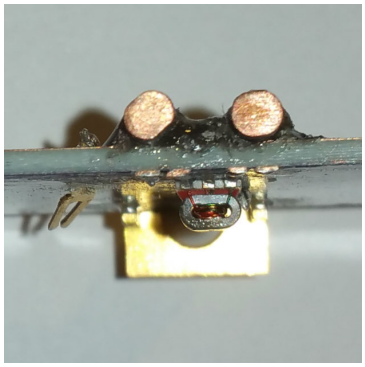

(b) Cross section of simple electrode array.

Figure 2-10: A simple electrode array made from AWG 9 copper wire.

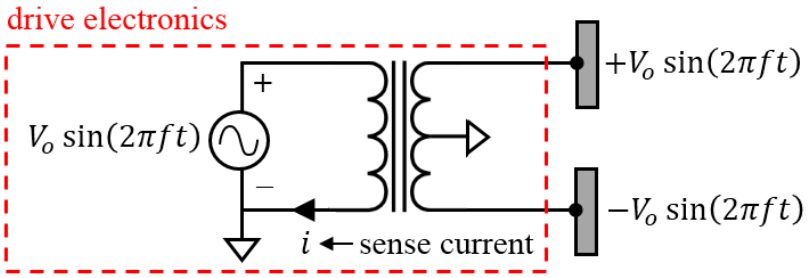

Figure 2-11: The two sense electrodes of the simple electrode array are driven by a center tapped transformer.

The sense electrode wires are then epoxied in place. The sense electrode wires are sized such that when epoxied into place, their ends fall on pads for their drive electronics. Afterwards, the sense electrode wires are directly soldered to their drive electronics. Unfortunately, the heat from soldering causes the epoxy to burn, but not enough to warrant remaking this simple electrode EQS sensor. Learning from this, 832HT-375 high temperature epoxy from MG Chemicals is used for making future electrode arrays as this epoxy is rated up to the temperatures used in soldering.

The simple EQS sensor's ability to detect changes in capacitance is verified using the same process used to test the buried trace EQS sensor. The simple EQS sensor is attached to the Agilent 4395A impedance analyzer, mounted on the initial test fixture, and positioned next to the aluminum base. Figure 2-12 shows this sensor positioned next to the base. The sensor is then stepped away from the aluminum base to produce a variable air gap target which by (2.1) should cause a change in

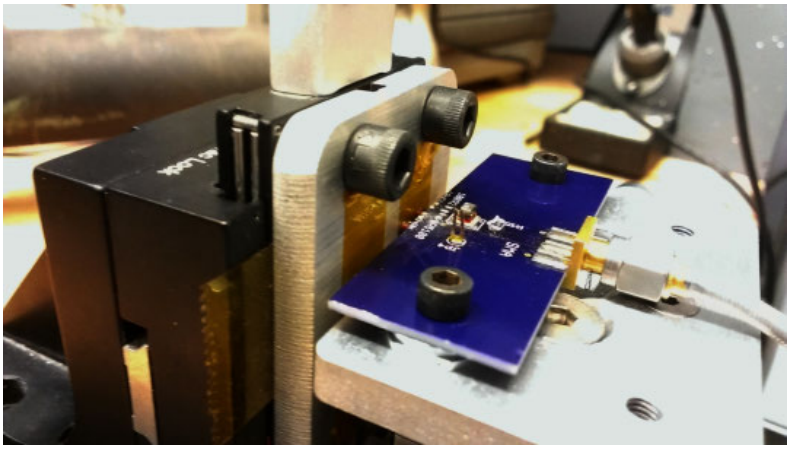

Figure 2-12: Stepping the simple EQS sensor away from an aluminum base to see if a change in capacitance due to a change in thickness of an air gap target can be detected.

capacitance and in turn a change in impedance on the impedance analyzer.

Stepping the simple EQS sensor did produce a change in capacitance. This confirms that a larger sense area is indeed required. In accordance with (2.7), this EQS sensor would have a potential lateral resolution of 2.9 mm while scanning parallel to the thickness of its electrode array and 9.4 mm when scanning parallel to the width of its electrode array. In addition, Rakesh Kumar found that the use of jumper wires is a major source of noise in the high frequency drive electronics [5] so having the sense electrode wires directly soldered to the sense drive electronics also helped. With this information, we decided to make a guarded electrode array with millimeter-scale features that was directly soldered to the drive electronics.

2.5 Variable Spatial Wavelength Electrode Arrays

Building upon the observation that a change in capacitance could be measured with a larger sense area, the next step is to build a guarded electrode array with millimeter-scale features. Multiple concepts are generated for creating the sense electrodes and their surrounding guard electrodes. Further, several concepts are created for constructing an electrode array from these sense and guard electrodes, and attaching this electrode array both mechanically and electrically to the PCB containing the

high frequency drive electronics. Two variable spatial wavelength electrode arrays are fabricated and attached to the drive electronics: a 2x1 long-wavelength electrode array and a 4x1 short-wavelength electrode array. These electrode arrays and the resulting EQS sensors are depicted earlier in Figures 2-1 and 2-2, respectively.

The long-wavelength electrode array only has 2 alternatingly charged electrodes while the short-wavelength electrode array has 4. Further, the long-wavelength electrode array has a longer spatial wavelength as the centers of two oppositely charged electrodes are farther apart. The long-wavelength electrode array is created and tested first. After being able to successfully measure a change in capacitance, the short-wavelength electrode array is constructed using the same concepts. The short-wavelength electrode array is also able to measure a change in capacitance.

2.5.1 Initial Designs

Concepts for Electrode Array Construction

To fabricate a guarded electrode array with millimeter-scale features, two strategies are conceived. Strategy 1 is to construct the entire electrode array layer-by-layer whereas Strategy 2 is to fabricate the individual electrodes in the array separately and then construct the electrode array from these individual electrodes. Figure 2-13 depicts a concept for building the electrode array by Strategy 1 and Figure 2-14 depicts two concepts for building the electrode array by Strategy 2.

Constructing the electrode array layer-by-layer, Concept 1, is similar to how the buried trace electrode array is constructed. However, since this would be manufactured in-house, dimensions such as layer thickness could now be directly controlled. To construct the electrode array layer-by-layer, different thickness copper sheets and single thickness FR4 sheets would be obtained. The thicker copper sheets would be used to fabricate the sense electrodes and the portion of the guard electrodes on their sides. The thinner copper sheets would be used to fabricate the guard electrodes portions above and below the sense electrodes while the sheets of FR4 would be used to set the gap between the sense and guard electrodes.

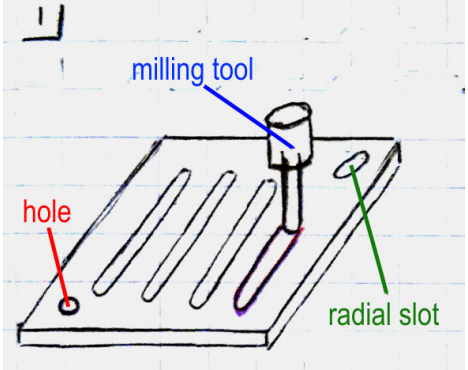

(a) Mill slots into copper sheets to make both sense and guard electrodes.

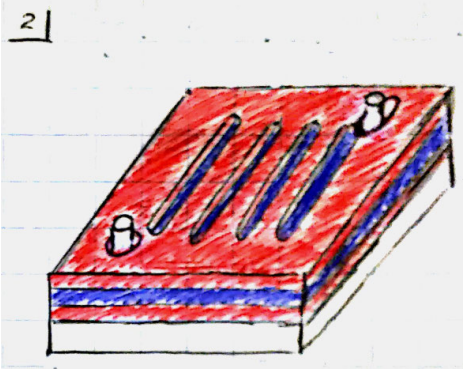

(b) Stack and epoxy together sheets of milled copper (red) and FR4 (blue) using dowel pins for alignment.

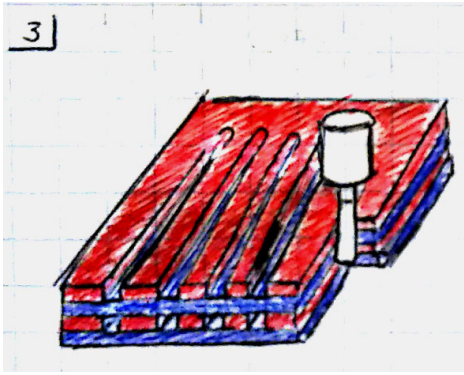

(c) Mill stack to separate the sheets of copper into individual electrodes.

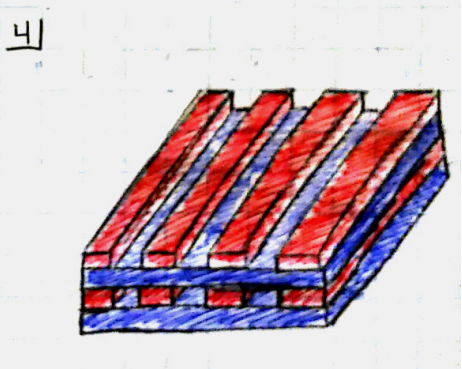

(d) Concept electrode array made from sheets of FR4 and milled copper.

Figure 2-13: Concept 1: Build the electrode array layer-by-layer.

Each layer would have a hole and radial slot milled into it. This would allow each layer to be kinematically positioned on a fixture with two dowel pins during milling and final layer-by-layer assembly of the electrode array. Each layer would be kinematically positioned as number of planar constraints applied is the same as the number of planar degrees of freedom. Each layer has 3 planar degrees of freedom: X-translation, Y-translation, and rotation. The pin in the hole provides a constraint in X-translation and Y-translation while the pin in the radial slot provides a constraint in rotation.

Slots would be milled in the corresponding thickness copper sheets to make the

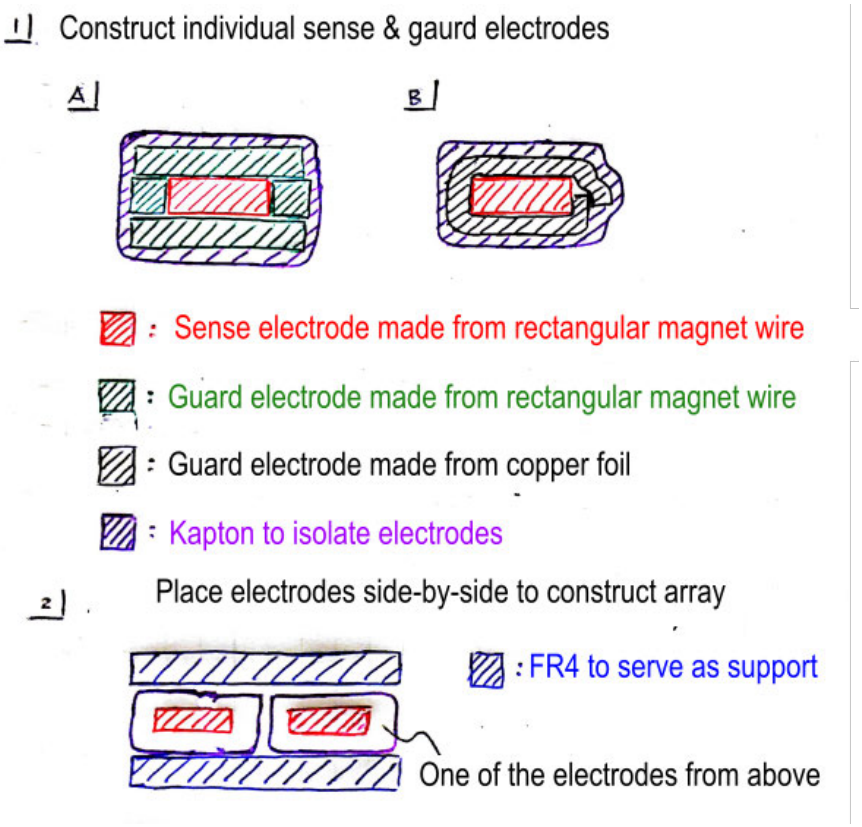

Figure 2-14: Concept 2: Build the electrode array from individual electrodes.

sense electrodes and guard electrode components. The sheets of FR4 and milled copper would be stacked up on the two dowel pin fixture with adhesive between each layer. This adhesive would be 832HT-375 high temperature epoxy. Glass beads could be added to the adhesive to also set the adhesive thickness. The edges of the stack would then be milled to separate the copper layers into individual sense electrodes and guard electrode components. Finally, each guard electrode's components would be electrically connected, finishing the electrode array, when the electrode array was attached to its drive electronics.

For the second concept of constructing the electrode array from individually fabricated electrodes, two similar concepts were devised. In both cases, the sense electrode would be made from large rectangular magnet wire or multiple strips of smaller rectangular magnet wire placed side-by-side. Using large rectangular magnet wire versus multiple strips of rectangular magnet wire would be determined later upon researching if rectangular magnet wire came in the aspect ratio desired.

The fabrication of Concept 2 could take two approaches. In the first, (A), the guard electrodes would also be made from rectangular magnet wire. The guard electrodes would be constructed from components similar to the way they would be built in Concept 1. Strips of rectangular magnet wire would be placed around the sense electrode and then connected electrically when attaching the electrode array to its drive electronics, completing the guard electrodes. In the second, (B), the guard electrodes would be made by wrapping insulation and copper foil around the sense electrodes.

To construct the array, these individual electrodes would be placed side-by-side and sandwiched between two layers of FR4 with 832HT-375 high temperature epoxy. After the electrode array is constructed, the sensing face of the electrode array would then have to be milled to guarantee that the sense faces of the electrode pairs in the electrode array are coplanar.

We chose Concept 2B, building the electrode array from individual electrodes using copper foil as guards, as the method to fabricate the electrode array. Figure 2-15 shows an electrode array quickly prototyped using this method. Relative to Concept 1, building the electrode array layer-by-layer, Concept 2B is much quicker to construct. The rectangular magnet wire and copper foil can be cut by hand instead of having to mill several layers of copper and FR4. Further, no fixture has to be constructed. However, Concept 1 is ultimately much more repeatable and can be used in the future to more easily make large electrode arrays with many electrode pairs. We chose Concept 2B over Concept 2A, building the electrode array from individual electrodes using rectangular magnet wire as guards, as this requires less parts.

Concepts for Attaching the Electrode Array to the Drive Electronics PCB

We conceived four concepts to attach the electrode array to the high frequency drive electronics PCB, both mechanically and electrically. Figure 2-16 displays these four concepts for mechanical attachment while Figure 2-17 displays these four concepts for electrical attachment.

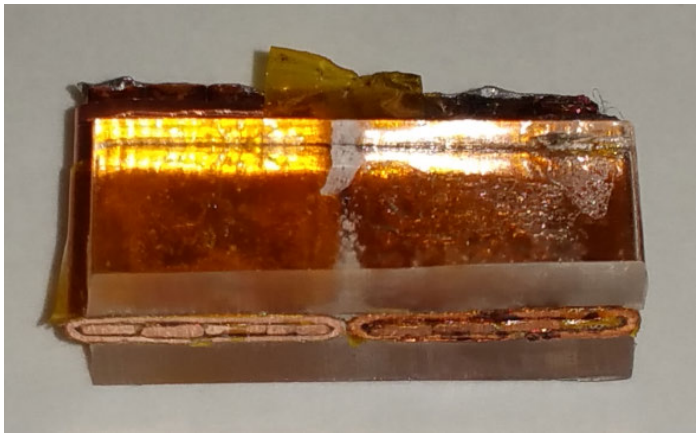

Figure 2-15: Prototype for a variable spatial wavelength electrode array.

The four concepts for mechanical attachment are governed by two strategies: attachment with adhesive and attachment with fasteners. The two concepts for mechanically attaching with adhesive are to epoxy the electrode array directly to the drive electronics PCB or to epoxy both the electrode array and the drive electronics PCB to an intermediate surface. To fasten the electrode array to the drive electronics PCB, the electrode array can be screwed to the drive electronics PCB using the existing holes for mounting the PCB to the test fixture or with newly machined holes.

Attaching the electrode array with the drive electronics PCB's mounting holes is problematic as the sensor would have come apart if it needed to be removed from or repositioned on the test fixture. In addition, using epoxy is attractive as it requires less space than fasteners. We chose epoxying the electrode array directly to the drive electronics PCB, as the drive electronics PCB had components soldered to its bottom and would not sit flat on an intermediate surface without machining spaces for those components. Also, the drive electronics PCB still has the buried trace electrode array on the board. This would need to be milled away to minimize parasitics and would leave a space for the new electrode array.

To epoxy the electrode array to the drive electronics PCB, the support layers of FR4 above and below the electrodes would be wider than the electrodes. As a result, the electrode array would have two overhanging layers of FR4 on its sides with nothing in between them. The drive electronics PCB would be slid into this

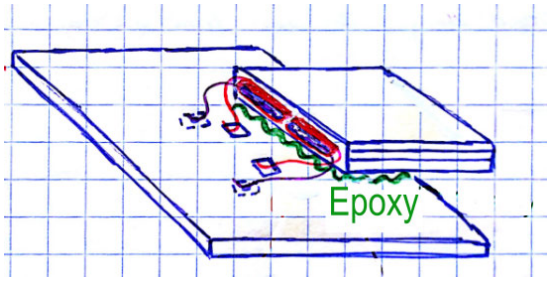

(a) Epoxy the electrode array directly to the drive electronics PCB.

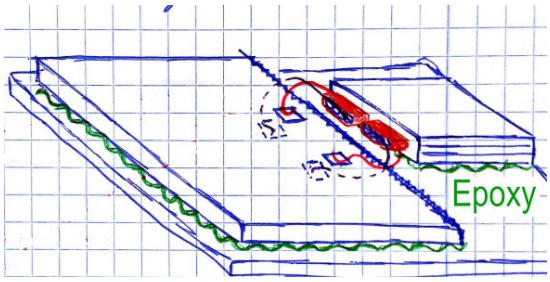

(b) Epoxy the electrode array and the drive electronics PCB to an intermediate board.

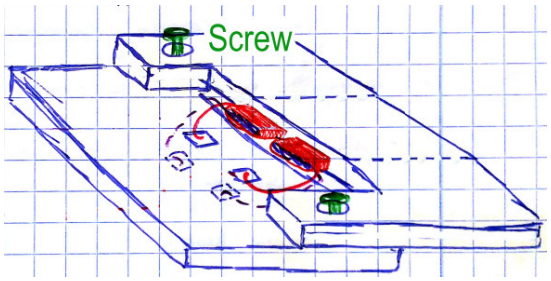

(c) Attach the electrode array to the drive electronics PCB with its test fixture mounting holes.

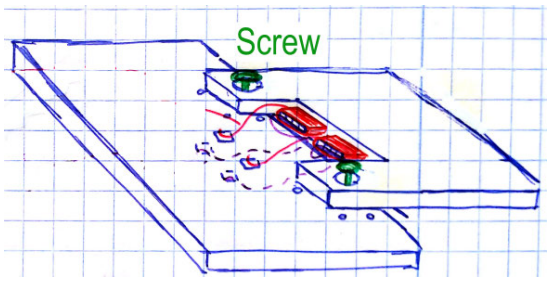

(d) Attach the electrode array to the drive electronics PCB with new holes.

Figure 2-16: Four concepts for mechanically attaching the electrode array to the drive electronics PCB.

empty slot which would be sequentially filled with epoxy. This would form a very rigid connection as both sides of the drive electronics PCB would be epoxied to the electrode array. Figure 2-18 portrays this.

As for electrically attaching the electrode array to its drive electronics, one method is to stagger ends of the guard and sense electrodes. This way, the tops of the sense and guard electrodes would be exposed and provide an easily accessible spot to solder wires running from the drive electronics. Another method is to solder wires to the tops of the sense and guard electrodes before epoxying them together such the wires could come from in between the guard and sense electrodes. Alternatively, if the electrode array is fabricated using Concept 1, the wires could be attached in the gaps formed by the slots milled into the copper. Lastly, the wires could be attached directly to the back of the electrodes in the electrode array.

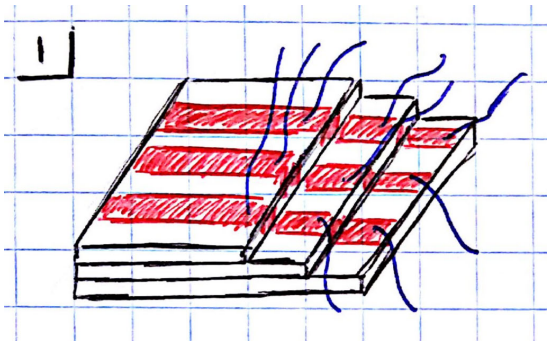

(a) Stagger sense and guard electrode ends and attach wires to the electrode tops.

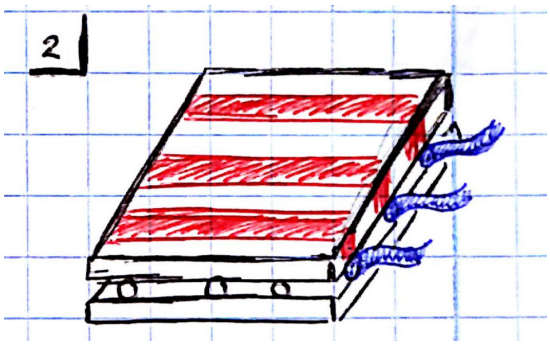

(b) Attach wires before epoxying electrodes together so the wires come from between electrodes.

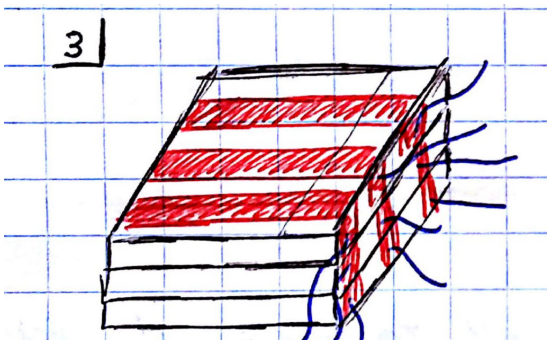

(c) Attach wires to the back sides of the sense and guard electrodes.

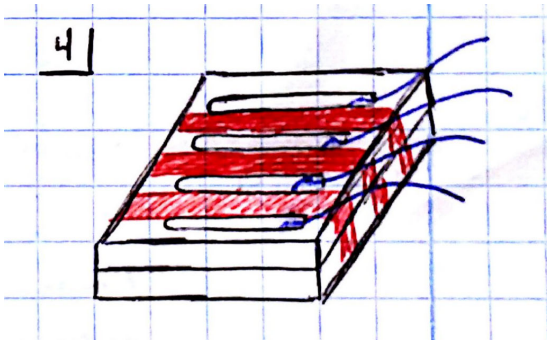

(d) Attach wires in gaps between the sense and guard electrodes.

Figure 2-17: Four concepts for electrically connecting the electrode array to the drive electronics.

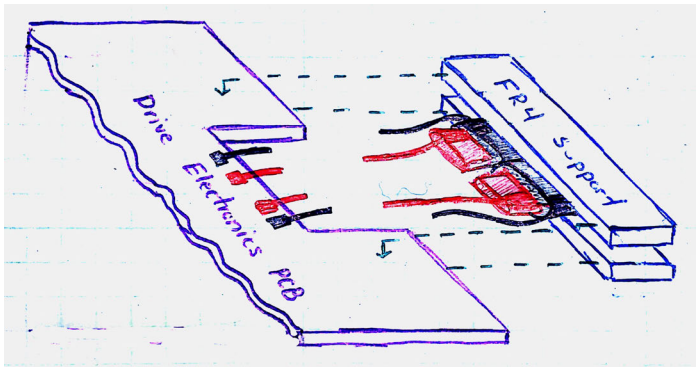

Figure 2-18: Final concept for attaching variable spatial wavelength electrode arrays to the drive electronics PCBs.

Since the electrode array is not going to be built layer-by-layer, there are no gaps from milling slots in copper sheets to place wires in. In addition, it is simpler to build the electrode array and then attach wires to it so attaching the wires before epoxying the electrodes together is undesirable. As for attaching to the tops of staggered sense and guard electrodes, the enamel coating on the sense electrodes' rectangular magnet wire would need to be removed. However attaching to the backs of all the electrodes would get very crowded. Thus we decided to stagger the sense and guard electrodes, but only attach wires to the tops of the guard electrodes. For the sense electrodes, wires would be attached to their backs. This is portrayed in Figure 2-18.

2.5.2 Final Design

Two variable spatial wavelength electrode arrays are constructed according to the concepts decided above in Section 2.5.1: a 2x1 long spatial wavelength electrode array and a 4x1 short spatial wavelength electrode array. The long-wavelength electrode array has 2 alternatingly charged electrodes while the short-wavelength electrode array has 4. Further, the long-wavelength electrode array has a longer spatial wavelength as the centers of two oppositely charged electrodes are farther apart. Initially, we only fabricated the 2x1 long-wavelength. However, after successfully measuring a change in capacitance with this array, we built the short-wavelength electrode array.

For both of these variable wavelength electrode arrays, the individual sense electrodes with their surrounding guard electrodes are constructed first. The steps to construct the individual electrodes are visually summarized in Figure 2-19. Each sense electrode is constructed from 12 mm long strips of AWG 16.5 1:3.5 rectangular magnet wire placed side-by-side, 4 strips for the long-wavelength sense electrodes and 2 strips for the short-wavelength sense electrodes. Four wire strips are used for each long-wavelength electrode so its sense area is larger than the simple electrode array's. We did this so the detected changes in capacitance are larger in case the readdition of the guard electronics or the wiring used to connect the array to the drive electronics introduces a lot of noise.

The wire strips have an enamel coating to insulate them from the copper foil to be

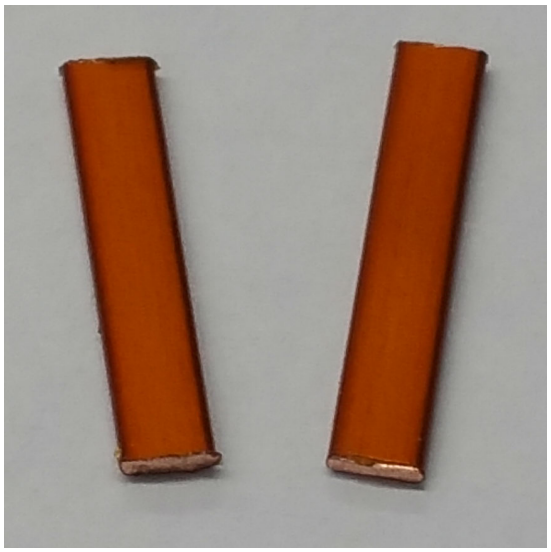

(a) Cut AWG 16.5 1:3.5 rectangular magnet wire.

(b) Insulate with 0.064 mm (2.5 mil) Kapton tape.

(c) Wrap in 0.254 mm (10 mil) copper foil.

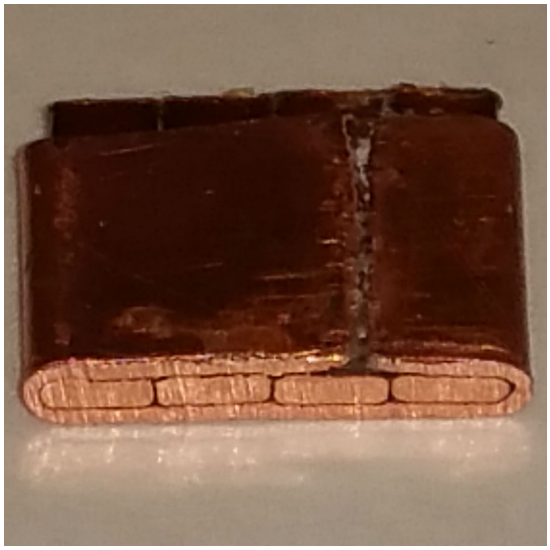

(d) Epoxy together with 832HT-375 high temperature epoxy.

Figure 2-19: Construction of an electrode from rectangular magnet wire.

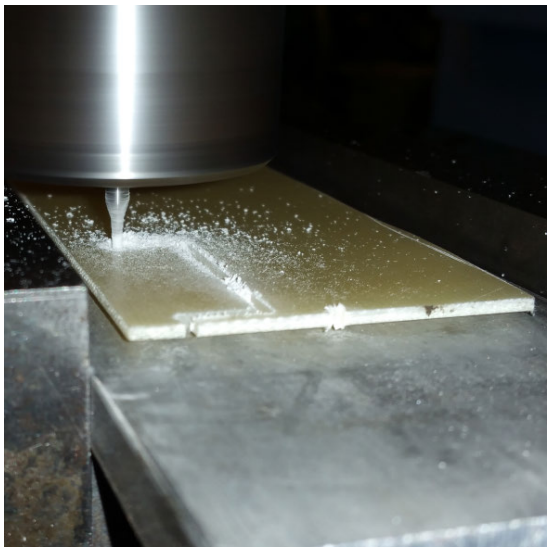

(a) Mill two pieces of FR4 to serve as support and a way to mount to the drive electronics PCB.

(b) Epoxy pairs of electrodes between the two support pieces of FR4 with 832HT-375 high temperature epoxy.

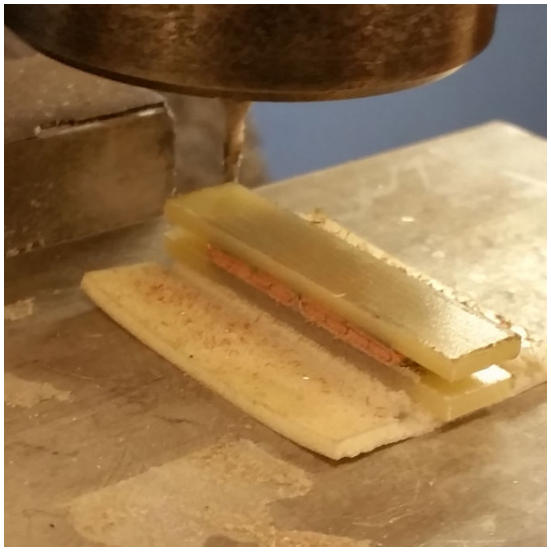

(c) Mill the electrode array face flat.

(d) Lap with increasing grit sandpaper and finally 2000 grit paste.

Figure 2-20: Construction of variable spatial wavelength electrode arrays.

wrapped around them, but this coating can have scratches and defects. Thus these side-by-side wire strips are wrapped in 0.065 mm (2.5 mil) thick Kapton tape to further isolate them and hold them together. Next 0.254 mm (10 mil) thick copper foil is cut to make the guard electrodes. The copper foil is cut to be 10 mm long, 2 mm shorter than the wire strips, so that the ends of the sense and guard electrodes are staggered. This copper foil is wrapped around the side-side-wire wire strips and epoxied to them using 832HT-375 high temperature epoxy to make the guard electrode. Finally, the copper foil is wrapped in Kapton tape to electrically isolate the guards of electrodes that are placed side-by-side. In wrapping the copper foil with Kapton tape, a section is left exposed on the top of the copper foil to provide electrical access to the guards.

To create electrode arrays from these electrodes, two pieces of FR4 are milled for each electrode array. These pieces of FR4 serve as support for the electrodes mounted to them and a way for the electrode array to be epoxied to the drive electronics board. In addition, these pieces are 8 mm long, 2 mm shorter than the copper foil guards, such that the tops of the guards can be accessed to make electrical connections.

Figure 2-20 visually recaps the steps to construct the variable wavelength electrode arrays from their individual electrodes. Two side-by-side long-wavelength electrodes are sandwiched and epoxied between two pieces of FR4 to construct the 2x1 long-wavelength electrode array. 832HT-375 high temperature epoxy is again used. Four side-by-side short-wavelength electrodes is used to create the 4x1 short-wavelength electrode array so that it has roughly the same footprint and sense area as the 2x1 long-wavelength electrode array. After their assembly, these electrode arrays are squared up on a mill and climbed milled to guarantee the sense faces of all electrodes in the electrode array are coplanar. Lastly, the sense faces of these electrode arrays are lapped with increasing grit sand paper and 2000 grit paste on a granite lapping plate. Figure 2-21 shows the effects of lapping on the electrode array's sense face. In addition, Figure 2-22 is provided to show 2000 grit paste provides an almost mirror finish, indicating the electrodes are very coplanar.

The last step to finish fabricating the different wavelength electrode arrays is to

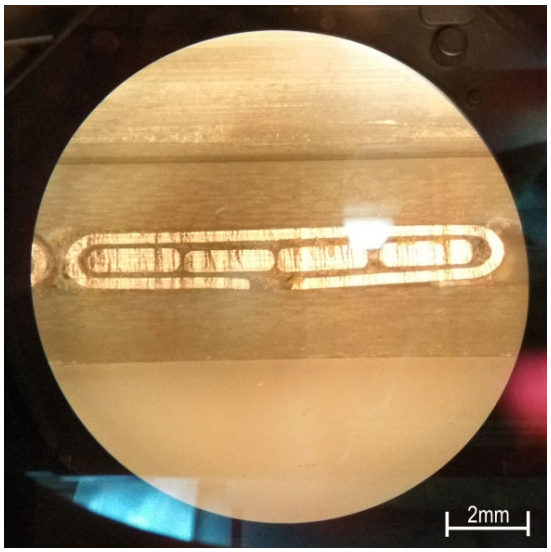

(a) Long-wavelength electrode's face before lapping.

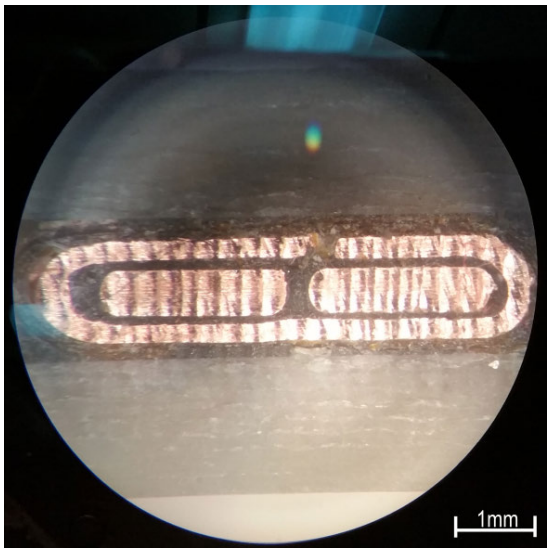

(b) Short-wavelength electrode's face before lapping.

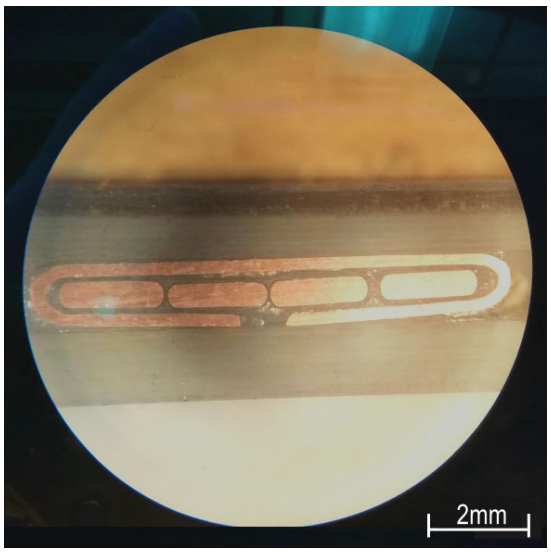

(c) Long-wavelength electrode's face after lapping.

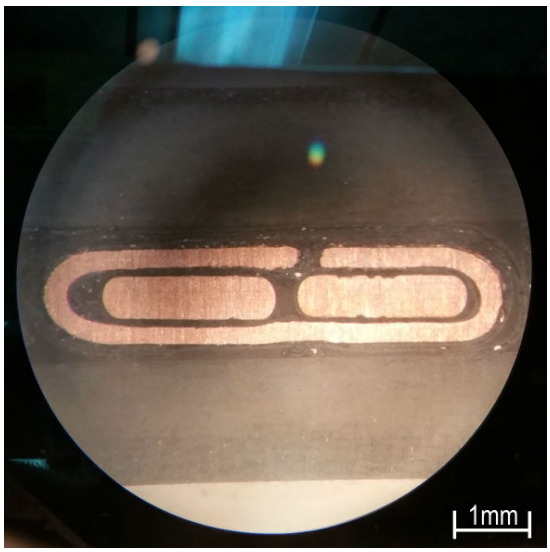

(d) Short-wavelength electrode's face after lapping.

Figure 2-21: Variable spatial wavelength electrode faces before & after lapping.

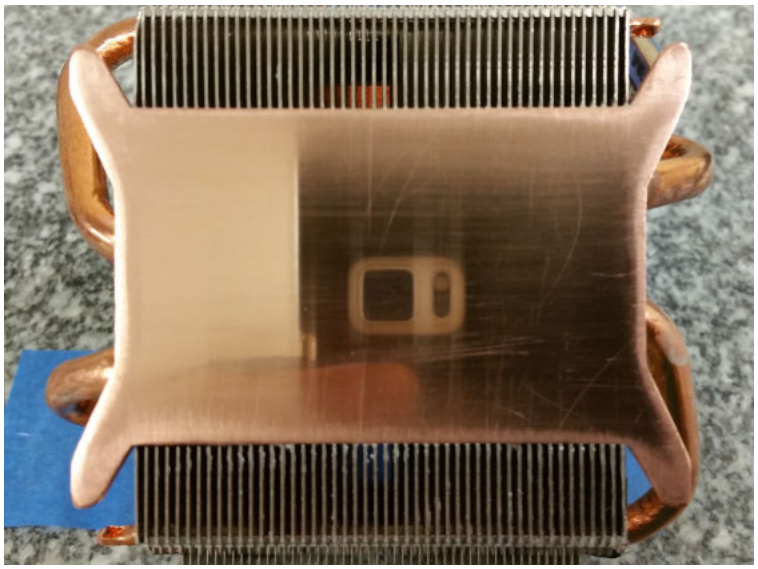

Figure 2-22: A heat sink with an identical finish as the faces of the electrode arrays to show 2000 grit paste provides an almost mirror finish, indicating the electrodes are very coplanar.

electrically connect each set of side-by-side rectangular magnet wire strips into a sense electrode. This is done by applying solder across the back of each set of wire strips as shown in Figure 2-23. A stripped piece of wire can also used, but ultimately this is unnecessary. To confirm these wire strips are electrically connected, the conductivity between each wire strip is tested with a Fluke 1587 insulation multimeter. Further, the insulation multimeter shows each of the sense and guard electrodes are electrically isolated from each other up to a drive voltage of 500 V, much higher than the drive voltage from the drive electronics.

The fully fabricated and electrically tested variable wavelength electrode arrays are shown earlier in Figure 2-1; their dimensions are shown provided in Figure 2-24. To mechanically attach these electrode arrays to the high frequency drive electronics, a slot needs to be milled into the drive electronics PCBs. The drive electronics PCBs are fixtured in the mill using double sided tape and milled as shown in Figures 2-25a-c. The electrodes arrays are slipped into the slot of the drive electronics PCBs such that the drive electronics PCB is sandwiched between the electrode array's overhanging FR4 supports. This assembly is placed vertically with the drive electronics PCB on top of 0.9 mm shims and epoxied together with 832HT-375 high temperature

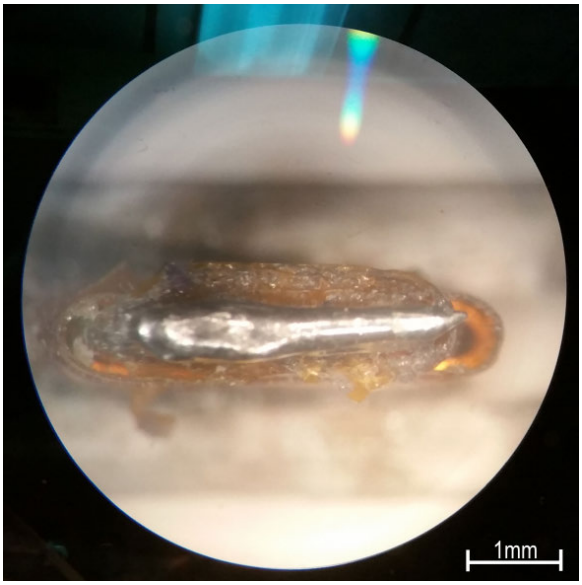

Figure 2-23: Solder the backs to the copper wires together to create a single sense electrode.

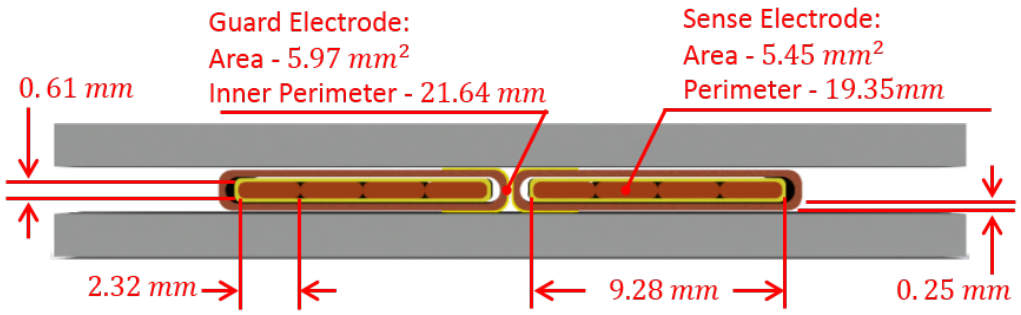

(a) Dimensions of the 2x1 long-wavelength electrode array.

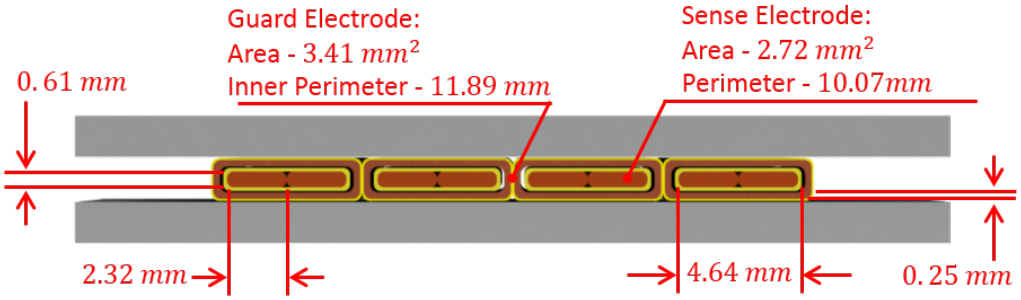

(b) Dimensions of the 4x1 short-wavelength electrode array.

Figure 2-24: Dimensions of the electrode arrays.

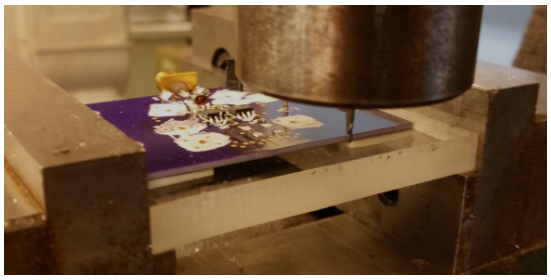

(a) Fixture drive electronic PCB in mill with double-sided tape.

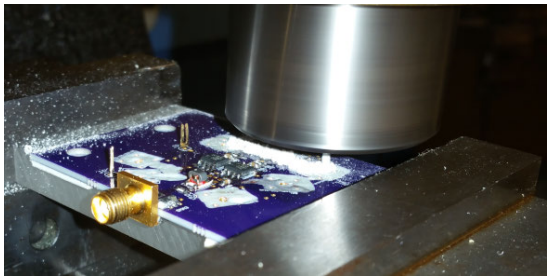

(b) Mill out slot in drive electronic PCB for electrode array.

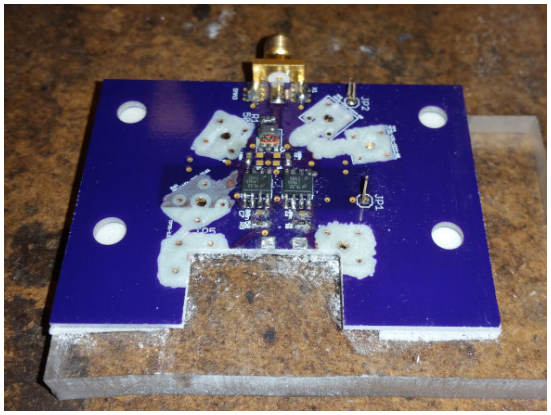

(c) Slot in electronic PCB for electrode array.

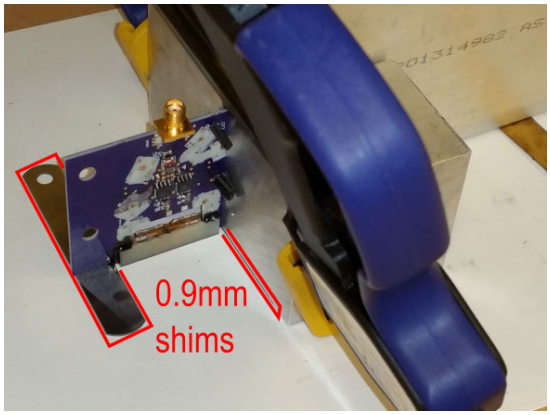

(d) Epoxy electrode array into drive electronic PCB slot.

Figure 2-25: Attachment of electrode array to the drive electronic PCB.

epoxy. The shims offset each electrode array's sense face from the edges of the drive electronics PCB to guarantee the sense face of the electrode array will be the closest part to the target during testing. In addition, this is done vertically to use gravity as a preload.

To electrically attach the electrode arrays to the drive electronics, strips of copper foil wrapped in Kapton tape are used. Each strip is wrapped in Kapton to prevent shorts. Copper foil is used instead copper wire to minimize the inductance of the connection between the electrode array and the drive electronics. For the sense electrodes, the copper foil runs from the back of the sense electrodes to the pads of the drive sense electronics. These connections are shown by Figure 2-26c,d for the long-wavelength and short-wavelength electrode arrays respectively. For the guard electrodes, the copper foil runs from the guard electrode tops to the pads of the

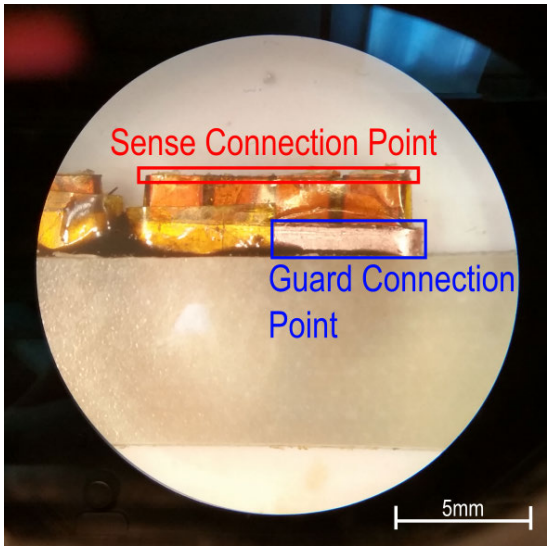

(a) Long-wavelength sense and guard electrode electrical connection points.

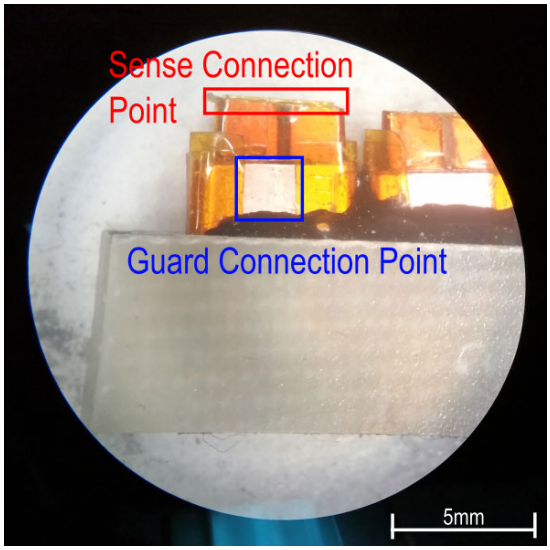

(b) Short-wavelength sense and guard electrode electrical connection points.

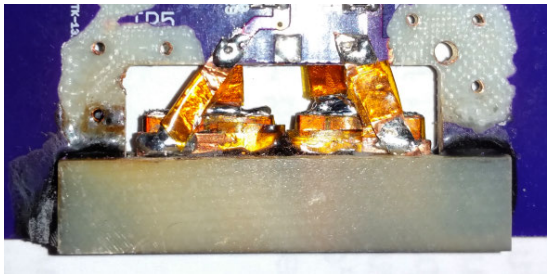

(c) Top view showing long-wavelength guard electrodes electrical connection to the drive electronics.

(d) Top view showing short-wavelength guard electrodes electrical connection to the drive electronics.

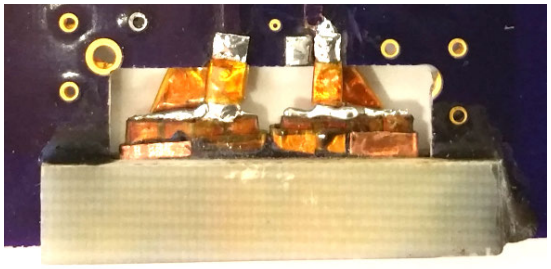

(e) Bottom view showing long-wavelength sense electrodes electrical connection to the drive electronics.

(f) Bottom view showing short-wavelength sense electrodes electrical connection to the drive electronics.

Figure 2-26: Electrode arrays' electrical connections.

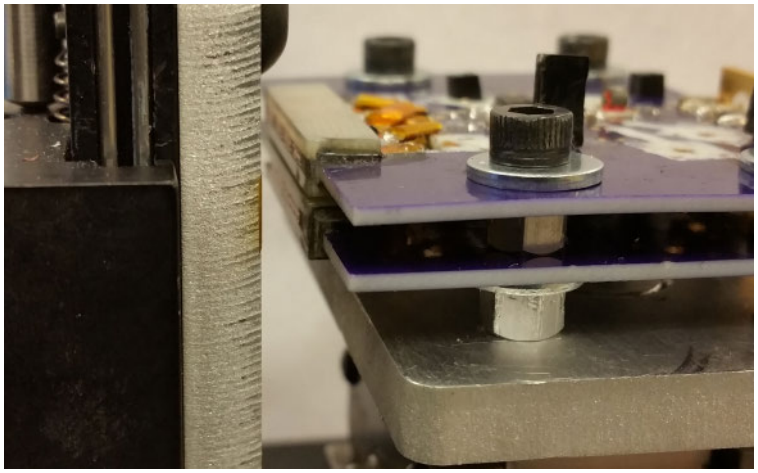

Figure 2-27: Stepping both the variable spatial wavelength EQS sensors away from an aluminum base to see if a change in capacitance due to a change in thickness of an air gap target can be detected. Note, only one sensor can be measured with at a time as the Agilent 4395A impedance analyzer only has one port.

guard drive electronics. These connections are shown in Figures 2-26e,f.

The complete long-and short-wavelength sensors are depicted earlier in Figure 2-2. The long-wavelength sensor is initially tested by itself as the short-wavelength EQS sensor is built after the long-wavelength sensor is confirmed to work. However, they are both tested the same way. They are tested the same way as the buried trace and simple EQS sensors. Both are connected to an Agilent 4395A impedance analyzer, mounted on the initial test fixture, and positioned relative to the aluminum base as shown in Figure 2-27. They are then stepped away from the base to produce a variable air gap target, which by (2.1) should cause a change in capacitance and in turn a change in impedance on the impedance analyzer. Since the impedance analyzer only has one port, capacitance changes can only be measured with one sensor at a time.

Stepping both sensors, changes in the thickness of the air gap did produce a change in capacitance. Sections 3.3.1 and 5.1 show both sensors' capacitance varies inversely with the thickness of the air gap. Using (2.7), these sensor have a potential lateral resolution of 0.6 mm if scanning parallel to their thickness and a potential lateral resolution of 23.4 mm if scanning parallel to their width. These lateral resolutions can be improved by scaling these electrodes down to the MEMS scale, however care

would need to be taken to ensure the array still has a large enough sense area such that the even smaller changes in capacitance can be detected.

2.6 Chapter Summary

This chapter presented the development of two variable spatial wavelength electrodes arrays to be used to make high frequency EQS sensors. First the models governing the electrode array design, (2.1) to (2.7), were presented along with design requirements derived from them. The four design requirements were:

1. Maximize the changes in capacitances measured by the EQS sensors,
2. Minimize the size of the smallest detectable feature (maximize resolution),
3. Maximize how well the electrode arrays follow a parallel plate capacitor model,
4. Design the electrode array such that it can be easily fabricated and attached to the high frequency drive electronics PCB.

Following this, a design was presented to construct the electrode array from the buried traces in the high frequency drive electronics PCB. Limits in the thickness of the PCB's traces and therefore the sense electrodes size resulted in this design having an insufficient sense area to detect changes in capacitance. In response, a bench-level experiment was conducted where a simple, unguarded electrode array with a much larger sense area was used to detect a change in capacitance. Building upon this, multiple strategies and concepts were conceived to create two variable spatial wavelength, guarded electrode arrays with millimeter-scale features and to attach them to the drive electronics PCB. Two different spatial wavelength EQS sensors were developed from these concepts that could each successfully measure a change in capacitance due to a variation in the thickness of an air gap target.

Chapter 3

Initial Test Fixture Design & Experiments

This chapter presents an initial test fixture for positioning the high frequency EQS sensors relative to the aluminum base with micron resolution. Figure 3-1 depicts this test fixture. This test fixture is used to step the sensors away from the base to produce a variable air gap target and is used to sweep the sensors across a target mounted on the base.

First the design requirements for this initial test fixture are presented along with components specified to satisfy those requirements. This initial test fixture is used to step the buried trace EQS senor (Section 2.3), the simple EQS sensor (Section 2.4), and the two variable spatial wavelength EQS sensors (Section 2.5.2) from an aluminum base to verify that variations in the thickness of an air gap target produce a change in capacitance. For the 2x1 long-wavelength sensor, the measured capacitance is recorded at multiple steps and compared to its model. Both the measured and modeled capacitances inversely decrease as the air gap increases. Following this experiment, the initial test fixture is used to step the 2x1 long-wavelength sensor from completely off to completely on a strip of Kapton tape to verify that changes in a target's permittivity produce a change in capacitance. Both the measured and modeled capacitances increase as the senor moves onto the Kapton tape. Both this initial Variable Air Gap Experiment and initial Dielectric Step Experiment are performed jointly

with Rakesh Kumar. They both reveal tilt between the 2x1 long-wavelength sensor and the aluminum base. To minimize the effect of this tilt in following experiments, the test fixture is redesigned (Section 4.2).

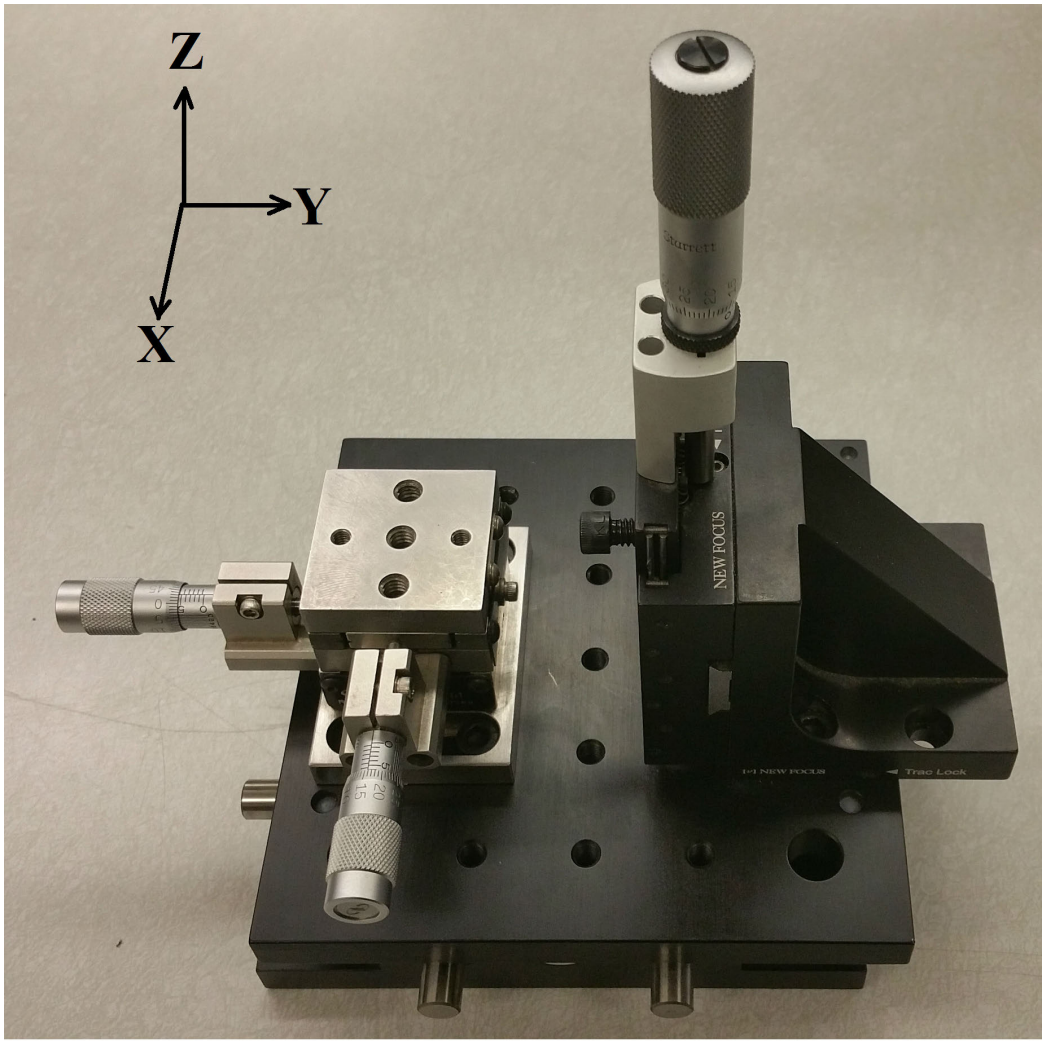

Figure 3-1: Initial test fixture to position the EQS sensor relative to the aluminum base. The sensor sits on the XY stage which allows the air gap between the sensor and target to vary and allows the sensor to sweep over the target horizontally. The target sits on an aluminum base on the Z stage which lets the sensor sweep over the target vertically.

3.1 Initial Test Fixture Design Requirements

The initial test fixture is originally designed to position the buried trace sensor orthogonally to a target and sweep the sensor across the target to see if a change in capacitance can be detected. However when the buried trace sensor could not detect a change in capacitance, this test fixture is used with the simple sensor and then finally with the two variable spatial wavelength sensors. To design this test fixture, a list of design requirements is first compiled:

Variable Target Thickness

According to (2.1) and (2.2), the capacitance measured by the EQS sensor is inversely proportional to the thickness of the gap between the EQS sensor and the aluminum base. Thus the test fixture should be able to change the distance between the sensor and the base to: (1) vary the thickness of the air gap between the sensor and the base and (2) allow for different thickness targets mounted on the base.

Planar Sweep

Since the primary goal is to explore using EQS sensors as an imaging tool, the test fixture should be able to sweep the sensor over a target mounted on the base, maintaining a fixed orthogonal distance between the sensor and the base.

Bidirectional Sweep

By (2.7), electrode pairs with non-square footprints will not have equal lateral resolutions in both Cartesian directions. Even with square-footprint electrode pairs however, electrode arrays may not have the same number of electrode pairs in both Cartesian directions, resulting still in a different resolution on both directions. As a result, the test fixture should be able to move the EQS sensor in either Cartesian direction coplanar to the target depending on the desired resolution of the scan.

Resolution

By (2.7), the lateral resolutions of an electrode array with millimeter-scale features will be millimeter-scale. In addition, the capacitance measured by the EQS sensors is very sensitive to the distance between the electrode array and the aluminum base according to (2.1) and (2.2). Therefore, the test fixture should be able to move the EQS sensor with high resolution.

Range of Travel

To be able to sweep the EQS sensor across several features on a target, the test fixture should have a large range of travel relative to the EQS sensor's lateral resolutions.

Load Capacity

Since the EQS sensor will not make physical contact with the target, components of the test fixture will not need to support high loads.

Angular Deviation

The test fixture should be able to move the EQS sensor with minimal angular deviation from the desired direction of motion.

With these design requirements compiled, a test fixture can now be designed.

3.2 Initial Test Fixture Design

As shown in previously in Figure 3-1 and now in Figure 3-2, the initial test fixture consists of two components: 1) a Newport ULTRAlign Integrated Crossed-Roller Bearing XY Linear Stage (Model: 461-XY-M) with two SM-13 Vernier Micrometers and 2) a Newport Triple Divide Z Axis Translation Stage (Model: 9064-Z) with an SM-25 Vernier Micrometer. The buried trace EQS sensor and other EQS sensors are mounted to the XY linear stage while the target is mounted to the Z linear stage. Turning the micrometer driving the X axis of the XY linear stage horizontally sweeps the sensor across the target while turning the micrometer driving the Z linear stage

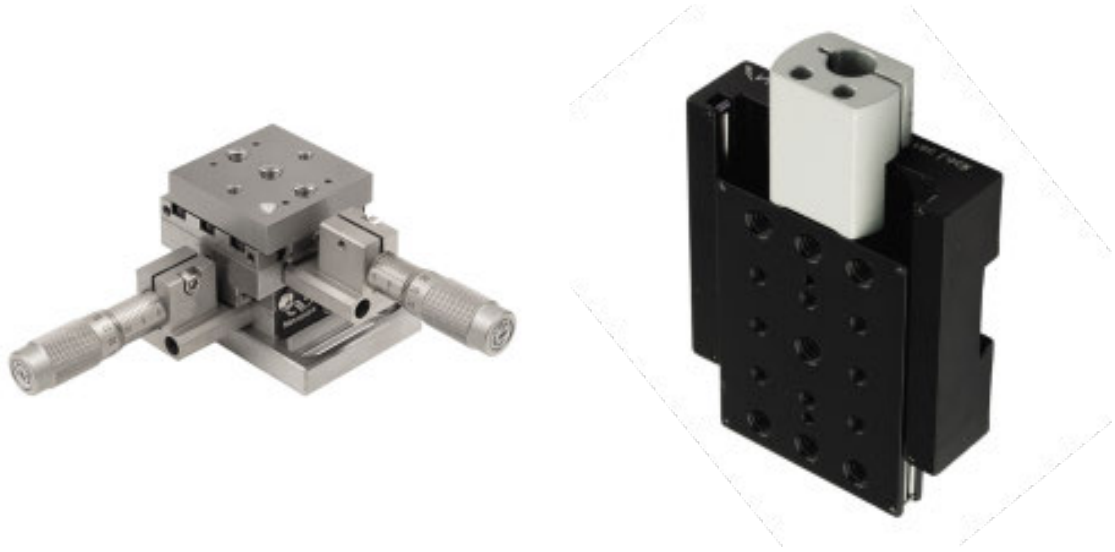

(a) Newport ULTRAlign Integrated Crossed-Roller Bearing XY Linear Stage (Model: 461-XY-M) with two SM-13 Vernier Micromters.

(b) Newport Triple Divide Z Axis Translation Stage (Model: 9064-Z) without an SM-25 Vernier Micrometer.

Figure 3-2: Linear, micrometer-driven stages used in the initial test fixture.

vertically sweeps the sensor across the target. Turning the micrometer controlling the Y axis of the XY stage changes the sensor's orthogonal distance from the base.

We chose a Newport ULTRAlign Integrated Crossed-Roller Bearing XY Linear Stage as it satisfies multiple design requirements. By moving the EQS sensor both orthogonal (motion along the Y axis) and parallel to the base (motion along the X axis), this XY stage can vary an air gap target and horizontally sweep the EQS sensor across other targets mounted on the base. In addition, this stage has a 13 mm range of travel in both Cartesian directions. Since the potential resolution of a horizontal sweep with the buried trace EQS sensor is 12.3 mm, 13 mm is adequate enough to step the sensor from completely off to completely on the Kapton strip to see a capacitance change due to a change in permittivity of the target. A separate concept for a high-bandwidth scanning system with a much larger range of motion is developed to horizontally sweep the sensor across multiple targets. The concept for this system is discussed in Section 6.2.

The two SM-13 Vernier Micrometers allow the EQS sensor on this XY stage to

travel with 1 μm of resolution over the 13 mm of travel. Given the thickness of the Kapton strip target used in later experiments is 65 μm, being able to control the air gap between the electrode array and the base on a micron-scale is also deemed adequate. Further, the XY stage has an angular deviation of less than 100 μrad over its range of travel. This translates to the sensor moving at most $\pm$1.3 μm orthogonal the base during a horizontal sweep. Since 1.3 μm is about the resolution which the XY stage can position the sensor orthogonally to the base, this angular deviation is acceptable.

We chose the Newport Triple Divide Z Axis Translation Stage (Model: 9064-Z) as it satisfies the remaining design requirements not covered by the XY stage. By vertically moving the base parallel to the buried trace EQS sensor, the Z stage can vertically sweep the sensor across targets mounted on the base. With both stages, the sensor can bidirectionally sweep across targets. Further, the Z stage has a 25 mm range of travel. Given the potential resolution of a vertical sweep with the buried trace EQS sensor is 1.3 mm, this range is as more than adequate. The Z stage can vertically sweep the sensor across multiple targets.

The SM-25 Vernier Micrometer has a micron resolution like the SM-13 Vernier Micrometer. This is desirable as the sensor can be stepped vertically across the target in increments finer than the vertical sweep's potential resolution. Further, each step would have the same resolution as the steps in the horizontal sweep. Lastly, the Z stage also has an angular deviation of less than than 100 μrad over its range of travel. Even though this means the target can move up to $\pm$2.5 μm orthogonal to the sensors during a vertical sweep, this is acceptable as this is again about the resolution which the XY stage can position the EQS sensor relative to the base.

3.3 Initial Experiments

Originally, the initial test fixture is used to determine if the buried trace EQS sensor can detect a change in capacitance due to changes in the thickness of an air gap target. With the buried trace EQS sensor unable to detect a capacitance

change, the simple EQS sensor is built. Using the initial test fixture, the simple EQS successfully measured a change in capacitance due to a variable air gap. With the success of the simple EQS sensor, the two variable spatial wavelength EQS sensors are constructed and tested with the initial test fixture. Both of these EQS sensors measured a change in capacitance due to variation in the thickness of the air gap target. In each experiment, the different sensors are connected to an Agilent 4395A impedance analyzer and the changes in capacitance are detected as changes in the impedance analyzer's measured impedance.

To convert these changes in impedance to changes in capacitance, Rakesh Kumar developed a circuit model for the EQS sensors which includes the circuitry for the high frequency drive electronics, the board parasitics, and the capacitance between the electrode array and the target [5]. Figure 3-3 shows this circuit model. Supplying this model to the software program Advanced Design System (ADS) by Agilent Technologies along with the impedance data at a given point, ADS is able to find both the board parasitics and the capacitance between the electrode array and the target at that point. For ADS to perform this, the impedance data at a given point needs to consist of the measured impedance's magnitude, $|Z|$, and phase, ϕ_Z, over at least three frequencies. In all the experiments, the impedance data is given at 201 frequencies between 1 to 500 MHz.

Now that measured impedance can be converted into measured capacitance, the next step is to verify the models for the capacitance between the electrode array and target, (2.5) and (2.6), for single and double dielectric targets respectively. According to the model for a single dielectric target such as a variable air gap, the capacitance should inversely change as the thickness of the target changes. Thus the test fixture is used to back the long-wavelength sensor away from the aluminum base to verify that the measured capacitance inversely decays as the thickness of the air gap increases. Further, both models predict the capacitance between the electrode array and target should increase as the permittivity of the target increases. To test this, the test fixture is used to step the long-wavelength sensor from completely off to completely on a strip of Kapton. Both of these experiments are done jointly with Rakesh Kumar.

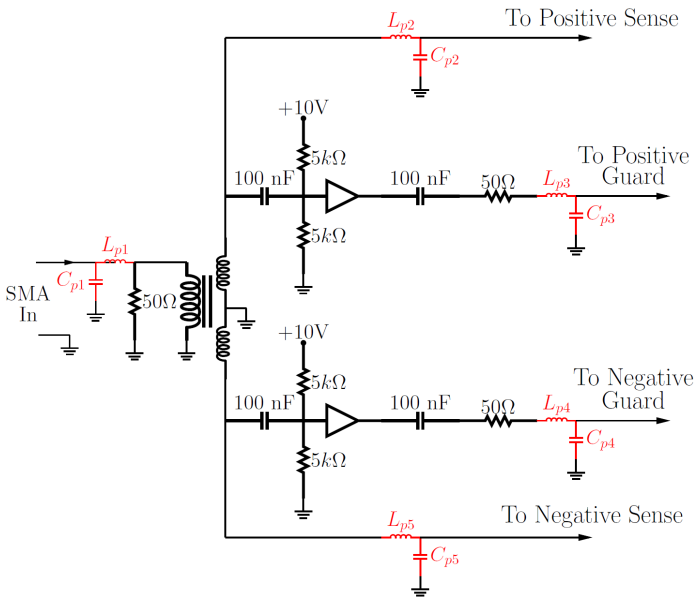

Figure 3-3: Model of high frequency drive electronics with parasitic inductances and capacitances in red taken from [5].

3.3.1 Initial Variable Air Gap Experiment

Moving an EQS sensor orthogonally to the aluminum base produces a variable air gap target. This can be modeled by the capacitance models for a single dielectric target, (2.5). According to this model, as the thickness of the target, the air gap in this case, increases, the capacitance measured should decrease inversely. To validate this model, the long-wavelength sensor is positioned 20 μm away from the aluminum base and stepped away from it using the initial test fixture. To position the sensor, the first two steps of the alignment procedure described in Section 4.3.2 are used. The EQS sensor is stepped in increments of 10 μm until the air gap is 100 μm thick and then in increments of 50 μm until the air gap is 700 μm thick.

To record the capacitance between the long-wavelength electrode array and the air gap target, the sensor is again connected to an Agilent 4395A impedance analyzer. Each time the EQS sensor is stepped to increase the air gap, the measured impedance is averaged eight times and recorded from 1 to 500 MHz. Then the measured impedances at each step are passed through ADS by Rakesh Kumar (Section 3.3) to determine the measured capacitance at each step. The resulting capacitance

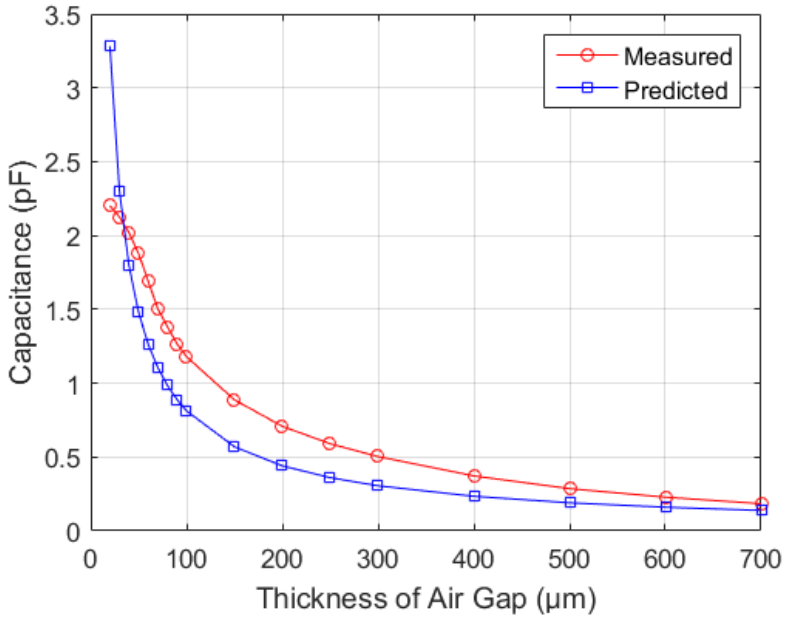

Figure 3-4: Measured vs. predicted capacitance of the long-wavelength EQS sensor due to a variable air gap using the initial test fixture. The predicted capacitance is obtained from the single dielectric parallel plate + fringe field model, (2.5).

profile measured by the long-wavelength sensor as the air gap increases is shown in Figure 3-4. The capacitance predicted by the parallel plate + fringe field model for a single dielectric, (2.5), is shown with it.

The capacitance profile measured by the long-wavelength sensor is fairly close to the predicted capacitance profile. Both decrease inversely as the air gap is increased. This validates our approximation that electric fields of sense electrodes near a target against a conductive base are relatively straight. Given the validation of this approximation, we can continue to model the capacitance between the electrode array and target as series and parallel combinations of parallel plate and fringing field capacitors, (2.5) and (2.6).

However, there are some discrepancies between the measured capacitance profile and the predicted capacitance profile. First, the measured capacitance levels off as the thickness of the air gap approaches 20 μm. This is likely due to the long-wavelength electrode array not truly being coplanar with the aluminum base. Instead, there is some tilt between the electrode array and the base such that near 20 μm, one part

of the electrode array contacts the base. As initial test fixture attempts to move the electrode array closer than 20 μm, the electrode array stays in place and the drive electronics PCB compresses instead. Thus near 20 μm, the electrode array is always the same distance from the base, resulting in a constant air gap thickness and in turn a constant measured capacitance.

The other discrepancy is that the measured capacitance is higher than the predicted capacitance. This is likely due to two sources. First, the single dielectric fringe field model 2.3 may not fully capture the additional capacitance due to slight differences in potential between the sense electrodes and their guard electrodes. Second, the measured capacitance is calculated by ADS from the impedance measured. This numerical conversion by ADS may not be perfect. Extra capacitance could be added to the measured capacitance instead of a parasitic capacitance. In response, Rakesh Kumar looked into better optimizing ADS's conversion from impedance to capacitance. In the meantime, a second experiment is performed to verify that the capacitance model for a two dielectric target, (2.6), can predict the change in capacitance due to a change in the permittivity of the target.

3.3.2 Initial Dielectric Step Experiment

Knowing the parallel plate + fringe field models reasonably predict the capacitance changes measured by the long-wavelength sensor due to changes in the geometric properties of a single dielectric target (a variable air gap), the next step is to verify that the models also reasonably predict the capacitance changes measured by the long-wavelength sensor due to changes in the material properties of a target (dielectric step). According to the parallel plate model + fringe field model for a two dielectric target (2.6), increasing the permittivity of one layer should produce an increase in capacitance between the electrode array and the target.

To validate this, a 65 μm thick strip of Kapton tape is placed horizontally across the aluminum base. Using the same alignment procedure used in the initial Variable Air Gap Experiment and described by the first two steps in Section 4.3.2, the long-wavelength sensor is placed 100 μm away from the base. This would correspond to

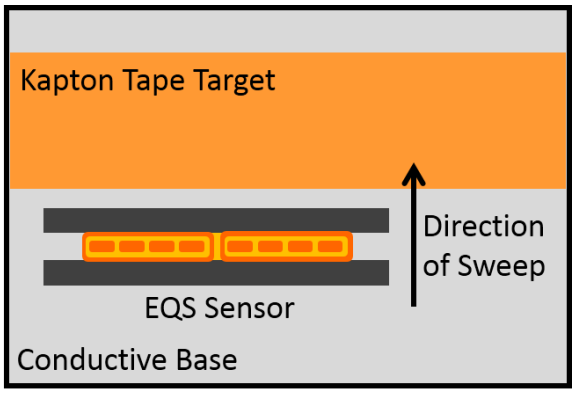

Figure 3-5: Diagram of an EQS sensor sweeping over a dielectric step.

a 100 μm air gap when the sensor is completely off the Kapton strip and a 35 μm air gap when on the Kapton strip. The sensor is laterally stepped in the vertical direction from completely off to completely on the Kapton strip in increments of 100 μm. Figure 3-5 depicts this setup. As the sensor moves onto the strip of Kapton, the capacitance measured should increase as Kapton has a higher permittivity than air.

The EQS sensor is again connected to an Agilent 4395A impedance analyzer. The measured impedance is averaged eight times and recorded from 1 to 500 MHz at each step. To obtain the measured capacitances at each step, the data is passed through ADS by Rakesh Kumar (Section 3.3). The resulting capacitance profile measured by the long-wavelength sensor as it steps from completely off to completely on a strip of Kapton is shown in Figure 3-6. The capacitance predicted by the parallel plate + fringe field model for a two dielectric target, (2.6), is shown with it.

Both the capacitance profile predicted by the model and measured follow the same trend. They both begin and stay relatively flat at a low capacitance. This corresponds to the long-wavelength sensor being completely off the strip of Kapton. Then both capacitance profiles rapidly increase to a higher capacitance. This corresponds to the sensor transitioning from completely off to completely on the strip of Kapton. Finally both capacitance profiles reach a high capacitance and level out relatively. This corresponds to the sensor being completely on the strip of Kapton.

The measured capacitance profile is flat at the beginning and end of the Kapton step relative to its transition. Relative to the predicted capacitance profile, the

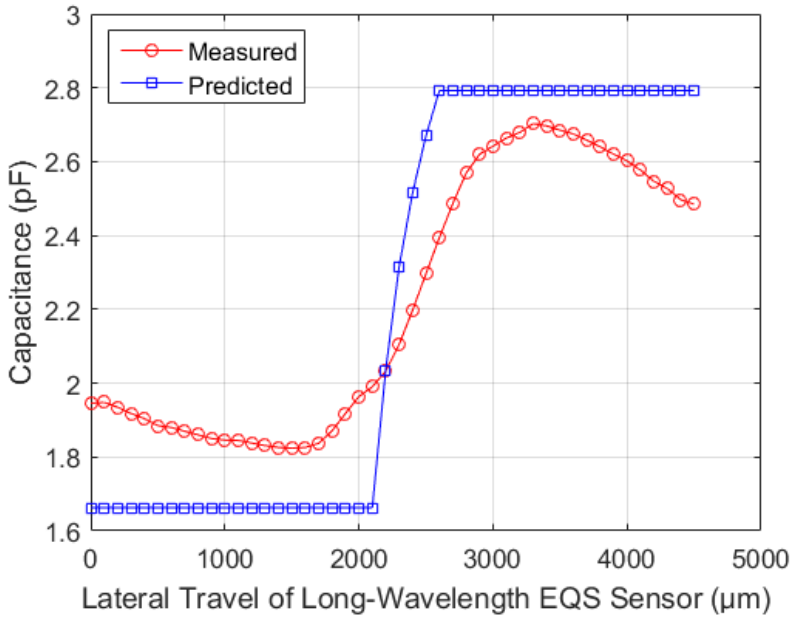

Figure 3-6: Measured vs. predicted capacitance of the long-wavelength EQS sensor while sweeping over a dielectric step using the initial test fixture. The predicted capacitance is obtained from the double dielectric parallel plate + fringe field model (2.6).

measured capacitance profile has a downward slop in both of these regions. This downward slope exists because the sensor's electrode array is not truly coplanar with the aluminum base. The top of the base is tilted slightly away from the electrode array. Thus as the sensor sweeps vertically, the air gap gradually increases which produces a gradual decrease in the capacitance measured. The difference in slope before and after the Kapton step exists because of the difference in the average thickness of the air gap before and after the step. Before the step, the dielectric consists of only air, thus this gradual increase is small relative to the total thickness of the air gap. However after the step, the dielectric consists of mostly Kapton so this gradual increase is now much larger relative to the thickness of the air gap. To further determine the agreement between the measured and predicted capacitance profiles, change in capacitance due to this tilt needs to be removed.

3.4 Misalignment in Initial Experiments

To determine the tilt of the aluminum base relative to the long-wavelength electrode array, the distance between the electrode array and the based is calculated for each point on the measured capacitance profile. The tilt can be determined from the slope of the relative flat sections of this distance profile. Since the aluminum base has a constant tilt throughout the experiment, the tilt can be calculated from the relatively flat section before or after the Kapton step. Given the parallel plate + fringe field model for a single dielectric target is simpler than for a double dielectric target, we calculate the distance between the electrode array and base before the Kapton step and use its slope to determine the tilt.

Solving (2.5), the thickness of the air gap target, which is equal to the distance between the long-wavelength electrode array and the aluminum base, is

$$d_{\text{air}} = -\frac{\pi A \Delta}{4\left(A - \Delta w \mathbb{W}\left\{\frac{A \exp\left(\frac{A}{\Delta w} + \frac{C\pi}{4\epsilon w}\right)}{bw}\right\}\right)}, \tag{3.1}$$

where C is the measured capacitance, and $\mathbb{W}$ is the Lambert $\mathbb{W}$-function. This can be reduced by acknowledging that for a 100 μm thick air gap, (2.1), (2.3) and (2.5) predict

$$C_{\text{Parallel-Single}} + C_{\text{Fringe-Single}} \approx 1.5\ C_{\text{Parallel-Single}}, \tag{3.2}$$

and

$$C_{\text{Measured}} \approx 2.35(C_{\text{Parallel-Single}} + C_{\text{Fringe-Single}}). \tag{3.3}$$

Using these two approximations,

$$d_{\text{air}} \approx 2.35 \cdot 1.5 \cdot \frac{\epsilon_{\text{air}} A}{C_{\text{Measured}}}. \tag{3.4}$$

Using this approximation, Figure 3-7 shows the distance between the long-wavelength electrode array and the aluminum base before the sensor stepped onto the Kapton strip. The slope of this distance curve reveals the top of the base is tilted 0.34° away

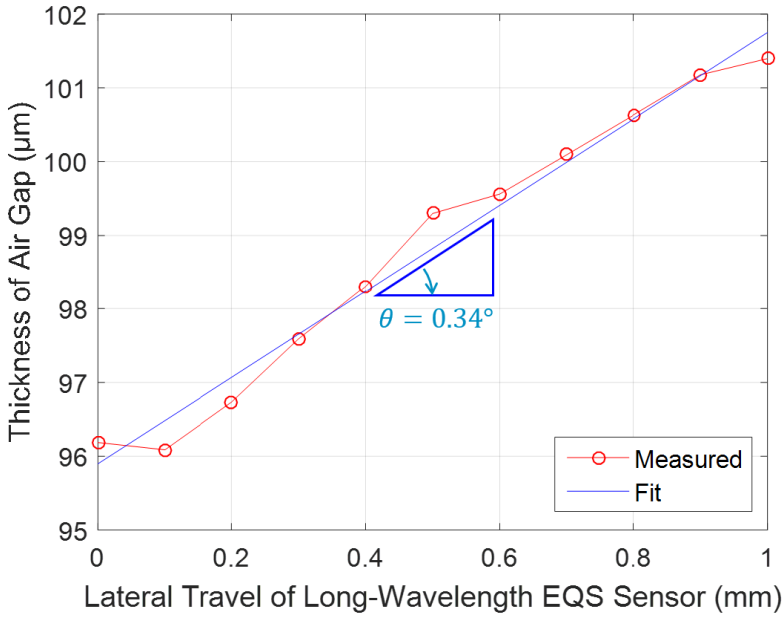

Figure 3-7: Tilt of the aluminum base with respect to the long-wavelength electrode array in the initial Dielectric Step Experiment in Section 3.3.2.

from the sensor. This translates to the sensor moving 30 μm away from the aluminum base as it travels from completely off to completely on the Kapton strip. This proves problematic as this is 30% of the distance the sensor is positioned from the base.

Using the double dielectric parallel plate + fringe field model, (2.6), and the amount this model deviates from the measured capacitance at 100, μm (3.3), the change in capacitance due to the tilt is removed from the measured capacitance. Figure 3-8 shows the tilt-corrected capacitance profile measured by the long-wavelength sensor as it steps from completely off to completely on a strip of Kapton. With the tilt-correction, the predicted and measured capacitance profiles have greater agreement. The measured capacitance profile before and after the Kapton step is flatter like the predicted capacitance profile and the change in capacitance due to the Kapton step are now roughly equal in both curves.

The one major discrepancy is that the predicted capacitance profile transitions faster than the measured capacitance profile due to the Kapton step. This is explained by the number of steps it takes the sensor to travel from completely off to completely on the Kapton strip in the model relative to the experiment. The model assumes that

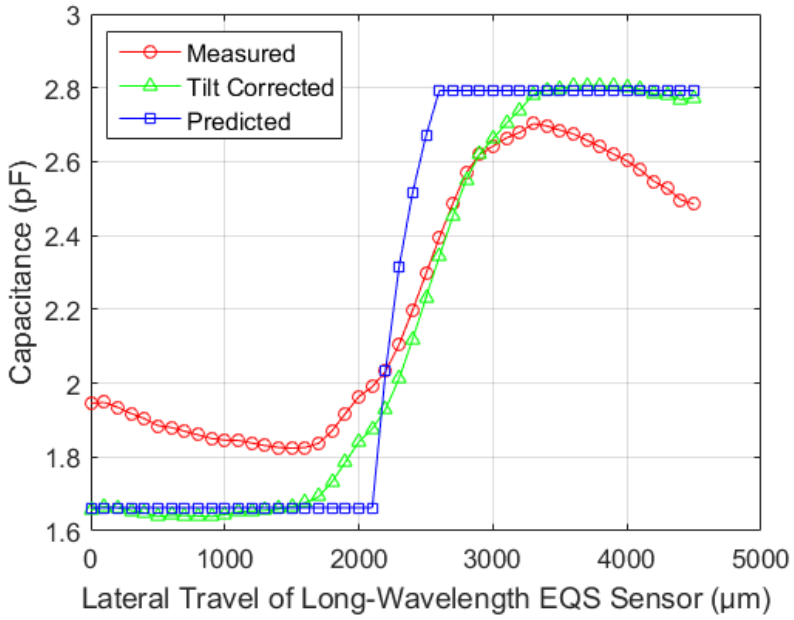

Figure 3-8: Tilt-corrected measured vs. predicted capacitance of the long-wavelength EQS sensor while sweeping over a dielectric step using the initial test fixture. The predicted capacitance is from the double dielectric parallel plate + fringe field model (2.6).

the edge of the long-wavelength electrode array is perfectly parallel with the edge of the Kapton strip as the sensor moves onto it. However, in the experiment, there is a slight angle between the edge of the electrode array and the edge of the Kapton strip. Hence, the sensor begins to move onto the Kapton strip earlier and finishes moving completely onto the Kapton strip later in the experiment than in the model, resulting in a longer transition for the experiment.

3.5 Chapter Summary

This chapter presented an initial test fixture able to position an EQS sensor relative to an aluminum base with micron-resolution. Further this test fixture is able to step the sensors away from the base to produce a variable air gap target and is able to sweep the sensors across a target mounted on the base. First the design requirements for the test fixture were given:

1. The sensor can be moved orthogonal to the aluminum base.

2. The sensor can be swept in two Cartesian directions over the base.

3. The sensor can be positioned with high resolution.

4. The sensor has a large range of travel during its sweeps.

5. The test fixture does not need to support high loads.

6. The test fixture has low angular deviation when moving the sensors.

Based on these design requirements, the test fixture has two components. A Newport ULTRAlign Integrated Crossed-Roller Bearing XY Linear Stage (Model: 461-XY-M) with two SM-13 Vernier Micrometers allows the EQS sensor to move orthogonally to the aluminum base and to sweep over it horizontally. A Newport Triple Divide Z Axis Translation Stage (Model: 9064-Z) with an SM-25 Vernier Micrometer allows the EQS sensor to vertically sweep over the base.

This test fixture was used to move the buried EQS sensor, simple EQS sensor, and the variable spatial wavelength EQS sensors away from the base to verify that they could measure a change in capacitance due to a change in thickness of a variable air gap target. After successfully measuring a change in capacitance with the simple sensor and the variable spatial wavelength sensors, the test fixture was again used to step the long-wavelength EQS sensor away from the base. The goal was to determine if the measured capacitance inversely decayed as the air gap increased as predicted by the single dielectric parallel plate + fringe field model, (2.5). The measured capacitance mostly agreed with the predicted capacitance, validating our approximation that the electric fields of sense electrodes near a target against a conductive base are relatively straight. Disagreement between the measured and predicted capacitances occurred when the sensor was roughly 20 μm from the base as tilt between the sensor and base led to the sensor contacting the base at that distance.

Afterwards, the test fixture stepped the long-wavelength sensor from completely off to completely on a Kapton strip to verify the sensor could measure a change in capacitance due to a change in the material properties of a target. As predicted by

the double dielectric parallel plate + fringe field model, (2.6), the measured capacitance increased when the sensor moved onto the Kapton strip since Kapton has a higher permittivity than air. However, the measured capacitance profile contained a downward slope before and after the step as the base was tilted away from the EQS sensor roughly 0.34°. After accounting for this tilt, the measured capacitance curve tracked the predicted capacitance curve reasonably well.

Chapter 4

Test Fixture Redesign

This chapter presents the redesign of the test fixture used for positioning and sweeping the high frequency EQS sensors with micron-resolution. The redesign of the test fixture is shown in Figure 4-1. The test fixture required redesigning as it provided no means to adjust tilt between the sensor and the aluminum base. Using this adjustment to minimize the tilt is necessary as it would minimize several disagreements between the measured and predicted capacitance profiles in the initial Variable Air Gap Experiment (Section 3.3.1) and initial Dielectric Step Experiment (Section 3.3.2).

To redesign the test fixture, we first identified sources that cause undesired changes in the distance between the EQS sensors and the base, and in turn undesired changes in capacitance. From these sources of misalignment, additional design requirements are compiled. To account for the horizontal tilt in the initial Variable Air Gap Experiment, a rotation stage is added to the initial test fixture underneath the XY stage. To account for the vertical tilt in the initial Dielectric Step Experiment, a tilt stage is designed and added underneath the Z stage. To confirm these new stages reduced the sources of misalignment, both the long-and short-wavelength EQS sensors are swept vertically and horizontally across the aluminum base. Changes in the capacitance due to misalignments in these experiments are compared to the noise level of the system and found to be on the same order of magnitude.

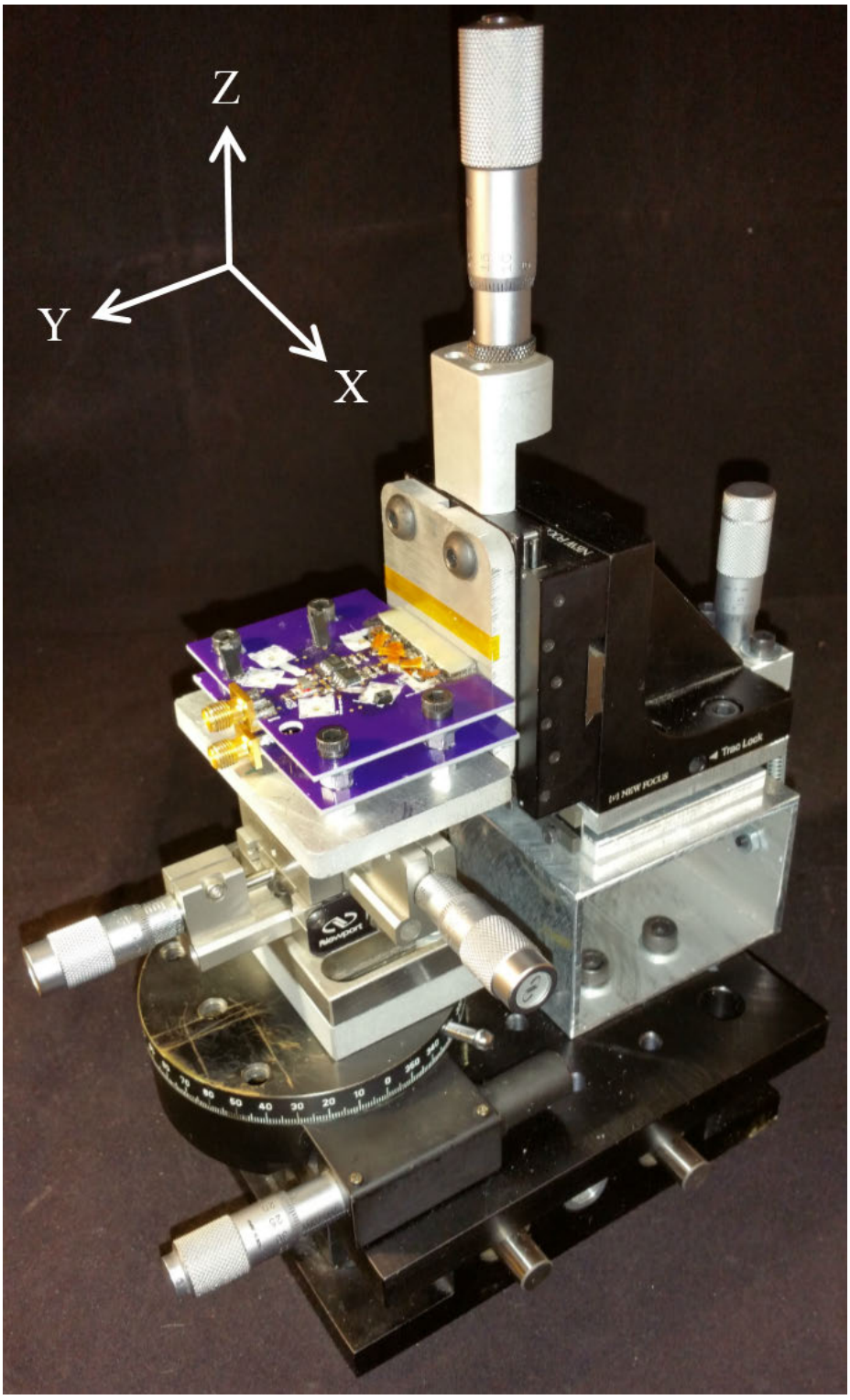

Figure 4-1: Final test fixture to position the EQS sensor relative to the aluminum base. A rotation stage has been placed under the XY stage to account for the horizontal misalignments shown in Figure 4-2c,d. A flexure tilt stage has been placed under the Z stage to account for the vertical misalignments shown in Figure 4-2a,b.

4.1 Sources of Misalignment

According to the single and double dielectric capacitance models, undesired changes in capacitance are caused by undesired changes in the distance between the sensor and the base. There are three possible sources which can cause undesired changes in the distance between the sensor and the base. An additional source of misalignment exists; instead of affecting the distance between the sensor and the base however, this misalignment causes the sensor to prematurely contact the base as the two are brought closer together. These sources of misalignment are displayed in Figure 4-2.

First the Z stage's axis of motion can be tilted relative to the EQS sensor. Thus as the Z stage moves the base laterally, the base moves slightly orthogonal relative to the sensor. In addition, the aluminum base itself can be tilted vertically. This also causes the base to move slightly orthogonal relative to the sensor as the Z stage moves the base laterally. Both of these misalignments are categorized as vertical misalignments as the Z stage moves vertically in order to sweep the sensor over the base. Further, these two sources of misalignment can account for the changes in measured capacitance due to tilt in the initial Dielectric Step Experiment.

Similar to the Z stage, the XY stage's axes of motion can be tilted relative to the sensor. In particular, tilt in the XY stage's X axis of motion would cause the sensor to move slightly orthogonal relative to the base as the sensor is laterally swept over the base by the XY stage. Alternatively, the sensor itself can be tilted horizontally relative to the base. However, this would not cause the sensor to move slightly orthogonal relative to the base as the XY stage sweeps the sensor laterally over the base. Instead the sensor would not be able to move as close to the base as a coplanar sensor. This would happen as the closest edge of the sensor would prematurely contact the base as the sensor and base are brought together. This tilt of the sensor relative to the base explains why the measured capacitance levels off near the base in the initial Variable Air Gap Experiment. Both of these misalignments are categorized as horizontal misalignments as they only occurred due to the horizontal movement of the XY stage.

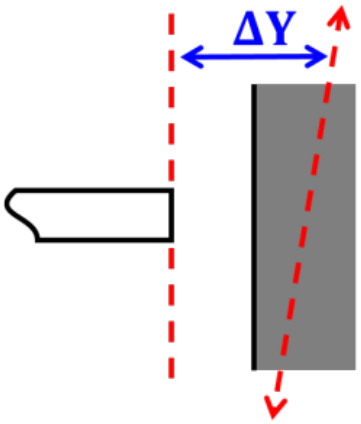

(a) Vertical misalignment due to tilt in the Z (vertical) axis of motion relative to the EQS sensor.

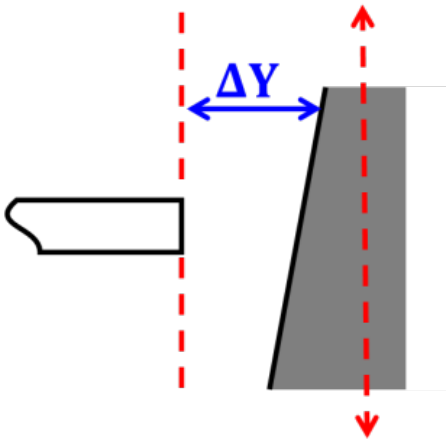

(b) Vertical misalignment due to vertical tilt in the base relative to the EQS sensor.

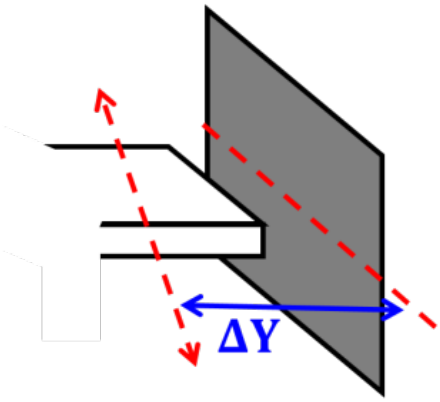

(c) Horizontal misalignment due to tilt in the X (horizontal) axis of motion relative to the base.

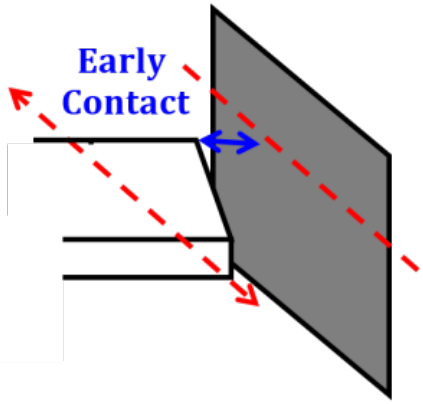

(d) Horizontal misalignment due to horizontal tilt in the EQS sensor relative to the base.

Figure 4-2: Sources of misalignment between the EQS sensor and the aluminum base. Sources (a)-(c) lead to changes in the distance between the sensor and the base ΔY, and in turn changes in measured capacitance as the EQS sensor is swept laterally across the base. Source (d) causes the sensor to prematurely contact the base as the sensor is brought closer to the base.

4.1.1 Additional Test Fixture Design Requirements

By categorizing these sources of misalignment into two groups, two new design requirements arise for the redesign of the test fixture:

Vertical Misalignment

Vertical tilt in the Z stage's axis of motion and in the aluminum base relative to the EQS sensor cause the base to move slightly orthogonal relative to the sensor when the Z stage moves. The redesigned test fixture should be able to remove this slight orthogonal travel by counter-tilting the Z stage.

Horizontal Misalignment

Horizontal tilt in the XY stage's axis of motion causes the sensor to move slightly orthogonal relative to the base when the XY stage moves along its X axis. Additionally, horizontal tilt in the sensor prevents it from traveling near the base without prematurely contacting it. Thus the redesigned test fixture should be able to remove this slight orthogonal travel by counter-rotating the XY stage.

In addition to meeting these new design requirements, the redesigned test fixture still has to meet the initial design requirements listed in Section 3.1.

4.2 Redesign

The completely redesigned test rig is shown earlier in Figure 4-1. To account for the initial design requirements, the redesigned test fixture still uses the Newport ULTRAlign Integrated Crossed-Roller Bearing XY Linear Stage (Model: 461-XY-M) with two SM-13 Vernier Micrometers and the Newport Triple Divide Z Axis Translation Stage (Model: 9064-Z) with an SM-25 Vernier Micrometer. To account for the horizontal sources of misalignment, a rotation stage is added underneath the XY stage as described in the following section. To account for the vertical sources of

misalignment, a tilt stage is added underneath the Z stage. The tilt stage is designed from the measured tilt in the initial Dielectric Step Experiment (Section 3.3.2). Its design and development are described in Section 4.2.2. Lastly spacers are added to keep the EQS sensor's height at the center of the Z stage's range of motion.

4.2.1 Rotation Stage

We chose a Melles Griot Micrometer-Driven Rotation Stage (Model: 98 mm Dia.) as the rotation stage for its range of travel and resolution. It is shown in Figure 4-3. This rotation stage has a range of 10° with a resolution of 0.0083°. Since there is no measure of the horizontal tilt in the initial stage, we approximated the horizontal tilt to be roughly equal to the vertical tilt, 0.34°. With this approximation, the rotation stage's range of travel is roughly 30 times greater than the horizontal tilt and its resolution is roughly 40 times finer than the horizontal tilt. Further, a horizontal tilt of 0.0083° (the maximum alignment the rotation stage offers) translates to the EQS sensor moving at most ± 1.88 μm orthogonal to the base during a horizontal sweep. This is about the resolution the XY stage can position the sensor orthogonally to the base. As a result, we found this rotation stage to be adequate.

4.2.2 Tilt Stage

A custom micrometer-driven flexure stage is used as the vertical tilt stage. Figure 4-4 depicts the concept for this custom tilt stage. The stage consists of two plates connected by a strip of spring steel, a pair of extension springs, and a micrometer. The strip of spring steel is held to each plate by a bar with screws. The micrometer rests on the top plate, held in place by a set screw, and contacts a ball on the bottom plate. The ball ensures the micrometer only makes a single point of contact with the bottom plate. Turning the micrometer causes the distance between the two plates to change at one end of this assembly. Since the distance between the two plates at the other end is fixed by the spring steel strip, this motion causes the strip to bend, tilting the top plate relative to the bottom plate.

Figure 4-3: Melles Griot Micrometer-Driven Rotation Stage (Model: 98 mm Dia.) added in the test fixture redesign to account for horizontal misalignment.

The micrometer can only set the distance between the two plates while in contact with both of them. However, when the displacement set by the micrometer is less than the height of the spring steel strip, the micrometer will cease contact with the ball on the bottom plate. The pair of extensions springs account for this issue. By having the distance between the springs' attachment points on the two plates always greater than the springs' relaxed lengths, the springs will always attempt to pull the two plates together. This compressive preload causes the micrometer to stay in contact with the ball on the bottom plate even when the applied distance is less than the height of the spring steel strip. This allows the micrometer to tilt the top plate both toward and away from the bottom plate.

Tilt Stage Modeling

The majority of the top plate's dimensions are determined by the bottom of the Z stage as the top plate will be mounted to it. The majority of the bottom plate's dimensions are the same as the top plate for simplicity. The height of the spring steel strip and the length of the top plate are determined by the range of tilt the stage

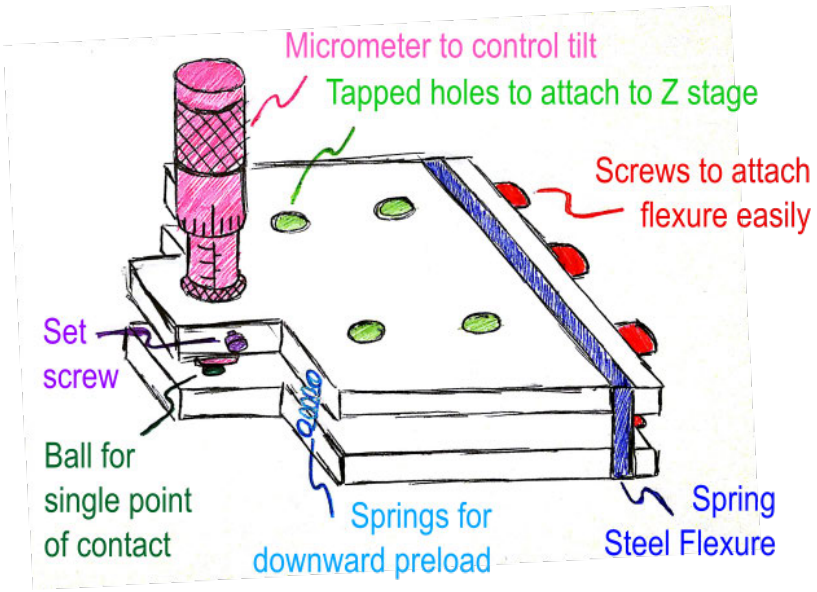

Figure 4-4: Concept a micrometer-driven flexure tilt stage.

should provide. We chose the thickness of the strip such that the strip will not yield at the stage's max tilt. To see how the strip's height l_2, and the length of the top plate l_1, relate to the range of tilt $2\theta_2$, the stage is modeled as a vertical cantilevered beam with a horizontal cantilevered beam attached to its end and a vertical displacement δ_y applied to the end of the horizontal beam. This is depicted in Figure 4-5 with the top plate as beam 1 and the strip as beam 2.

The vertical displacement at the end of the top plate, Point A, is

$$\delta_y = \begin{bmatrix} 0 & 1 \end{bmatrix} \begin{Bmatrix} x_{A'} \\ y_{A'} \end{Bmatrix} - \begin{bmatrix} 0 & 1 \end{bmatrix} \begin{Bmatrix} x_A \\ y_A \end{Bmatrix}, \tag{4.1}$$

where $\{x_A \quad y_A\}^T$ and $\{x_{A'} \quad y_{A'}\}^T$ are the coordinates of Point A with respect to the origin, Point C, before and after the beams are deformed.

The coordinates of Point A before the beams are deformed are simply given by the dimensions of the beams:

$$\{x_A \quad y_A\}^T = \{l_1 \quad l_2\}^T, \tag{4.2}$$

while the coordinates of Point A after the beams are deformed can be found using

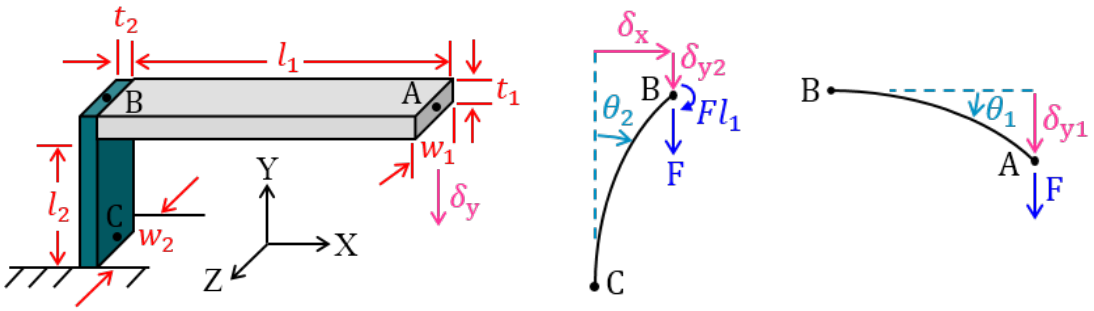

(a) Dimensions of the tilt stage.

(b) Forces and deflections of the tilt stage.

Figure 4-5: Model of the tilt stage with the top plate as beam 1 and the spring steel strip as beam 2.

2D Homogeneous Transformation Matrices (HTMs) [25]:

$$\{x_{A'} \quad y_{A'} \quad 1\}^{\mathrm{T}} = {}^{C}\mathbb{H}_{B}\ {}^{B}\mathbb{H}_{A}\ [\ 0 \quad 0 \quad 1\ ]^{\mathrm{T}}, \tag{4.3}$$

where ${}^{B}\mathbb{H}_{A}$ is the 2D HTM that relates the deformed position of Point A to Point B and ${}^{C}\mathbb{H}_{B}$ is the 2D HTM that relates the deformed position of Point B to Point C.

${}^{B}\mathbb{H}_{A}$ can be found by solving the bending of the top plate for the top plate's vertical deflection δ_{y1} and slope θ_1 at Point A:

$${}^{B}\mathbb{H}_{A} = \begin{bmatrix} \cos\theta_1 & -\sin\theta_1 & l_1 \\ \sin\theta_1 & \cos\theta_1 & \delta_{\mathrm{y1}} \\ 0 & 0 & 1 \end{bmatrix}, \tag{4.4}$$

$$\delta_{\mathrm{y1}} = -\frac{F{l_1}^3}{3E_1I_1}, \tag{4.5}$$

and

$$\theta_1 = -\frac{F{l_1}^2}{2E_1I_1}, \tag{4.6}$$

where F is the load at Point A needed to apply the total vertical displacement δ_{y}, E_1 is the modulus of elasticity for the top plate, and I_1 is the area moment of inertia for the top plate given by

$$I_1 = \frac{1}{12} w_1 {t_1}^3, \tag{4.7}$$

where w_1 and t_1 are the width and thickness of the top plate respectively.

${}^{C}\mathbb{H}_{B}$ can be found by solving the axial compression of the strip for the strip's vertical deflection δ_{y2} at Point B and the bending of the strip for the strip's horizontal deflection δ_{x} and slope θ_2 at Point B:

$$ {}^{C}\mathbb{H}_{B} = \begin{bmatrix} \cos\theta_2 & -\sin\theta_2 & \delta_{\mathrm{x}} \\ \sin\theta_2 & \cos\theta_2 & l_2 + \delta_{\mathrm{y2}} \\ 0 & 0 & 1 \end{bmatrix}, \tag{4.8} $$

$$ \delta_{\mathrm{y2}} = -\frac{F l_2}{E_2 A_2}, \tag{4.9} $$

$$ \delta_{\mathrm{x}} = \frac{F l_1 {l_2}^2}{2 E_2 I_2}, \tag{4.10} $$

and

$$ \theta_2 = -\frac{F l_1 l_2}{E_2 I_2}, \tag{4.11} $$

where E_2 is the modulus of elasticity for the strip, A_2 is the cross-sectional area of the strip given by

$$ A_2 = w_2 t_2, \tag{4.12} $$

and I_2 is the area moment of inertia for the strip given by

$$ I_2 = \frac{1}{12} w_2 {t_2}^3, \tag{4.13} $$

where w_2 and t_2 are the width and thickness of the strip respectively.

Since the deflection of the top plate and strip are small, $\sin\theta \approx \theta$ and $\cos\theta \approx 1$ by first-order approximation. This reduces

$$ {}^{B}\mathbb{H}_{A} \approx \begin{bmatrix} 1 & -\theta_1 & l_1 \\ \theta_1 & 1 & \delta_{\mathrm{y1}} \\ 0 & 0 & 1 \end{bmatrix} \tag{4.14} $$

and

$$ {}^{C}\mathbb{H}_{B} \approx \begin{bmatrix} 1 & -\theta_2 & \delta_{\mathrm{x}} \\ \theta_2 & 1 & 1_2 + \delta_{\mathrm{y2}} \\ 0 & 1 & 1 \end{bmatrix}. \tag{4.15} $$

Substituting (4.2), (4.3), (4.14) and (4.15) into (4.1):

$$ \delta_{\mathrm{y}} = l_1\theta_2 + \delta_{\mathrm{y1}} + \delta_{\mathrm{y2}}. \tag{4.16} $$

Substituting (4.5) to (4.7) and (4.9) to (4.13) into (4.16), the relationship between the vertical displacement applied by the micrometer and the range of motion is

$$ \delta_{\mathrm{y}} = \left[l_1 + \frac{1}{3} \cdot \frac{{l_1}^2}{l_2} \left(\frac{E_2 I_2}{E_1 I_1} \right) + \frac{I_2}{l_1 A_2} \right] \theta_2, \tag{4.17} $$

where the first term comes from the top plate tilting as the strip bends, the second term comes from the bending of the top plate, and the third term comes from the axial compression of the strip.

Since the spring steel strip is being used as a flexure, its thickness is very small compared to all the other dimensions. As a result, the strip's area moment of inertia is very small. This causes the first term of (4.17) to dominate, reducing it to

$$ \delta_{\mathrm{y}} \approx l_1\theta_2. \tag{4.18} $$

The max vertical displacement the micrometer can apply to pull the top and bottom plate together is less than the max vertical displacement it can apply to push them apart. This is because after the plates are pulled together the height of the strip, the points of the plates farthest from the strip contact. Using this smaller maximum as the max vertical displacement the micrometer can apply, the relationship between the height of the spring steel strip, the length of the top plate, and the stage's range of tilt is obtained:

$$ (\theta_2)_{\max} \approx \frac{1}{l_1} l_2. \tag{4.19} $$

Alternatively, this can be rearranged to provide the angular resolution of the stage R_{stage}:

$$R_{\text{stage}} \approx \frac{(\theta_2)_{\max}}{l_2} r_{\text{micrometer}} \approx \frac{1}{l_1} r_{\text{micrometer}} \tag{4.20}$$

where $r_{\text{micrometer}}$ is the linear resolution of the micrometer driving the stage.

At the stage's max tilt, the max stress in the spring steel strip $\sigma_{\max}$ is

$$\sigma_{\max} = \frac{F_{\max} l_1 \left(t_2/2\right)}{I_2} + \frac{F_{\max}}{A_2}, \tag{4.21}$$

where the first term is the component of max stress induced by bending, the second term is the component of max stress induced by axial compression, and

$$F_{\max} = -\frac{E_2 I_2}{l_1 l_2} \left(\theta_2\right)_{\max}. \tag{4.22}$$

It is worth noting $F_{\max}$ is the minimum compressive preload the pair of extension springs must apply to ensure the micrometer always contacts the ball on the bottom plate.

To ensure the strip does not yield,

$$\sigma_{\max} < \sigma_{\text{yield}}, \tag{4.23}$$

where σ_{yield} is the yield stress of spring steel. Given this strip is only being bent a couple times to account for tilt, fatigue is not a concern. However, it is worth noting that in the case where fatigue was a concern,

$$\sigma_{\max} < 0.5\sigma_{\text{ut}} \tag{4.24}$$

where σ_{ut} is the ultimate tensile strength of spring steel and the right side is the endurance limit for steels with ultimate tensile strengths less than 1400 MPa [26].

Tilt Stage Design Principles

Based on the modeling of the test fixture, a list of design principles can be compiled:

Angular Range of Motion

By (4.19), the length of the top plate should be minimized and the height of the strip should be maximized in order to maximize the tilt stage's angular range of motion.

Angular Resolution

By (4.20), the length of the top plate should again be minimized and the resolution of the micrometer should be maximized in order to maximize the tilt stage's angular resolution.

Loading

Due to the cubic dependence of the strip's area moment of inertia on the strip's thickness,(4.13), the strip's thickness should be decreased to decrease the total preload the pair of extension springs must apply and the the max stress in the strip. The strip's thickness cannot decrease too much though as the strip still needs to be stiff axially to support the weight of the Z stage.

Tilt Stage Design

The complete tilt stage is shown in Figure 4-6 while the stage's dimensions and material properties used in its model are given in Table 4.1. The length of the top plate is 79.38 mm (3.125 in), 15.88 mm (0.625 in) longer than the length of the Z stage's base. This allows the driving micrometer to be centered so its displacements do not induce extra moments. In addition, the spring steel strip has a height of 3.07 mm (0.12 in). By (4.19), this provides the tilt stage with an angular travel of 4.57°. This is acceptable as this range of travel is about an order of magnitude greater than

the vertical angular tilt in the initial Dielectric Step Experiment, 0.34°.

The spring steel strip is 0.51 mm (0.020 in) thick tempered 1095 spring steel. According to (4.21), this corresponds to a max stress of 677 MPa at the stage's max tilt. This is adequate as the max stress would be lower than the 800 MPa yield stress and less than half the 1270 MPa ultimate tensile stress for 1095 spring steel [27]. Further, we chose a Mitutoyo 148-132 micrometer to drive the stage for its fine resolution of 10 μm. A 10 μm resolution translates to an angular resolution of 0.0074°, a resolution finer than the angular resolution of the rotation stage, 0.0083°.

The two springs need to apply a combined preload of 20 N. Given the height of the spring steel strip is only 3.07 mm, the two springs need a relaxed length less than 3.07 if they are attached to the top and bottom plate of the tilt stage. Since extension springs with such small relaxed lengths are typically custom and thus cost prohibitive, the extension springs are instead attached to the top plate and the spacer beneath the bottom plate to allow for a much larger relaxed length. Given springs with larger relaxed lengths can be utilized, two generic extension springs from a spring assortment are used.

To manufacture the stage quickly and easily, all the components are designed to be cut by waterjet with minimal additional post processing. In particular, only the holes for the micrometer set screw and for the screws holding the spring steel strip to the top and bottom plate are done afterwards on a mill.

4.3 Alignment Characterization

With the test fixture redesigned, the next step is to confirm that the addition of the rotation and tilt stages account for the horizontal and vertical sources of misalignment, respectively. To verify the rotation stage mitigates the horizontal tilt, both variable spatial wavelength EQS sensors are horizontally swept over a constant air gap target. The measured capacitance is converted to the thickness of the air gap and the remaining amount of tilt is determined from the deviation in this thickness. To verify the tilt stage mitigates the vertical tilt, both variable spatial wavelength

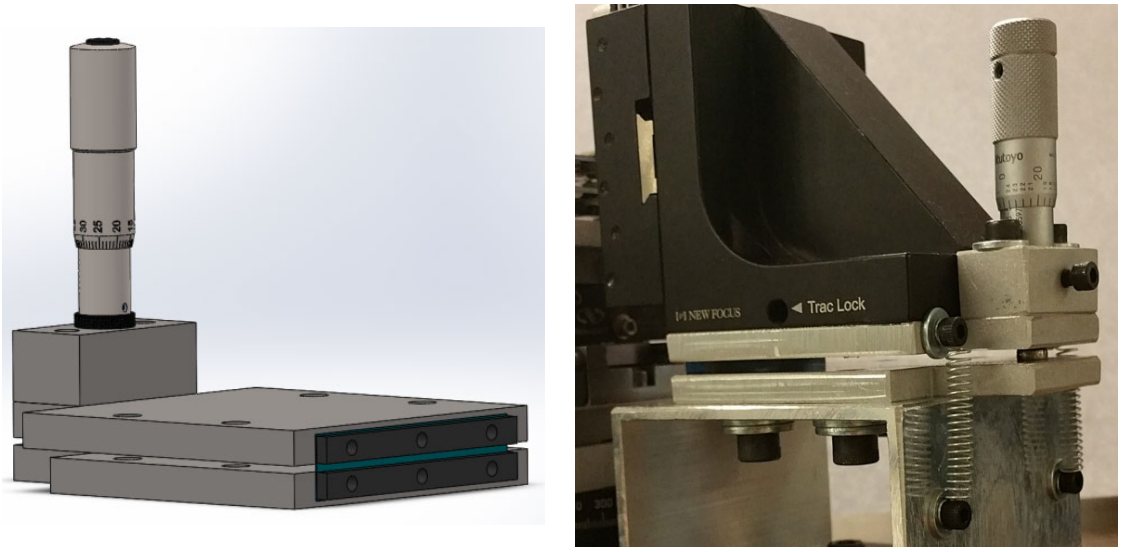

(a) CAD of the flexure tilt stage.

(b) Tilt stage in the redesigned test fixture.

Figure 4-6: Custom flexure tilt stage added in the test fixture redesign to account for vertical misalignment.

EQS sensors are vertically swept over a constant air gap target and the remaining amount of tilt is calculated using the same procedure as for the horizontal sweep.

4.3.1 Noise Characterization

Before conducting these horizontal and vertical sweep alignment experiments, the noise floor of the setup is established. The noise floor is needed as it is the max resolution which the EQS sensors can be aligned relative to the aluminum base. To establish the noise floor, both variable spatial wavelength sensors are connected to the Agilent 4395A impedance analyzer and positioned 100 μm from the base using the first two steps of the alignment procedure in the following section. Both EQS sensors are then stepped 10 μm from the base and the 150 MHz impedance reading of the impedance analyzer is compared before and after the step.

For the long-wavelength sensor, the 10 μm increase in the air gap translates to a 0.1 Ω increase in the 150 MHz impedance reading. The impedance reading jitters by 0.01 Ω before and 0.001 Ω after 8-sample averaging. Thus the long-wavelength EQS sensor reading's had 1 μm of noise without averaging and and 0.1 μm of noise with

Table 4.1: Dimensions & Properties Used in the Tilt Stage Model

Property	Symbol	Value	Units
Top Plate Length	l_1	79.8	mm
Top Plate Width	w_1	63.5	mm
Top Plate Thickness	t_1	6.35	mm
6061-T6 Aluminum Modulus of Elasticity	E_1	69.0	GPa
Spring Steel Strip Height	l_2	3.07	mm
Spring Steel Strip Width	w_2	52.4	mm
Spring Steel Strip Thickness	t_2	0.508	mm
1095 Spring Steel Modulus of Elasticity	E_2	205	GPa
1095 Spring Steel Yield Stress	σ_{yield}	800	MPa
1095 Spring Steel Ultimate Tensile Strength	σ_{ut}	1270	MPa

an 8-sample average.

For the short-wavelength sensor, the 10 μm increase in the air gap correlates to a 0.2 Ω increase in the 150 MHz impedance reading. This change is double the change for the long-wavelength sensor. The impedance readings jitters by 0.04 Ω before and 0.004 Ω after 8-sample averaging. Hence the short-wavelength sensor's reading had 2 μm of noise without averaging and and 0.2 μm of noise with an 8-sample average. Interestingly, this is double the noise the long-wavelength sensor had.

4.3.2 Alignment Procedure

With the noise floor established, the EQS sensors can be used to very finely position themselves relative to the base. We take advantage of this in aligning the sensors with the redesigned test fixture. The steps to align the EQS sensors relative to the base are:

1. Tram the XY stage relative to the base using a dial indicator.

2. Mount and home the long-wavelength sensor.

3. Further tram the XY stage using the long-wavelength sensor.

4. Tram the Z stage using the long-wavelength sensor.

5. Rehome the long-wavelength sensor.

6. Verify the tramming of the XY stage using the long-wavelength sensor.

7. Verify the tramming of the Z stage using the long-wavelength sensor.

8. Mount and home the short-wavelength sensor.

9. Verify the tramming of the XY stage using the short-wavelength sensor.

10. Verify the tramming of the Z stage using the short-wavelength sensor.

For the initial Variable Air Gap Experiment (Section 3.3.1) and initial Dielectric Step Experiment (Section 3.3.2), only steps 1 and 2 are performed as tramming with the EQS sensor itself requires the rotation and tilt stages in order to make fine adjustments.

To tram (rotationally align) the XY stage with a dial indicator, a dial indicator is mounted to the XY stage as shown in Figure 4-7. The XY stage is moved toward the aluminum base until the dial indicator's contact arm deflects a desired amount. Then the XY stage is horizontally swept across the base. The dial's reading at each end of the sweep are compared and the XY stage is rotated so the readings are closer. This horizontal sweep, dial reading comparison and rotation are repeated multiple times until the dial's reading at each end are nearly identical. Rotating the XY stage is done differently before and after the test fixture redesign. For the initial test fixture, the bolts holding down the XY stage are loosened, the XY stage turned by hand, and the bolts are retightened. For the redesigned test fixture, the rotation stage is finely rotated using its micrometer.

The long-wavelength sensor is mounted and homed as shown in Figure 4-8a. For this, the sensor is placed on the XY stage and loosely screwed down, such that the sensor can still slide around due to clearance in its mounting holes. The sensor is then lightly pushed toward the base. This forces the mounting screws to contact the back of their clearance holes. Meanwhile, the XY stage is moved toward the base. Eventually the sensor's electrode array contacts the base and aligns itself with it.

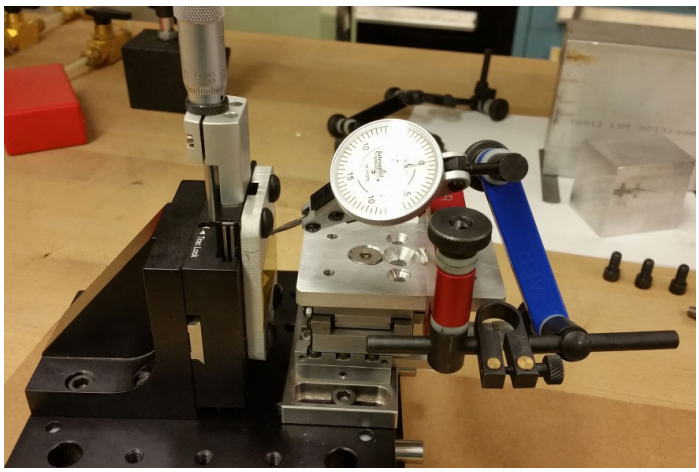

Figure 4-7: Alignment procedure step 1: Tram the XY stage relative to the base using a dial indicator. Note, the initial test fixture is shown here.

While the electrode array is in contact with the base, the XY stage is moved even closer to the base. Since the sensor cannot move from being in contact with the base, this causes the mounting screws to move toward the front of the clearance hole. Once the mounting screws reach the middle of their holes, the mounting screws are tightened down and the force applied to the sensor is removed. Lastly, the Y position of the XY stage is recorded as the long-wavelength sensor's home, the position 0 μm from the base.

Afterwards, the XY stage is further trammed as the dial indicator can only align the ends of the horizontal sweep within 12.7 μm (0.005 in), an order of magnitude greater than the XY stage's resolution. To further tram the XY stage, the long-wavelength sensor's 150 MHz impedance readings at each end of the horizontal sweep are used as depicted in Figure 4-8b. This aligns the ends of the horizontal sweep within 0.01 Ω, (1 μm). The ends can be aligned down to 0.001 Ω (0.1 μm), the averaged noise floor of impedance measurements made with the long-wavelength sensor, but this proves unnecessarily time consuming. This additional tramming is only done after the test fixture's redesign as rotating the XY stage by hand does not provide fine enough adjustments. After this, the Z stage is trammed by comparing the long-wavelength sensor's 150 MHz impedance readings at each end of the vertical sweep. This is depicted in Figure 4-8c.

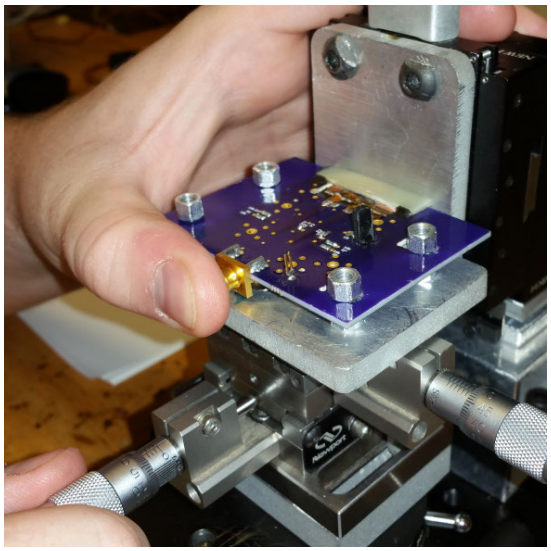

(a) Step 2: Mount and home the long-wavelength sensor.

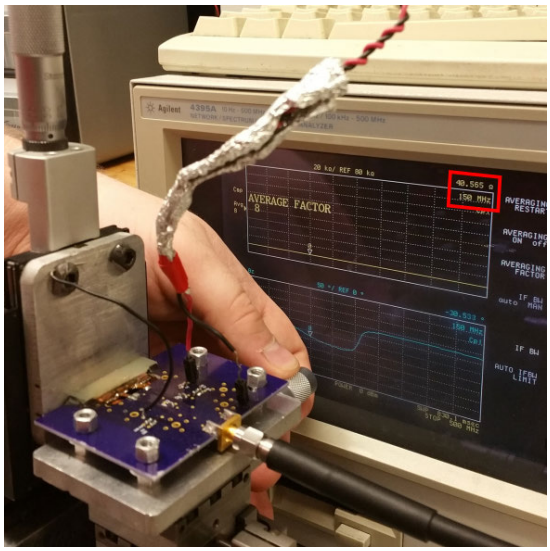

(b) Step 3: Tram the XY stage using the long-wavelength sensor's impedance measurements and the rotation stage.

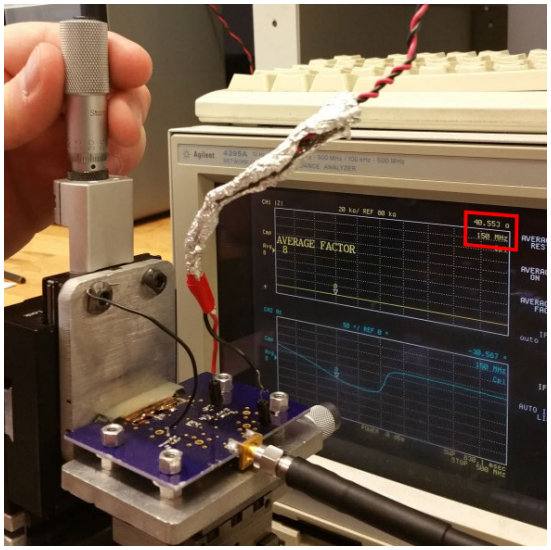

(c) Step 4: Tram the Z stage using the long-wavelength sensor's impedance measurements and the tilt stage.

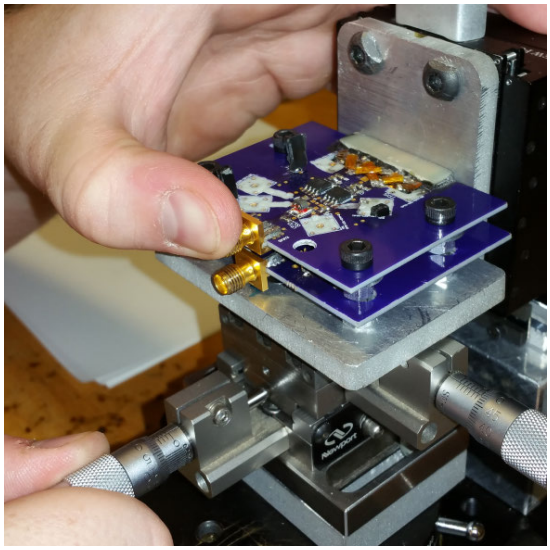

(d) Step 8: Mount and home the short-wavelength EQS sensor.

Figure 4-8: Steps 2, 3, 4 and 8 in the alignment procedure. The red boxes highlight the 150 MHz impedance reading from the impedance analyzer.

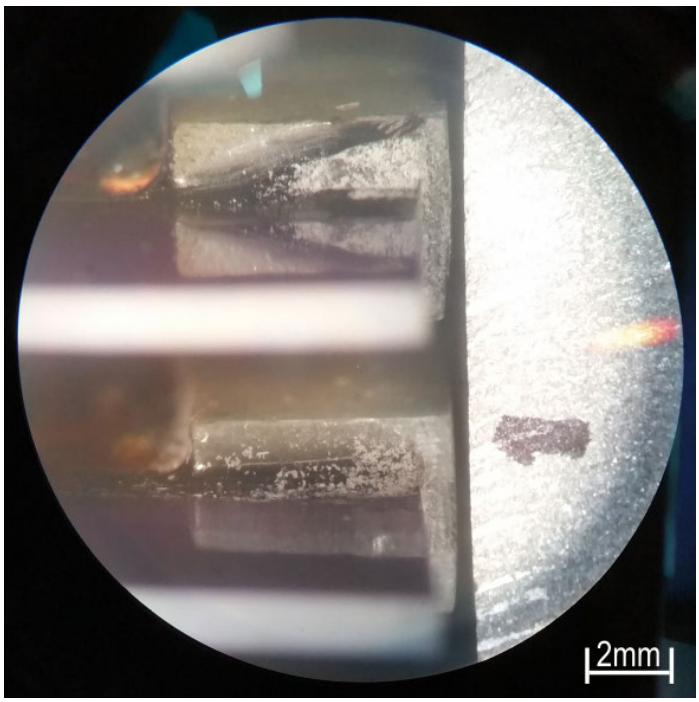

Figure 4-9: Side view of the long-wavelength sensor (bottom) and the short-wavelength sensor (top) in coplanar alignment with the base.

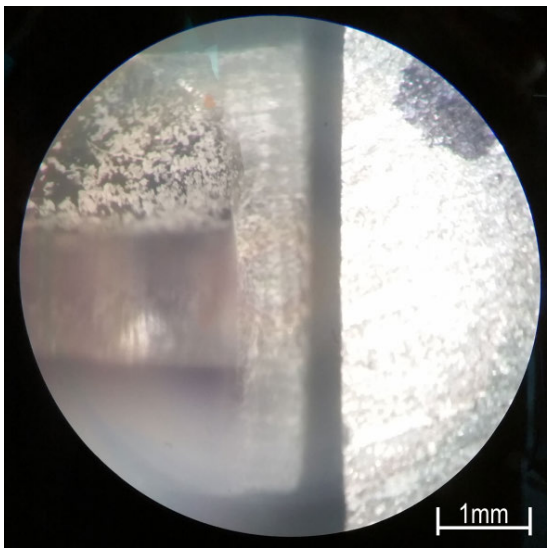

(a) Side view of the long-wavelength sensor in coplanar alignment with the base.

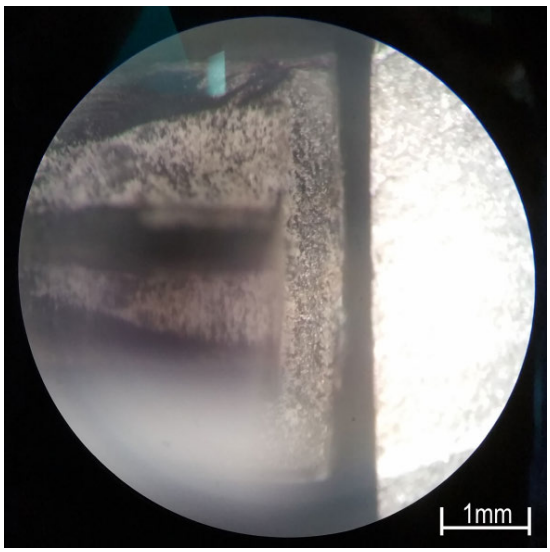

(b) Side view of the short-wavelength sensor in coplanar alignment with the base.

Figure 4-10: Each EQS sensor in coplanar alignment with the base.

With the XY and Z stages both trammed, the long-wavelength EQS sensor is remounted and rehomed. As the rotation stage turns the XY stage and the tilt stage tilts the Z stage during tramming, the orthogonal distance between the long-wavelength sensor and the base slightly changes. Thus the long-wavelength sensor is rehomed. Following this, the long-wavelength sensor is swept horizontally and vertically across the base to verify the XY and Z stages stay trammed.

The short-wavelength sensor is mounted above the long-wavelength sensor and homed using the same procedure as for the long-wavelength senor. This step is displayed in Figure 4-8d. During homing, the XY stage is moved until it reaches the long-wavelength sensor's home position so that both variable spatial wavelength sensors have the same home. Lastly, the short-wavelength sensor is horizontally and vertically swept across the base to verify the tramming of both stages a second time. A side view of the two variable spatial wavelength sensors against the base is provide in Figures 4-9 and 4-10.

4.3.3 Horizontal & Vertical Alignment Experiments

To verify the rotation stage mitigates the horizontal tilt, both the variable spatial wavelength sensors are horizontally swept over a constant air gap target. To verify the tilt stage mitigates the vertical tilt, both sensors are vertically swept over a constant air gap target. The air gap is 100 μm thick as the sensors are positioned 100 μm away from the aluminum base using the alignment procedure outlined in the previous section. For each sweep, the sensors travel 10 mm forward and 10 mm backward across the base.

Even though measurements can only be taken with one sensor at a time, both sensors are swept together so alignment is only done once. The impedance measured by the Agilent 4395A impedance analyzer is recorded from 1 to 500 MHz for every 1 mm of lateral travel forward and backward. These impedances are then passed through ADS by Rakesh Kumar (Section 3.3) to produce the measured capacitance profiles for each alignment experiment. Figures 4-11a and 4-13a show the measured capacitance profiles for the horizontal alignment experiments with long-and short-wavelength sen-

sors respectively. Figures 4-15a and 4-17a show the measured capacitance profiles for the vertical alignment experiments with long-and short-wavelength sensors respectively.

We convert these measured capacitances to air gap thickness using the same approach used in the initial Dielectric Step Experiment (Section 3.3.2). For a 100 μm air gap, the capacitance predicted by the single dielectric parallel plate + fringe field model, (2.5), is compared to the capacitance predicted by just the single dielectric parallel plate model, (2.1):

$$C_{\text{Parallel-Single}} + C_{\text{Fringe-Single}} = \alpha C_{\text{Parallel-Single}}, \tag{4.25}$$

where α is the factor relating the capacitance predicted by the two models.

Then the measured capacitance is compared against the total predicted capacitance:

$$C_{\text{Measured}} = \beta(C_{\text{Parallel-Single}} + C_{\text{Fringe-Single}}), \tag{4.26}$$

where β is the factor relating the measured and predicted capacitances.

Lastly, these two comparisons are used to approximate the air gap thickness:

$$d_{\text{air}} \approx \alpha\beta \left(\frac{\epsilon_{\text{air}} A}{C_{\text{Measured}}} \right). \tag{4.27}$$

Using (4.27), a profile for the air gap thickness in each alignment experiment is calculated from each experiment's capacitance profile. The relating factors, α and β, used in each approximation are listed in Table 4.2. α and β are the same for the long-wavelength senor alignment experiments as the experiments are taken in series. β is different for the short-wavelength senor alignment experiments as they are not taken in series. The short-wavelength senor horizontal alignment experiment had to be retaken at a later time with a different calibration for the impedance analyzer as the cable between the impedance analyzer and the senor came loose in the initial experiment, corrupting the data.

The air gap thickness profiles for the long-and short-wavelength horizontal align-

Table 4.2: Relating Factors, α & β, Used to the Approximate Air Gap Thickness

Sweep Direction	EQS Senor	α	β
Horizontal	Long-Wavelength	1.50	1.78
Horizontal	Short-Wavelength	1.49	2.92
Vertical	Long-Wavelength	1.50	1.78
Vertical	Short-Wavelength	1.49	1.07

ment experiments are shown in Figures 4-11b and 4-13b, respectively. The air gap thickness profiles for the long-and short-wavelength vertical alignment experiments are shown in Figures 4-15b and 4-17b, respectively. To convert the air gap thickness to deviation in air gap thickness, 100 μm is subtracted from each point on the profiles. Figures 4-12 and 4-14 show how well the variable spatial wavelength senors are horizontally aligned while Figures 4-16 and 4-18 show how well they are vertically aligned.

As the long-wavelength senor sweeps horizontally and vertically over the aluminum base, it moves a maximum of 1.99 μm and 2.26 μm orthogonal to the base, respectively. As the short-wavelength EQS sensor sweeps vertically over the base, it moves a maximum of 4.97 μm orthogonal to the base. Lastly, as the short-wavelength EQS sensor sweeps horizontally over the base, it moves a maximum of 2.61 μm orthogonal to the base on the forward pass, but a maximum of 8.47 μm orthogonal to the base on the backward pass. This difference in the amount moved on the forward and backward passes can be attributed to the setup being bumped as measured capacitance suddenly jumps a constant amount halfway through the backward pass.

In the initial Dielectric Step Experiment (Section 3.3.2), the base is tilted 0.34° relative to the long-wavelength sensor, causing the sensor to move 5.309 μm orthogonal to the base per millimeter of travel. If the sensor swept a distance of 10 mm, like in these alignment experiments, the EQS sensor would have moved 53.09 μm orthogonal to the base. Thus adding the rotation and tilt stages reduces the amount of tilt in the test fixture by over an order of magnitude. The tilt can be further reduced as the deviations measured in both alignment experiments with the long-wavelength sensor and the vertical alignment experiment with the short-wavelength sensor are

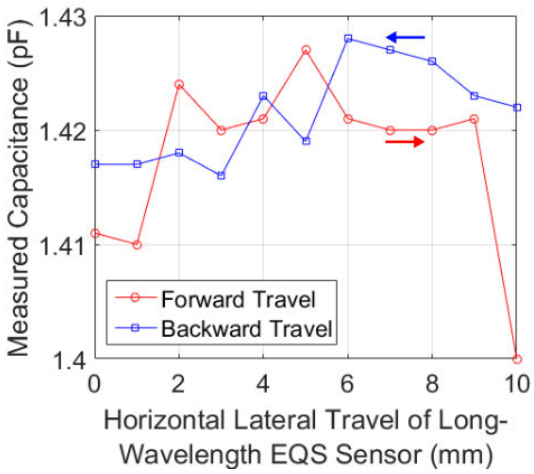

(a) Measured capacitance as the long-wavelength sensor is swept back and forth horizontally.

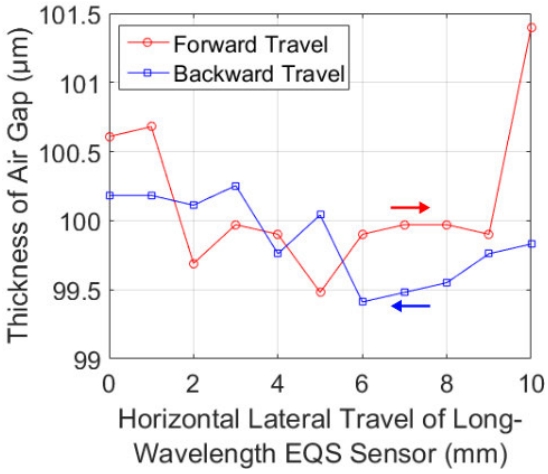

(b) Calculated air gap thickness from the measured capacitance.

Figure 4-11: Horizontal alignment experiment with the long-wavelength EQS sensor. The arrows indicate the direction of travel.

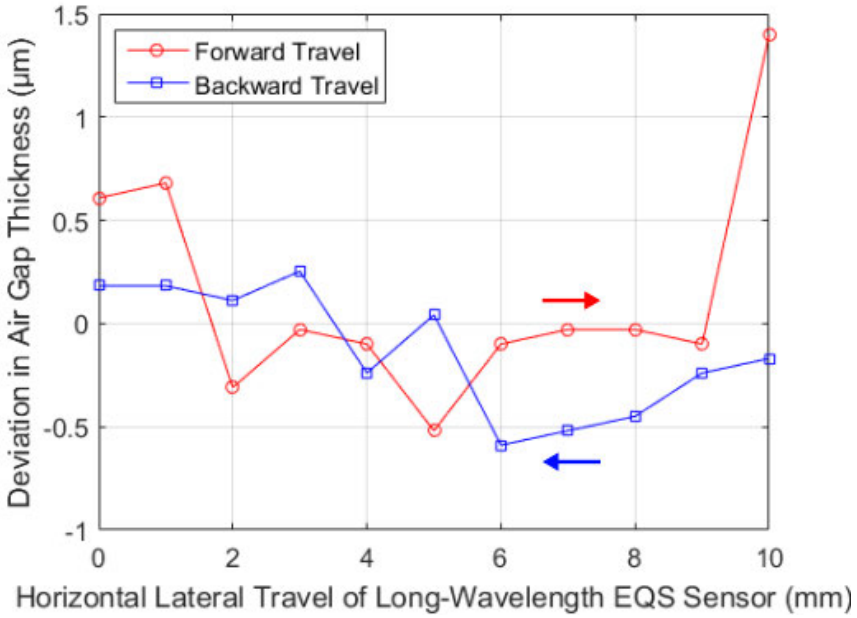

Figure 4-12: Deviation in air gap thickness during the horizontal alignment experiment with the long-wavelength EQS sensor. The arrows indicate the direction of travel.

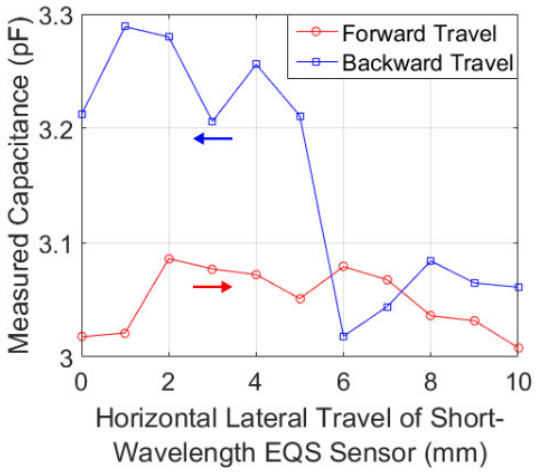

(a) Measured capacitance as the short-wavelength sensor is swept back and forth horizontally.

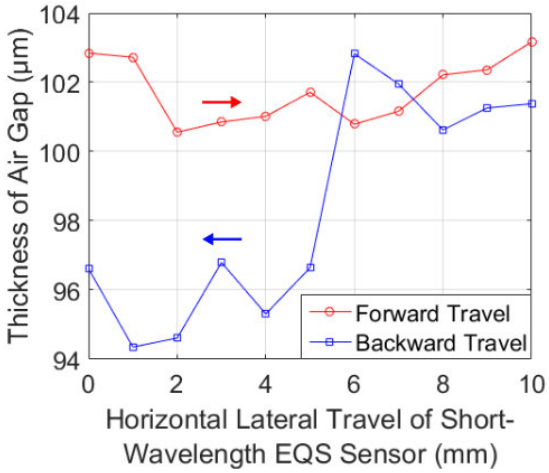

(b) Calculated air gap thickness from the measured capacitance.

Figure 4-13: Horizontal alignment experiment with the short-wavelength EQS sensor. The arrows indicate the direction of travel. The jump in (a) measured capacitance and (b) air gap thickness on the backward pass can be attributed to the setup being bumped.

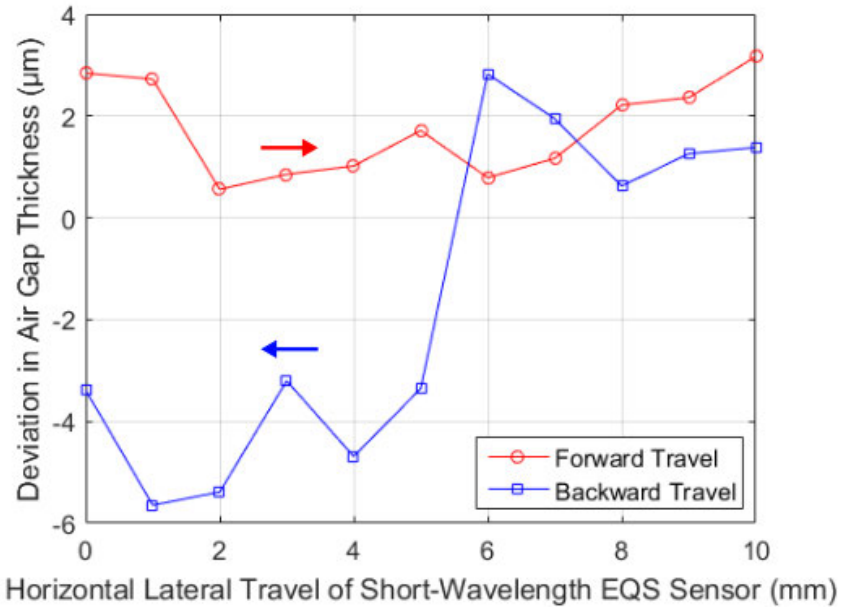

Figure 4-14: Deviation in air gap thickness during horizontal alignment experiment with the short-wavelength EQS sensor. The arrows indicate the direction of travel. The jump in deviation in air gap thickness can be attributed to the setup being bumped.

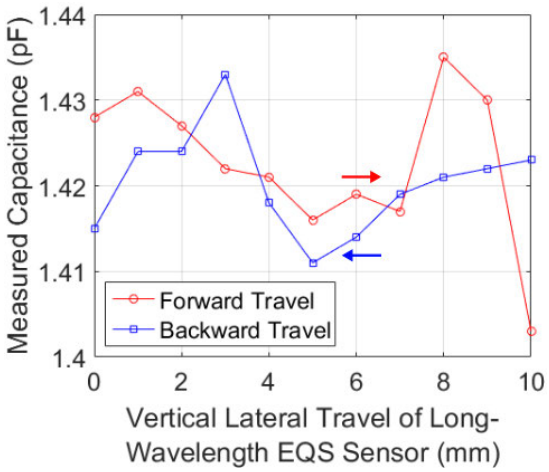

(a) Measured capacitance as the long-wavelength sensor is swept back and forth vertically.

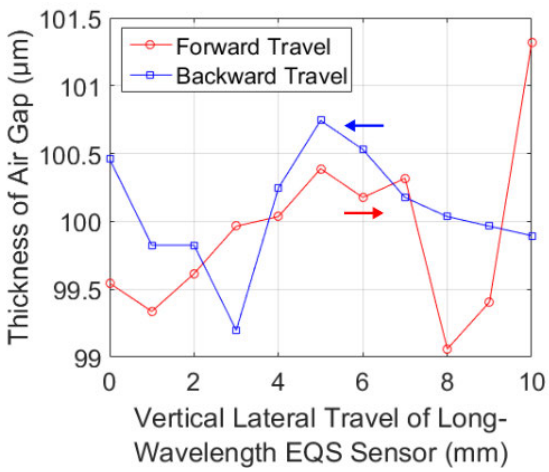

(b) Calculated air gap thickness from the measured capacitance.

Figure 4-15: Vertical alignment experiment with the long-wavelength EQS sensor. The arrows indicate the direction of travel.

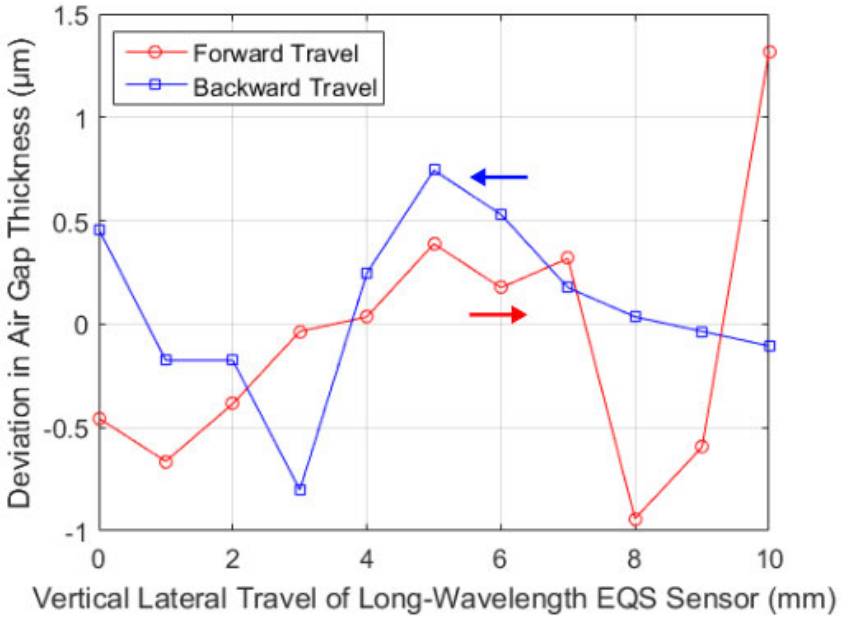

Figure 4-16: Deviation in air gap thickness during the vertical alignment experiment with the long-wavelength EQS sensor. The arrows indicate the direction of travel.

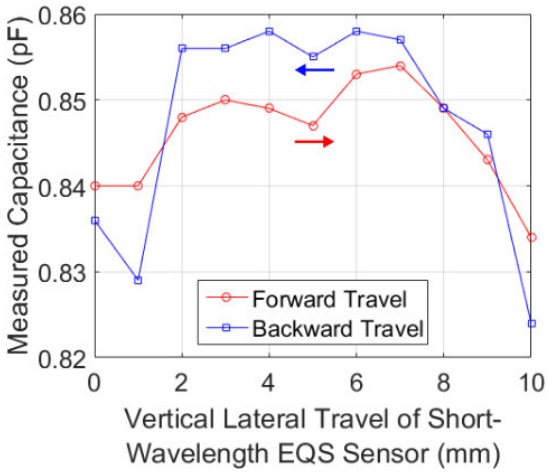

(a) Measured capacitance as the short-wavelength sensor is swept back and forth vertically.

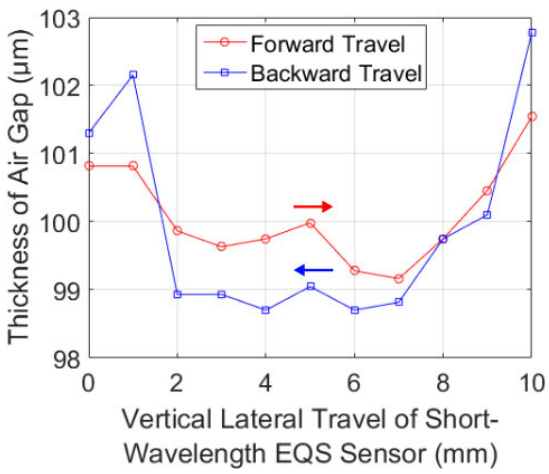

(b) Calculated air gap thickness from the measured capacitance.

Figure 4-17: Vertical alignment experiment with the short-wavelength EQS sensor. The arrows indicate the direction of travel.

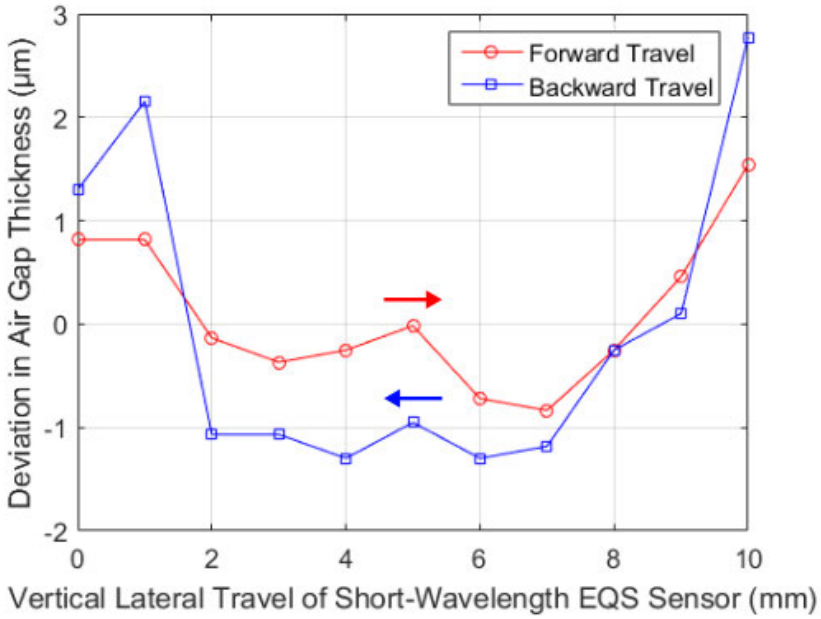

Figure 4-18: Deviation in air gap thickness during the vertical alignment experiment with the short-wavelength EQS sensor. The arrows indicate the direction of travel.

about double the unaveraged noise floor for each experiment. However, this amount of alignment is adequate as reducing the amount of deviation to the levels of the averaged noise floors proves to be unnecessarily time consuming.

4.4 Chapter Summary

This chapter presented the redesign and testing of the test fixture to account for the tilt found in the initial Variable Air Gap Experiment (Section 3.3.1) and the initial Dielectric Step Experiment (Section 3.3.2). First additional design requirements for the redesigned test fixture were presented:

1. The test fixture should minimize the amount of horizontal misalignment between the sensor and the base.

2. The test fixture should minimize the amount of vertical misalignment between the sensor and the base.

To account for the horizontal misalignment, a Melles Griot Micrometer-Driven Rotation Stage (Model: 98 mm Dia.) is added underneath the XY stage. To account for the vertical misalignment, a custom micrometer-driven flexure stage is designed, fabricated, and added underneath the Z stage.

Following the redesign of the test fixture, the noise floors of measurements made with both variable spatial wavelength sensors were characterized. Measurements made with the long-wavelength sensor have a noise floor of 1.0 μm without averaging and a noise floor of 0.1 μm with an 8-sample average. Measurements made with the short-wavelength EQS sensor have a noise floor of 2.0 μm without averaging and a noise floor of 0.2 μm with an 8-sample average.

With the noise floors characterized, both variable spatial wavelength sensors were placed 100 μm orthogonal to the aluminum base. At this distance, both sensors were swept horizontally and vertically across the base to measure the deviation in the air gap thickness due to the remaining tilt in the redesigned test fixture. The thickness of the air gap deviates by 1.99 μm and 2.26 μm as the long-wavelength sensor sweeps

horizontally and vertically. The thickness of the air gap deviates by 8.47 μm and 4.97 μm as the short-wavelength sensor sweeps horizontally and vertically. These deviation in the air gap thickness are over an order of magnitude less than deviation in the air gap thickness in the initial Dielectric Step Experiment.

Chapter 5

Scanning Experiments

This chapter presents the results for a second set of Variable Air Gap Experiments and Dielectric Step Experiments. These experimental results are accomplished jointly with Rakesh Kumar. The experimental setup with redesigned test fixture and the impedance analyzer for these experiments is provided in Figure 5-1.

In the initial Variable Air Gap Experiment and initial Dielectric Step Experiment with the long-wavelength sensor, some disagreement exists between the measured and predicted capacitance profiles. Part of this disagreement is because tilt in the initial test fixture introduced undesired changes in capacitance. Given the test fixture was redesigned to minimize this tilt, it is worth repeating these experiments to determine the level of disagreement that still exists between the measured and predicted capacitance profiles. Further, the initial experiments were only conducted using the long-wavelength sensor so it is also worth doing the experiments again as they still need to be done with the short-wavelength sensor. Finally, Rakesh Kumar improved the optimization used by ADS to convert the measured impedances to measured capacitances [5]. Thus it is worth repeating the experiments as another source of disagreement between the measured and predicted capacitance profiles was minimized.

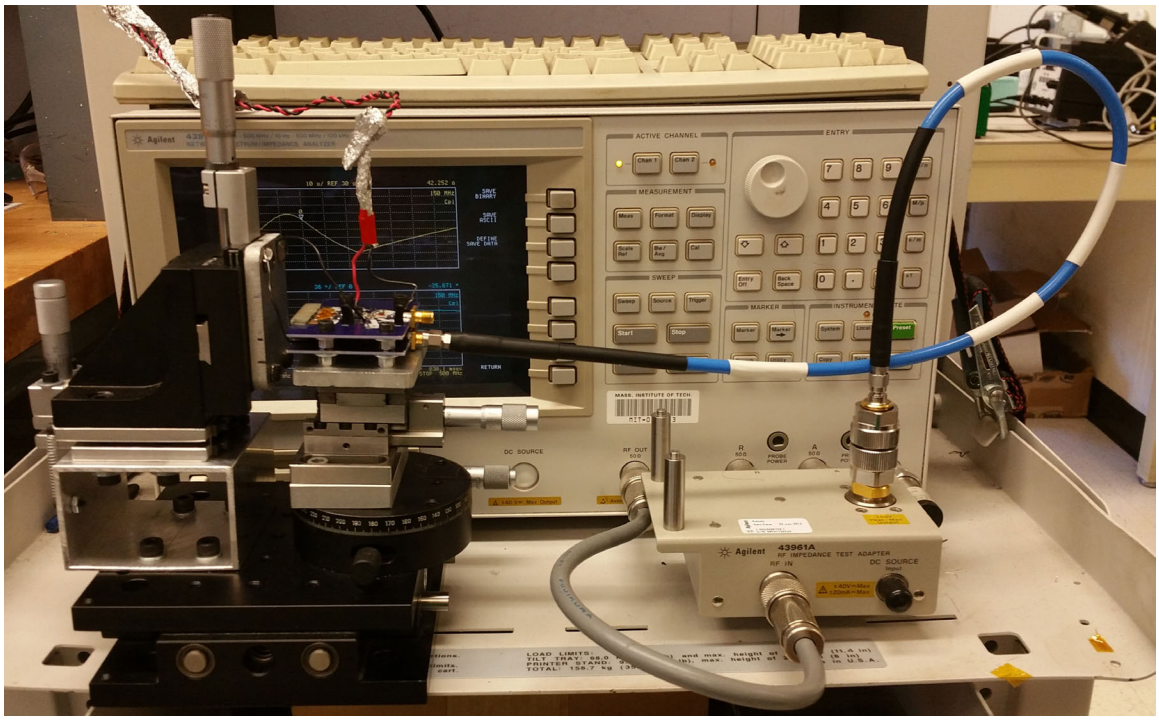

Figure 5-1: Experimental setup with both different spatial wavelength EQS sensors mounted on the redesigned test fixture. The long-wavelength EQS sensor is shown connected to the impedance analyzer.

5.1 Variable Air Gap Experiment

Just like in initial Variable Air Gap Experiment (Section 3.3.1), both variable spatial wavelength sensors are placed 20 μm from the aluminum base. However, the full alignment procedure given in Section 4.3.2 is used to position them. Then both EQS sensors are stepped back in increments of 10 μm until the air gap is 100 μm thick and then in increments of 50 μm until the air gap is 700 μm thick. This is done twice as the Agilent 4395A impedance analyzer can only connect to one sensor at a time.

At each step, the measured impedance is averaged eight times and recorded from 1 to 500 MHz. The measured impedance is then passed through ADS by Rakesh Kumar (Section 3.3) to determine the capacitance at each step. The resulting capacitance profiles measured by the long-and short-wavelength sensors due to an increasing air gap are shown in Figures 5-2 and 5-3 respectively. Both profiles are shown with their respective capacitance profiles predicted by the parallel plate + fringe field model for

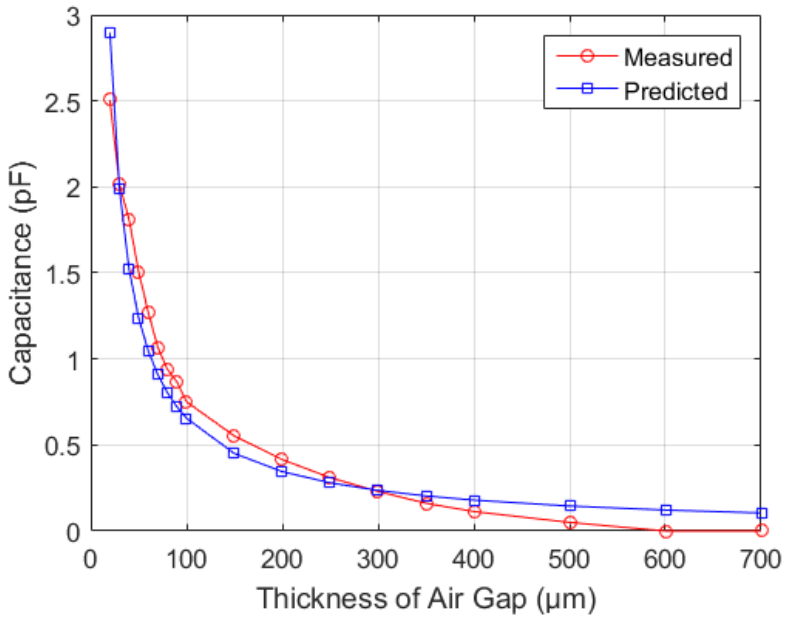

Figure 5-2: Measured vs. predicted capacitance of the long-wavelength EQS sensor due to a variable air gap using the redesigned test fixture and updated ADS optimization. The predicted capacitance is from the single dielectric parallel plate + fringe field model, (2.5).

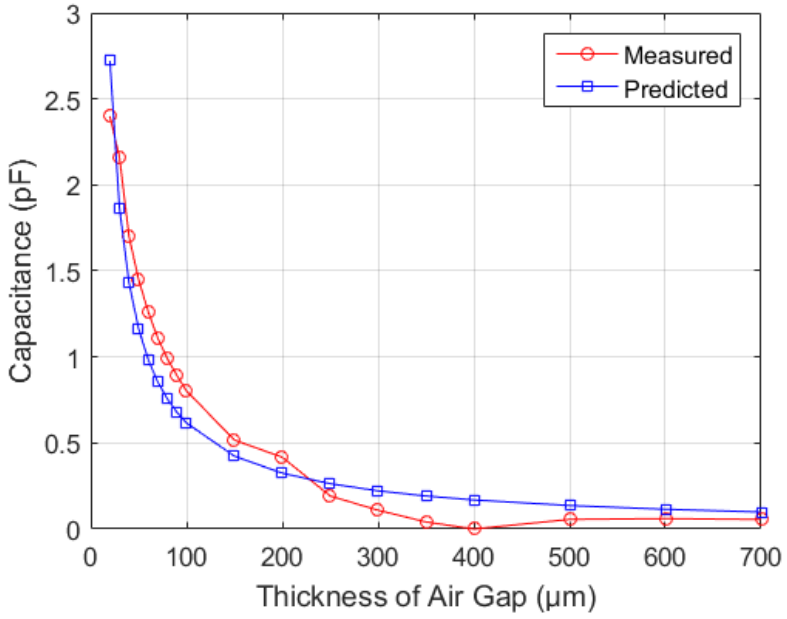

Figure 5-3: Measured vs. predicted capacitance of the short-wavelength EQS sensor due to a variable air gap using the redesigned test fixture and updated ADS optimization. The predicted capacitance is from the single dielectric parallel plate + fringe field model, (2.5).

a single dielectric, (2.5).

Again, the measured capacitance profiles follow the predicted capacitance profiles, inversely decaying as the air gap increases. On top of that, less disagreement exists between the measured and predicted capacitance profiles than in the initial experiment. First, the measured capacitance is no longer constantly larger than the predicted capacitance. This is likely due to the improvements Rakesh Kumar made to the ADS optimization for converting measured impedance to measured capacitance. Second, the measured capacitances no longer tapers off as the sensors approach the base. In the initial experiment, the measured capacitance tapers off around 20 μm. This occurred because tilt in the test fixture caused the long-wavelength sensor to prematurely contact the base, which resulted in a constant air gap and in turn, a constant measured capacitance. Thus test fixture redesign and the more thorough alignment procedure successfully minimize the affect of tilt between the sensors and the base.

5.2 Dielectric Step Experiment

The new Dielectric Step Experiments are performed similarly to the initial Dielectric Step Experiment (Section 3.3.2). A 65 μm thick strip of Kapton tape is placed horizontally across the base as shown in Figure 3-5. The tape is placed during the new alignment procedure while the sensors are at their home position to use the top of the short-wavelength sensor as a guide. Afterwards, both variable spatial wavelength sensors are positioned 100 μm away from the aluminum base (35 μm from the Kapton). Both sensor sweep vertically over the aluminum base, moving from completely off to completely on the Kapton strip. Again, this is done twice, once for each sensor.

As with all the other experiments, the measured impedance is averaged eight times and recorded from 1 to 500 MHz by the Agilent 4395A impedance analyzer. Rakesh Kumar passed this measured impedance data through ADS (Section 3.3) to produce measured capacitance profiles. The resulting capacitance profiles measured by the long-and short-wavelength sensors as they step onto the Kapton strip are shown

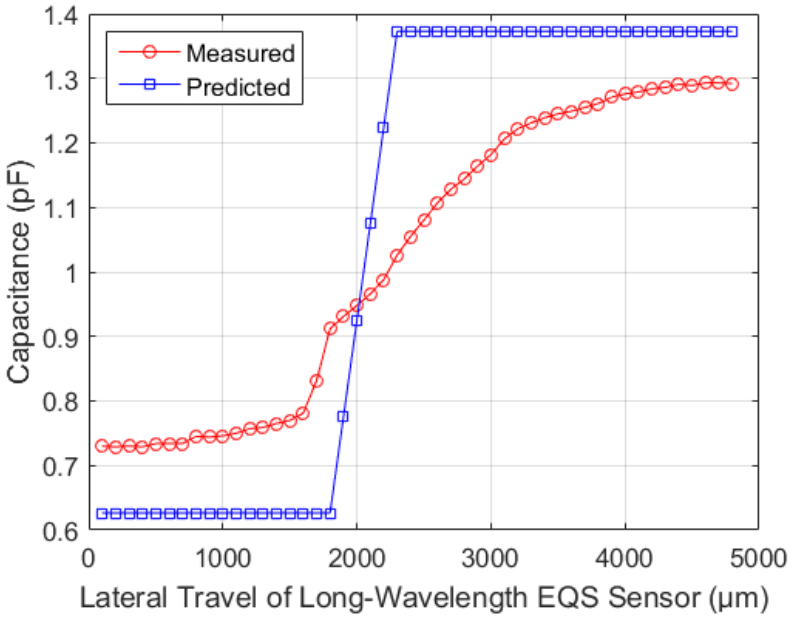

Figure 5-4: Measured vs. predicted capacitance of the long-wavelength EQS sensor while sweeping over a dielectric step using the redesigned test fixture and updated ADS optimization. The predicted capacitance is from the double dielectric parallel plate + fringe field model, (2.6).

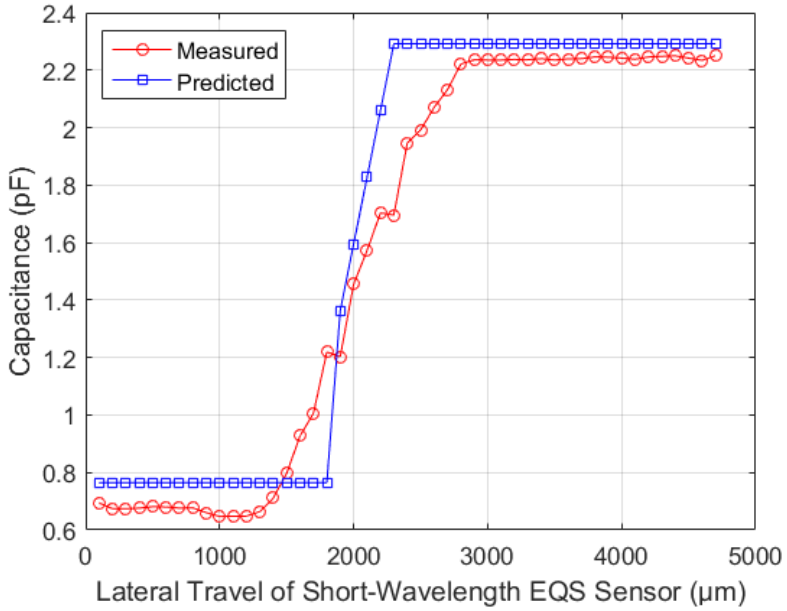

Figure 5-5: Measured vs. predicted capacitance of the short-wavelength EQS sensor while sweeping over a dielectric step using the redesigned test fixture and updated ADS optimization. The predicted capacitance is from the double dielectric parallel plate + fringe field model, (2.6).

in Figures 5-4 and 5-5, respectively. Both profiles are shown with their respective capacitance predicted by the double dielectric parallel plate + fringe field model, (2.6).

Again, the measured capacitance profiles follow the predicted capacitance profiles, increasing as the sensors pass onto the Kapton strip. Relative to the initial experiment, there is less disagreement between the short-wavelength sensor's measured and predicted capacitance profiles, but more disagreement between the long-wavelength sensor's measured and predicted capacitance profiles. In regards to the short-wavelength sensor's profiles, the measured capacitance profile is flatter before and after the Kapton step than the measured capacitance profile was in the initial experiment. This indicates that the redesign of the test fixture and the improved alignment procedure successfully reduces tilt in the experiment. Further, the measured capacitance profile steps faster than the measured capacitance profile did in the initial experiment, but unfortunately not as fast as predicted. This indicates using the edge of the short-wavelength sensor as a guide for placing the Kapton strip reduces the angle between the edge of the Kapton strip and the edge of the short-wavelength sensor, but does not eliminate it.

As for the long-wavelength sensor's measured capacitance profile, it is flatter before Kapton step than the measured capacitance profile was in the initial experiment. This further validates that the redesign of the test fixture and the improved alignment procedure successfully reduce the tilt in the experiment. However, the measured capacitance profile steps slower than the measured capacitance profile did in the initial experiment. This can be attributed to a larger angle existing between the edge of the Kapton strip and the edge of the long-wavelength sensor than in the initial experiment. This angle is larger for the long-wavelength sensor than for the short-wavelength sensor as the Kapton strip is aligned horizontally relative to the edge of the short-wavelength sensor only. We did not realign the Kapton strip relative to the edge of the long-wavelength sensor when testing it as we assumed the two sensors were mostly parallel since the standoffs separating them had very tight tolerances. However this assumption was flawed as the standoffs' tolerances may not have been tight

enough and the sensor's PCBs may have been compressed slightly during mounting, tilting the two sensors relative to one another.

To eliminate this angle between the two variable spatial wavelength sensors, there are a couple of different options. First, another tilt stage can be added between the two sensors. However this is extremely undesirable as the two sensors would no longer be side-by-side. The other option is to integrate the electrode arrays of both sensors into a single electrode array. Thus their alignment can be controlled during manufacturing. This is not done either, but is useful to consider in the future designs of EQS sensors.

5.3 Chapter Summary

This chapter presented the results from a second set of Variable Air Gap Experiments and Dielectric Step Experiments. These experimental results are accomplished jointly with Rakesh Kumar. These results were compared to the results of the initial Variable Air Gap Experiment and initial Dielectric Step Experiment. Less disagreement exists between the measured and predicted capacitance profiles in the new Variable Air Gap Experiments than in the initial experiment. The measured capacitance profiles are no longer constantly larger than their predicted capacitance profiles. This is likely due to the improvements Rakesh Kumar made to the ADS optimization for converting measured impedance to measured capacitance. In addition, the measured capacitance profiles no longer taper off near 20 μm. This is because the sensors no longer contact the aluminum base prematurely as they approached it. Thus test fixture redesign and the more thorough alignment procedure successfully minimize the affect of horizontal tilt between the sensors and the base.

As for the new Dielectric Step Experiments, both measured capacitance profiles increase in capacitance as the sensors moves from completely off to completely on the Kapton strip. Both measured capacitance profiles are very flat before and after the Kapton step, further validating that the test fixture redesign and the more thorough alignment procedure successfully minimize the affect of vertical tilt between the sen-

sors and the base. However, only the short-wavelength sensor's measured capacitance profile steps faster than the initial experiment's measured capacitance profile. This is because the Kapton tape is placed horizontally relative to the edge of the short-wavelength sensor and an angle exists between these two variable spatial wavelength sensors. This angle can be accounted for by fabricating all the electrode arrays as part of one larger electrode array in the future.

Chapter 6

Concept for High-Bandwidth Imaging System

This chapter presents concepts for a high-bandwidth measurement system and a high-bandwidth scanning system that could be used with the high-frequency EQS sensors to potentially image at high speeds. Further, integrated circuit (IC) implementation of the high-frequency sensors is considered to improve performance.

First, approaches for impedance measurements made using radio frequency excitations are discussed. From this discussion, design parameters are determined for the high-bandwidth measurement system. A high-bandwidth measurement system which satisfies those design requirements is presented. However, the hardware for this measurement system does not natively make high frequency impedance measurements and programming this hardware to do so, proves to be a major roadblock. Thus this measurement system exists only as a concept. Following this, the design requirements are provided for the high-speed scanning system. A high-speed scanning system which satisfies these design requirements is presented, but is not used since the high-bandwidth measurement electronics are not able to be implemented. Finally the potential resolution and the time it would take this concept EQS imaging system to scan the example IC photomask in Section 1.3 is considered. This potential resolution and scan time can be further improved through IC implementation of the high-frequency EQS sensors.

6.1 High-Bandwidth Measurement System Concept

6.1.1 S Parameters Measurement

As electrical power travels through a wire, it propagates as an electromagnetic wave with a wavelength λ proportional to its propagation speed v_{p}, and oscillation frequency in [Hz], f:

$$\lambda = \frac{v_{\mathrm{p}}}{f}. \tag{6.1}$$

At low frequencies, this wavelength is much larger than length of the wire so the voltage and current along the wire are essentially independent of their position. However, at high frequencies, this wavelength is comparable to or smaller than the length of the wire so the voltage and current along the wire are now dependent on their positions.

In the past, EQS sensors used relatively low excitation frequencies. Therefore the capacitance between these EQS sensors and a target could be determined by driving one set of electrodes at a given voltage or current and conventionally measuring the corresponding induced current or voltage on the other set of electrodes. Assuming the two electrode sets behave purely capacitively (no conductivity), this capacitance is given by:

$$Z_{11} = \frac{V}{I} = \frac{1}{j\omega C}. \tag{6.2}$$

Here, Z_{11} and C are the impedance and capacitance across the EQS sensor's electrode sets, respectively. Voltage V is the driving or induced voltage that can be measured with a voltmeter, current I is the corresponding induced or driving current that can be measured with a current meter, and ω is the frequency of the driving signal in [rad/sec].

To use EQS sensors for high speed imaging, the sensors need to operate with high excitation frequencies. As a result, the driving or induced voltages and currents in the sensor are now dependent on their positions. This makes measuring the voltages and currents difficult with volt and current meters. Further, this makes impedance a poor parameter to characterize the EQS sensor with since it is determined from values that are now position dependent, and more critically dependent on stray elements.

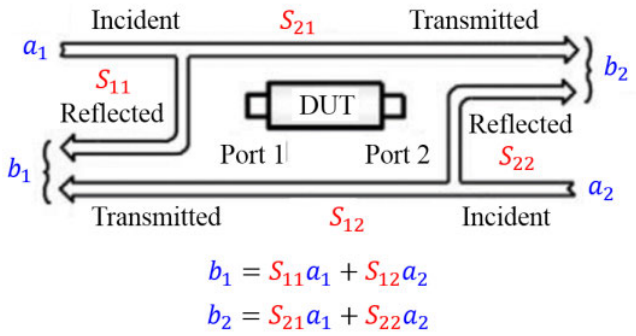

Figure 6-1: S-parameters for a two port circuit element. Taken from [28].

At high frequencies, circuit elements are typically characterized with scattering parameters (S-parameters) as S-parameters are determined from values that are not position dependent. Power is put into a circuit element via electromagnetic waves known as incident waves. Some of these electromagnetic waves will pass through the circuit element onto the next circuit element while some of these electromagnetic waves will be reflected back to the source. The electromagnetic waves that pass through are known as transmitted waves while the electromagnetic waves that return to the source are known as reflected waves. The ratios between these incident, transmitted, and reflected waves can be used to characterize the circuit element. These ratios are the circuit element's S-parameters.

Circuit elements with two ports require four S-parameters. Figures 6-1 and 6-2, taken from Agilent's white paper on Network Analyzer basics [28], show the four S-parameters and their definitions. However, EQS sensors are single port circuit elements from the view of the drive/sense electronics. Such single-port circuit elements are charactered by one S-parameter, S_{11}:

$$S_{11} = \frac{\text{Reflected Signal}}{\text{Incident Signal}}. \tag{6.3}$$

Since S_{11} completely characterizes the EQS sensor, it should be able to relate back to the capacitance between the sensor and the target. S_{11} is related to Z_{11} [28, 29, 30] by

$$Z_{11} = 50\Omega\left(\frac{1+S_{11}}{1-S_{11}}\right) \tag{6.4}$$

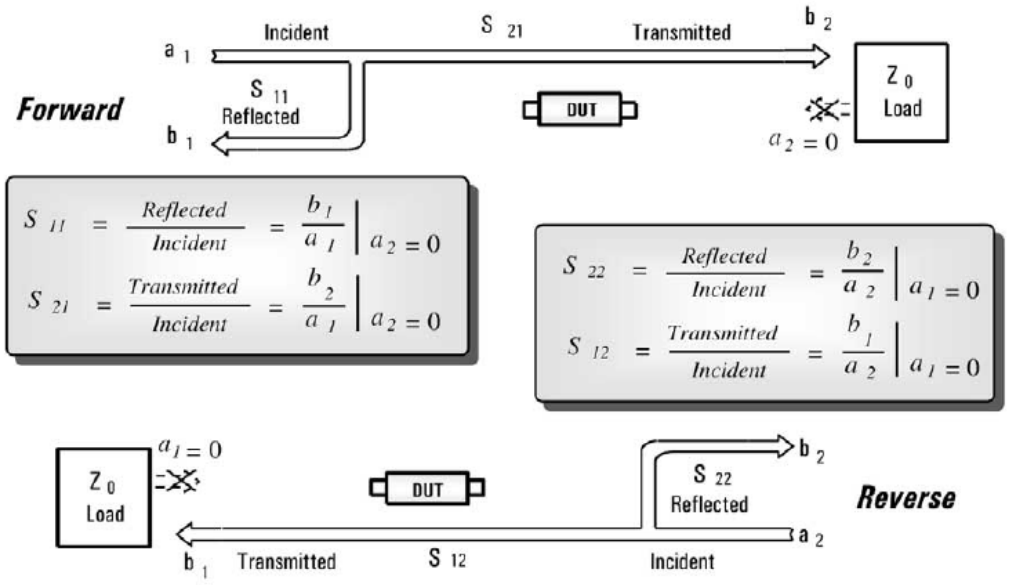

Figure 6-2: Finding the S-parameters for a two port circuit element taken from [28].

and the capacitance can then be found from (6.2). Thus to image with EQS sensors at high speeds, the incident signals into and the reflected signals from the EQS sensors need to be measured. For more information on S-parameters and their measurements, [28, 29, 30] are suggested readings.

6.1.2 Design Requirements for High-Bandwidth Measurements

Based on making high-speed measurements with S-parameters, a list of design requirements is compiled. This list is further expanded based on the proposed operating parameters needed for EQS sensors to scan an example IC photomask at the speeds in Table 1.1. The complete list of design requirements are:

Dual Measurements

The measurement system should be able to measure both the incident signal and reflected signal from the EQS sensor.

High Drive Frequency

The measurement system should be able to output a drive signal with a fre-

quency of at least 100 MHz, ideally at least 1 GHz, to excite the sensor.

High Data Read Rate

The measurement system will need a high read rate to fully capture the incident and reflected signals.

Frequency Sweep

To covert the measured S-parameters to measured capacitance, the S-parameters are first converted to impedance via (6.4) and then from impedance to capacitance by Agilent's Advanced Design System (ADS) as described in Section 3.3. Since ADS requires the measured impedance at multiple frequencies to calculate the measured capacitance, the measurement system should be able to measure the S-parameters at multiple frequencies.

Synchronization

The measurement system needs to be able to be coordinated with the scanning system in order to image.

With these design requirements compiled, a concept for the measurement system is developed.

6.1.3 Measurement Hardware

The measurement system is designed with the help of Matthew D'Asaro. This system is only a concept though as it could not make S-parameter measurements without significant reprogramming of its hardware. It consists of five components:

1. a National Instruments Vector Signal Transceiver, VST, (Model: PXIe-5645R),
2. a directional coupler (Model: ZHDC-16-63+) from Mini-Circuits,
3. a phase stable cable (Model: KBL-2FT-PHS+) from Mini-Circuits,
4. two hand-flex cables (Models: 141-3SM+ and 141-4SMRSM+) from Mini-Circuits.

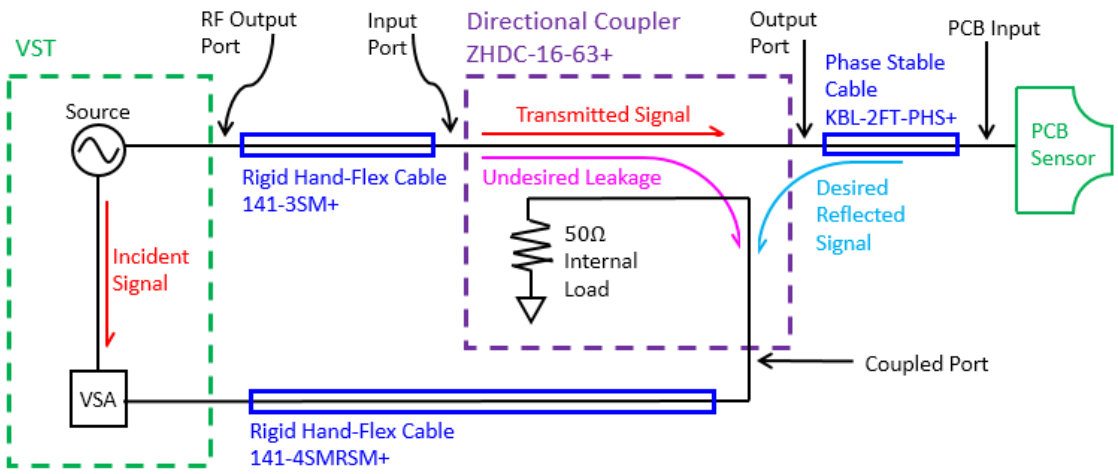

Figure 6-3: Schematic of signals and connections between the VST and the EQS sensor in order to make S-parameter measurements. Unfortunately, the VST is ultimately incapable of operating in this configuration.

Figure 6-3 shows a possible configuration of these components to potentially measure the S-parameter of an EQS senor. The VST connects to a directional coupler by two hand-flex cables and the directional couple connects to the EQS sensor by a phase stable cable. To measure the S-parameter, the VST generates an incident signal and passes it through the direction couple to the EQS sensor. Before the incident signal leaves the VST, it is recorded as it is needed later to calculate the S-parameter. Part of the incident signal is reflected back by the EQS sensor. This partial, reflected signal is siphoned off by the directional couple as it returns to the VST [31]. This siphoned, reflected signal is measured by the VST and compared to the recorded incident wave to determine the sensor's S-parameter.

We chose the VST as it appears to meet several of these design requirements simultaneously. The VST is shown in Figure 6-4. It is able to generate and read signals with frequencies from 65 MHz to 6 GHz, potentially enabling the EQS sensors to be driven and read at the frequencies necessary for high-bandwidth imaging. Further, the VST is capable of outputting signals with swept frequencies, allowing the sensor's S-parameters to be measured at multiple frequencies. Lastly, the VST can be programmed in LabVIEW Real Time, allowing measurement taking to be synchronized with the motion of the scanning system.

Figure 6-4: NI PXIe-5645R Vector Signal Transceiver (VST). Taken from [32].

However, the VST only has a single input port to read signals. As a result, it can only be used to measure the sensor's incident or reflected signal. To circumvent this issue, we decided that the input port would read the reflected signal and the incident signal would be recorded and stored in memory as it is output. Unfortunately, losses in the incident signal will not be taken into consideration in this configuration, but we deemed this acceptable. Alternatively, the input port can instead alternate in reading the incident and reflected signals [33]. However, this approach is more complicated and thus, we decided against it.

We chose a ZHDC-16-63+ directional coupler for its high directivity and low standing wave ratio (SWR). In addition, this directional coupler has a high, flat coupling value. Directivity is a measure of how well the backward traveling signal (reflected signal in this case) can be separated from the forward traveling signal (incident signal in this case). Thus having a directivity as high as possible is desired. SWR is the level of mismatch between the ports of the directional coupler. By minimizing the SWR, noise due additional, undesired reflections of the signals traveling through the directional coupler, is minimized. Lastly, the coupling value indicates the amount the

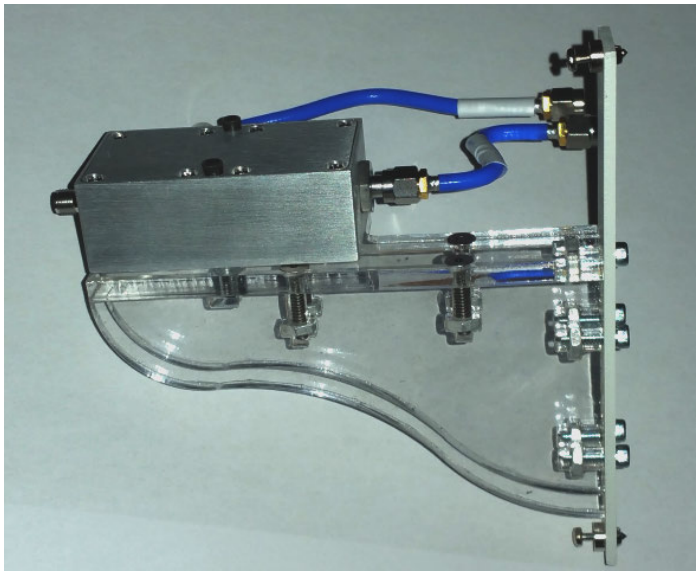

Figure 6-5: Directional coupler (Model: ZHDC-16-63+) mounted to the VST.

reflected signal is siphoned off at a given frequency. Hence, a high, flat coupling value is also desired [34].

The directional coupler is attached to the VST mechanically using a laser cut bracket and electrically using hand-flex cables. The bracket and cables are shown in Figure 6-5. We did this to ensure that the cables carrying the incident and reflected signals do not move during measurement as this would introduce distortions in the measured reflected signal, given that these are not phase stable under movement. Unfortunately, the directional coupler cannot be connected to the EQS sensor with such cables as the sensor may need to be moved to position itself relative to a target. Thus a phase stable cable is used here as it is a type of cable that does not distort the signal when moved.

Despite specifying and assembling the high-bandwidth measurement system, this system is still just a concept. The VST does not come preprogrammed to make S-parameter measurements and programming the VST proves to be a major roadblock. National Instruments gave support, but this was limited as according to National Instruments, it would take several months to program the VST to make S-parameter measurements and they already have other hardware capable of making these measurements. National Instrument's Vector Network Analyzers (VNAs)

make S-parameter measurements natively. However these VNAs have much lower data rates and cannot be freely programmed in LabVIEW Real Time, making them unsuitable substitutes.

6.2 High-Bandwidth Scanning System Concept

6.2.1 Design Requirements for High-Bandwidth Scanning

The high-bandwidth scanning system's design requirements include all the design requirements listed earlier for the test fixture before (Section 3.1) and after (Section 4.1.1) its redesign. Additionally, in order for the EQS sensors to scan an example IC photomask at the speeds in Table 1.1, two more functional requirements are needed:

High Speed

The scanning system should be able move the EQS sensor over a target as fast as possible while still satisfying the requirements for quasistatic imaging, (1.3).

Synchronization

The scanning system will need to be able to be coordinated with the measurement system in order to make images.

Based on all these design requirements, a concept for the scanning system is created.

6.2.2 Scanning Hardware

The concept scanning system consists of five components. However this system is not used as the incomplete high-bandwidth measurement system prevented us from having a high enough data rate sensor. These components are:

1. a Professional Instruments 4R Block-Head Twin-Mount air bearing spindle (S/N 52) from a diamond turning machine [35],

2. a custom New Way air bearing stage containing an Anorad linear motor (Model: LEB-S4) from a diamond turning machine [35],

3. the XY stage from the test fixture,

4. the rotation stage from the the test fixture redesign,

5. the tilt stage from the test fixture redesign.

To construct this scanning system concept, the tilt stage is placed between the XY and the rotation stages of the test fixture while the Z stage is replaced by the air bearing spindle on top of the air bearing stage.

The rotation, tilt, and XY stages are responsible for aligning the EQS sensor relative to targets on the air bearing spindle. The spindle and linear stage are responsible for sweeping the sensor over targets. The linear stage allows the sensor to sweep radially and to be positioned at different radii on the spindle. The spindle allows the sensor to sweep circumferentially. Together, the spindle and linear stage provide planar scanning in both polar directions.

We chose the Professional Instruments 4R Block-Head Twin-Mount air bearing spindle for its high speed, resolution, and range of travel, and its low error motion. This spindle is shown in Figure 6-6. Consider an EQS sensor positioned at radius of 38.89 mm (1.5 in) on the spindle. A target moving past the sensor here has a range of travel equal to the circumference of its circular path, 239.4 mm. Given that the spindle's Heidenhein encoder (Model: 1324) has 10,000 counts per revolution, the target can step with a 5.985 μm resolution using X4 encoding and zero interpolation. This is a large range of travel with resolution similar to that of the Z stage. In addition, the spindle is capable of rotating up to 1047 rad/sec (10^4 rpm). This translates to a maximum linear sweep speed of 38.89 m/sec at that radius which is more than enough. Lastly, the spindle has an error motion less than 25 nm so the mounted target will move a negligible amount orthogonal to the EQS sensor during its travel.

The New Way air bearing stage with an Anorad linear motor is a custom stage fabricated for a diamond turning machine [35]. It is shown in Figure 6-7. We chose

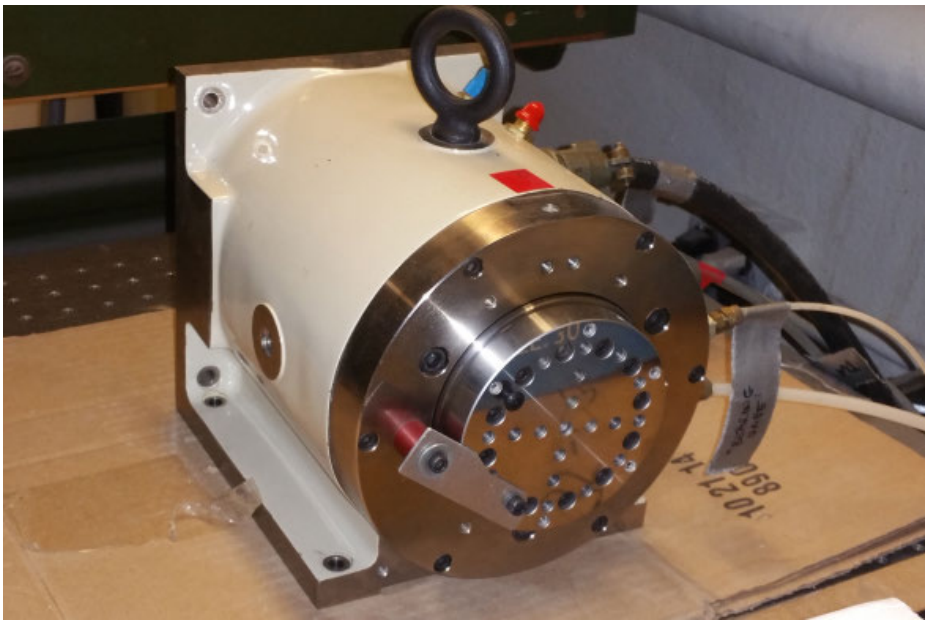

Figure 6-6: Professional Instruments 4R Block-Head Twin-Mount air bearing spindle for circumferential scanning of a target with an EQS sensor.

it for its resolution, range of travel and low error motion. In addition, it is capable of moving the spindle on top of it. The linear stage has a range of travel of 177 mm with a straightness of 5 μm/m. Thus a target mounted on the spindle would move at most 5 μm orthogonally to the EQS sensor during a radial sweep. Both of these specifications are adequate for the anticipated testing. The linear stage is paired with a Renishaw TONiC linear encoder (Model: Ti0200) to provide the stage with a resolution of 0.1 μm, which is more than acceptable.

Both the spindle and the linear stage require a source of clean, dry air. Otherwise, humidity can cause corrosion and particulates in the air can get stuck in the air bearing's fine, internal gaps, preventing the air bearing from operating properly. Therefore the air fed to the spindle and linear stage goes through two stages of cleaning as shown in Figure 6-8. First the air passes through a Topre refrigerated air dryer (Model: TPD-5C) with progressive filtering to dry the air. This progressive filtering consists of a main line filter (Model: AF40-N04-WZ-A), a mist separator (Model: AFM30-N03-WZ-A), and a micro mist separator (Model: AFD30-N03-WZ-A) to remove 99% of particles larger than 3 μm, 0.3 μm, and 0.01 μm respectively. Then the air passes through a D4-A Deliquescent Chemical Dryer (Model:4074) with additional filtering

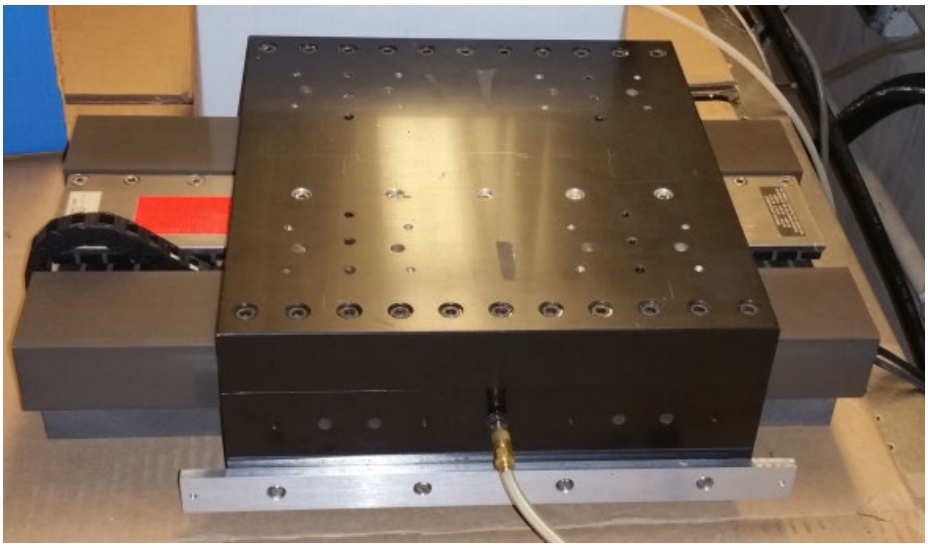

Figure 6-7: Custom New Way air bearing stage with an Anorad LEB-S4 linear motor for radially scanning of a target with an EQS sensor and for positioning the EQS sensor at a particular radius of the air bearing spindle.

to remove the oil from the air. This filtering consists of a Wilkerson particulate filter (Model: F16-02-00A-B91), a Wilkerson coalescing filter (Model: M16-02-000-A91), a Wilkerson particulate filter/regulator (Model: CB6-02-012A-E91), a Koby activated carbon air purifier (Model: Junior King), and another Wilkerson particulate filter (Model: F16-02-00A-B91) to remove 5 μm, 0.3 μm, 5 μm, 0.5 μm, and 5 μm oil particles respectively. Lastly, the air for the spindle passes through a quick-connect push fitting followed by a second Koby activated carbon air purifier (Model: Junior King). This allows the spindle to be detached from the air supply if necessary without risking contaminated air entering the spindle.

To control the spindle and the linear stage, a National Instruments PXIe-8135 controller with LabVIEW Real Time is used. This controller communicated with the spindle and linear stage via two R Series Multifunction RIO cards (Model: NI PXIe-7854R). R series cards are used as they contain a field-programmable gate array (FPGA), which can read signals at high frequencies. This is necessary to read high frequencies signals such as the pulses from the encoders of the spindle and the linear stage. All of these modules are contained in a NI PXIe-1082 Chassis with the VST in order to synchronize the concept measurement system with this concept scanning

(a) Stage 1: Refrigerated air dryer with progressive filtering to dry the air.

(b) Stage 2: Chemical air dryer with progressive filtering to remove oil from the air.

Figure 6-8: Filtration stages for the air supply fed from the building to the spindle and linear stage.

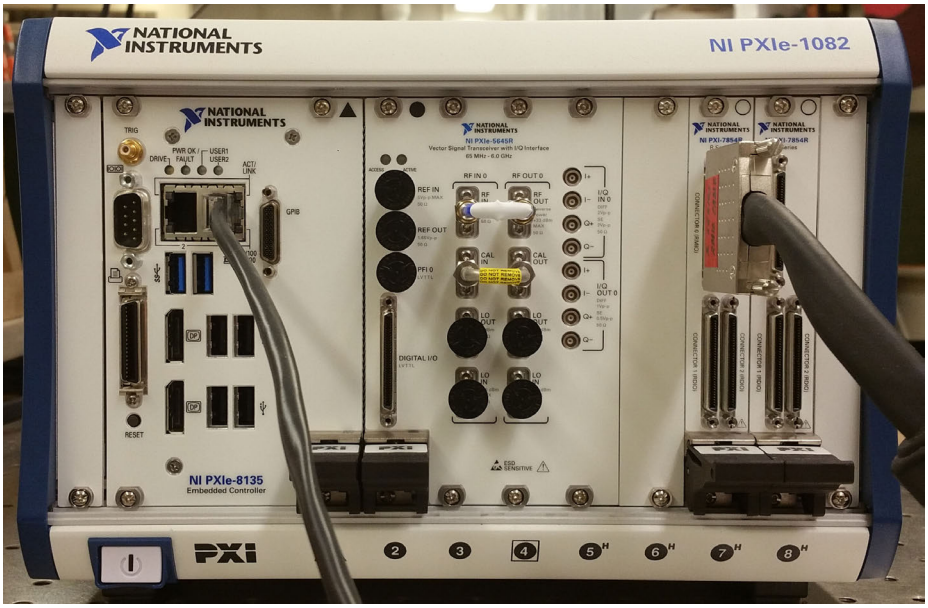

Figure 6-9: National Instruments PXIe-8135 controller with R series cards for controlling the spindle and linear stage.

system. This is shown in Figure 6-9.

6.3 Potential Performance

6.3.1 Potential Imaging Time

In the initial comparison between an EQS imaging system and AFM and SCM imaging systems (Section 1.3), assumptions were made about the potential EQS imaging system's excitation frequency $f_{\text{Excitation}}$, single-probe pixel imaging time T_{Measure}, and scan speed v_{Scan}. Using the properties of the concept measurement system and the concept scanning system, these parameters and in turn the imaging time of an EQS system can be more accurately estimated. The VST is capable for exciting an EQS sensor from 65 MHz to 6 GHz, frequencies adequate to support the first two EQS entries in Table 1.1.

Time T_{Measure} can be approximated from the VST's excitation frequency and the

frequency of its bandpass filter f_{Filter}:

$$T_{\text{Measure}} \approx N_{\text{Sweep}} \left(\frac{|\ln k_{\text{Tol}}|}{\pi f_{\text{Filter}}} + \frac{N_{\text{Sample}}}{f_{\text{Excitation}}} \right), \tag{6.5}$$

where N_{Sweep} is the number of excitation frequencies to measure at, k_{Tol} is the decimal representation of the percentage the previous signal should decay to before making measurements with the signal at a new excitation frequency, and N_{Sample} is the number measurements to be made at each excitation frequency and averaged together.

According to Rakesh Kumar, ADS requires the impedance and thus the S-parameters at a point to be measured over at least three frequencies to determine a measured capacitance for that point [5]. Further, the VST can be assumed to take an eight sample average like the impedance analyzer and waits for a previous signal to decay to a thousandth of its magnitude before making measurements with a new signal. Given the VST has an 80 MHZ bandpass filter, the VST can measure with a 1 GHz average excitation frequency at a rate of $T_{\text{Measure}}^{-1} = 9.4$ MHz, a rate also capable of supporting the first two EQS entries in Table 1.1.

In order to satisfy the conditions for quasistatic imaging, (1.3), the EQS imaging system can have a max scan speed of $v_{\text{Scan}} = 93.9$ mm/s. This speed is feasible using the spindle and also supports the first two EQS entries in Table 1.1. Again, we assume that stratifying (1.3) by a factor of 10 is sufficient. Using (1.2) with these new estimations, it would potentially take an EQS imaging system 12.3 days with a single probe and 3.0 hours with 100 probes to scan the example IC photomask. These imaging times are close to the initial estimate for an EQS imaging system to scan the example IC photomask. Table 6.1, an updated version of Table 1.1, compares these imaging times against the AFM and SCM imaging times.

6.3.2 Potential Resolution

Section 2.1 presented the lateral resolution of a probe and thus the concept imaging system, is roughly the dimensions of an electrode pair. However, this is the potential resolution of a probe if it is stationary. The lateral resolution for a moving probe in

Table 6.1: Updated Example IC Mask Scan Times for Various Imaging Systems

Imaging System	N_{Probe}	$f_{\text{Excitation}}$ [MHz]	T^{-1}_{Measure} [MHz]	v_{Scan} [mm/s]	T_{Scan}
AFM	1	0.6	0.06	0.6	5.3 yrs
SCM	1	915	20.00	5000.0	5.6 hrs
EQS	1	1000	93.94	93.9	12.3 days
EQS	100	1000	93.94	93.9	3.0 hrs

this concept EQS imaging system can be found by inserting the VST measurement time and spindle scan speed into (2.7). Assuming (2.7) can be satisfied by a factor of 10, the difference between the minimum feature size and characteristic length of the probe, $l_{\text{Feature}} - l_{\text{Probe}}$, is 10 nm. This translates to a potential lateral resolution of 10 nm greater than the electrode pair's dimensions for electrode pairs with dimensions greater than 1 nm and a potential maximum resolution of 10 nm for electrode pairs with dimensions less than 1 nm.

However, this potential resolution is the theoretical limit of the achievable resolution, not the system's actual resolution. In practice, the system's actual resolution may be noise limited to a lower value. This was not the case with Matey and Blanc's SCM though as their SCM did achieve its max resolution. The SCM had a lateral resolution of 0.1 μm with electrodes roughly 0.1 μm $\times$ 2.0 μm in dimension.

Noise in the impedance analyzer was mapped to noise in the orthogonal distance between the EQS sensor and the aluminum base (Section 4.3.1), but not to noise in the measured capacitance. Given these EQS sensors have a decent level of noise, we cannot determine the system's actual resolution due to noise limiting. We can determine the system's max potential resolution from the dimensions of its electrode arrays though. Given these dimensions (Figure 2-24), this system would have a max theoretical resolution of 0.6 mm $\times$ 23.4 mm. This theoretical resolution can be improved however by implementing these EQS sensors as ICs. Further, this would decrease the noise in the system, driving the system's actual resolution closer to this theoretical resolution.

6.4 Integrated Circuit EQS Sensors

The resolution and scan time of this concept EQS imaging system can be improved by implementing their EQS sensors as ICs. IC implementation would improve resolution for two reasons. First, it would drastically reduce the size of the electrode arrays, which would increase the max theoretical resolution of the system. A possible way to implement the electrode arrays as part of an IC would be to fabricate them from the IC's traces, similar to the method used by the buried trace EQS sensor. Second, IC implementation would eliminate the use of cables and minimize parasitics, reducing the noise in the system. With less noise, the system could detect smaller changes in capacitance, shifting the actual resolution of the system closer to its max theoretical resolution. Further, ICs can readily operate at higher frequencies.

As for improving scan times, an IC EQS sensor would have smaller, closer together components. In addition, IC implementation would allow these sensors to be mass produced. Lastly, the integrate circuit could contain both the sensor's electrode array and its drive/sense electronics. Then by combining multiples of these ICs into a larger IC, multiple parallel scanning probes could be implemented. The ability to implement parallel scanning probes is valuable as according to (1.2), this would linearly decrease the scan time.

On top of improving scan time, combining the electrode array and its drive/sense electronics into a single IC is space efficient and allows for easier integration of this imaging system into another system for quality control. Further IC implementation would allow the use of a switched topology for the drive/sense electronics for direct conversion of the measured capacitance changes to the digital domain. This would allow the measured changes in capacitance to be streamed at a high data rate from the sensor. Lastly, the measured capacitance changes could be immediately analyzed. Both of these would reduce the time needed for measurement.

6.5 Chapter Summary

This chapter presented the concepts for a high-bandwidth measurement system and a high-bandwidth scanning system that could be used with the high frequency EQS sensors to potentially image at high speeds. Further, implementation of these high frequency EQS sensors as ICs was discussed to improve the resolution and scan time of this concept EQS imaging system.

First, an explanation was provided for why EQS sensors operating at high excitation frequencies need to be characterized with S-parameters. From this explanation and the parameters needed for an EQS imaging system to image at high speeds, a list of design requirements was created for the concept measurement system to satisfy:

1. The measurement system should measure both the incident and reflected signals from an EQS sensor.

2. The measurement system should excite the senor with a frequency greater than 100 MHz.

3. The measurement system should measure the S-parameters of a sensor at multiple frequencies.

4. The measurement system should be able to be synchronized with the scanning system.

Based on these requirements, the concept measurement system consists of a National Instruments PXIe-5645R VST connected to a directional coupler, which is connected to the sensor. This concept was assembled, but never utilized as programming the VST to make S-parameter measurements is a major roadblock.

Next, the design requirements for the concept scanning system were presented. The concept scanning system needs to satisfy all the design requirements for the test fixture before (Section 3.1) and after (Section 4.1.1) its redesign. In addition, the scanning system needs to be able to move the sensor relative to the target at high speed and to be able to be synchronized with the measurement system.

To satisfy these design requirements, the rotation, tilt, and XY stage of the test fixture are used to position the EQS sensor relative to a target. The target is mounted to a Professional Instruments 4R Block-Head Twin-Mount air bearing spindle sitting on custom New Way air bearing stage containing an Anaroad linear motor. The spindle sweeps the sensor circumferentially over the target while the linear stage positions the senor at a specific radius of the spindle or sweeps the sensor radially over the target. This concept scanning system was not used however since the concept measurement system was not fully implemented.

Together, these concepts for a measurement system and scanning system supported the estimated time it would take an EQS imaging system to image the example IC photomask from Section 1.3. Table 1.1 was reiterated as Table 6.1 to reflect the imaging time of a concept EQS imaging system made from these measurement system and scanning system concepts. Further, this concept EQS imaging system was shown to have a theoretical maximum lateral resolution of 0.6 mm using the variable spatial wavelength EQS sensors. This resolution can be increased by rebuilding the EQS sensors as ICs.

Chapter 7

Conclusions & Suggestions for Future Work

Previously, EQS sensors have been suggested as a potential high speed alternative for imaging surface and subsurface defects in IC fabrication [4, 21]. To image at high speeds, EQS sensors need to utilize a combination of high measurement frequencies and parallel scanning probes. This thesis in conjunction with Rakesh Kumar's Master's thesis [5] continued the investigation into EQS sensors for high speed imaging by exploring EQS sensors driven with high excitation frequencies. In particular, this thesis presented the design and development of electrode arrays that can be driven with high excitation frequencies and thus can potentially image at high-bandwidths (Chapter 2). These electrode arrays are combined with drive electronics developed by Rakesh Kumar to create high frequency EQS sensors. The design and development of test fixtures for testing these EQS sensors was then covered here (Chapters 3 and 4). Experiments conducted jointly with Rakesh Kumar showed these EQS sensors are able to detect changes in a scanned target's geometric (variable air gap) and material (dielectric step) properties (Chapter 5). Finally a concept for a high-bandwidth imaging system utilizing these EQS sensors was presented along with the concept of implementing these EQS sensors as ICs (Chapter 6).

In Chapter 2: Design & Fabrication of Macro-Scale EQS Electrode Arrays, the development of electrodes arrays that can be driven with high excitation frequencies

was discussed. We built four electrode arrays in total: a buried trace electrode array, a simple unguarded electrode array, and two variable spatial wavelength electrode arrays. Changes in capacitance were observed when the later three electrode arrays were stepped from an aluminum base, but not when the buried trace electrode array was stepped from the aluminum base. This is primarily due the later three electrode arrays having an increased sense area. The sense area of the buried trace electrode array is small enough that the changes in capacitance measured were less than the system's noise floor, and thus not observable. In future EQS electrode arrays, particular attention should be paid to maximizing each electrode's sense area and reducing its detection electronic's noise.

The sense area of an electrode can be increased by increasing its dimensions. However this is unfavorable as the lateral resolution of each electrode is roughly the size of its dimensions (Sections 2.1 and 6.3.2). By reciprocity, changes in capacitance sensitivity can also be made observable by lowering the sensor's noise floor. Multiple steps were taken to reduce the noise in these electrode arrays' high frequency drive electronics, but in the end, the high frequency drive electronics were still fairly noisy [5]. Future work might include reducing the noise in these high frequency drive electronics. One possible method is to consolidate these drive electronics into an IC as ICs have smaller parasitics than PCBs and can readily operate at higher frequencies. In addition to shrinking the drive electronics, future work could also include shrinking the electrode arrays to the MEMS scale. The electrode array could be implemented as part of the IC containing the drive electronics. This would allow for much higher resolution imaging.

Chapter 3: Initial Test Fixture Design and Testing presented an initial design for the test fixture used to test the EQS sensors. This initial test fixture positioned, but did not orient the EQS sensors relative the an aluminum base. As a result, undesirable vertical and horizontal tilt existed between the sensors and base. This horizontal tilt caused the sensor to prematurely contact the base in the initial Variable Air Gap Experiment, resulting in the measured capacitance leveling off when the air gap was below 20 μm as shown in Figure 3-4. The vertical tilt caused a gradual increase in

the air gap and in turn a gradual decrease in the measured capacitance in the initial Dielectric Step Experiment as shown in Figure 3-6.

To mitigate the effects of these misalignments, the test fixture was redesigned so it could also angularly orient the EQS sensors relative to the base. Further, the sensors were used to tram themselves and the axes of motions relative to the base. This redesign of the test fixture and improved alignment procedure were presented in Chapter 4: Final Test Fixture Design and Testing. However, this alignment procedure was time consuming and in conjunction with the redesign, only brought the sensors within micron coplanar alignment with the base. For the experiments presented here, micron alignment is sufficient. However for future sensors with MEMS or even nano-scale electrode arrays, finer alignment would be needed. Thus another area of future research would be in bringing EQS sensors into co-planar alignment with targets. In particular, automation of the alignment process under closed loop feedback in real time would be desirable as it would reduce the time needed to align the sensors, reduce human error introduced in aligning the sensor by hand, and is required for fast scanning.

Chapter 5: Scanning Experiments & Results showed changes in capacitance due to changes in the target's material and geometric properties could not only be measured, but reasonably modeled. Figures 5-2 and 5-3 from the final Variable Air Gap Experiments show the measured capacitance inversely decreases as the thickness of the air gap increases as predicted by the single dielectric parallel plate + fringe field model, (2.5). Figures 5-4 and 5-5 from the final Dielectric Step Experiments show the measured capacitance step when the EQS sensors passed from completely off to completely on the strip of Kapton tape as predicted by double dielectric parallel plate + fringe field model, (2.6).

Deviations in both set of experiments can be accredited to four sources:

Misalignment of the EQS Sensors

Capacitance measured by the EQS sensors is very sensitive to the distance between the sensors and the target. As shown in Figure 4-2, misalignments

of the sensor relative to the target cause changes in this distance. Since the sensors can never be brought into prefect co-planar alignment with targets, future work could also include characterizing the sensors misalignment with an external metrology setup. For example, capacitance probes can be arranged to externally measure the sensor's position and orientation relative to the target.

Manufacturing Defects in the Electrode Arrays

Manufacturing defects contributed to the measured capacitance deviating from the predicted capacitance in two ways. First, the models assumed the electrode arrays were coplanar with the targets. Even if the test fixture could perfectly align the sensors, coplanar alignment would still not be achieved as the face of an electrode array is not perfectly flat. To mitigate this, the electrode arrays were lapped to make it as flat as possible. However, the flatness of the electrode array could be improved in future work, especially with MEMS fabrication techniques.

Second, significant fringing contributed to the capacitance measured by the sensors. This is undesirable, as it is much harder to account for transitions in material and geometric properties with the fringing field capacitance models; the fringing field models increase the difficulty of the inverse problem of determining material and geometric properties from changes in capacitance. Fringing was significant due to the large epoxy gaps between the sense electrodes and their surrounding guard electrodes. There will always be a gap between the sense and guard electrodes so they are electrically isolated, but this gap could be minimized in future work through MEMS fabrication techniques too.

Errors in Circuit Parameter Optimization

In all of the experiments, the capacitance between the electrode array and a target was not directly measured. Instead, the impedance of the electrode arrays and the drive electronics was measured and converted by Rakesh Kumar to capacitance using the software program Advanced Design System (ADS) by

Agilent (Section 3.3). Thus deviations in the measured capacitance from the models could be a result of errors in the ADS tuning of the parasitic circuit model of the sensor, Figure 3-3. As a result, future work could include an investigation into ADS as an appropriate tool for determining board parasitics or if there is a more appropriate tool. Alternatively, the driving and sensing ports could be separated for the sensors. Instead, the sensing ports could be located between the electrode arrays and their drive electronics so that the capacitance between the electrode array and target is directly measured.

System Noise

Lastly, noise in the drive electronics and the impedance analyzer was significant and is a large source of error. Thus as mentioned before, future work must include reducing the noise in the drive electronic and in the measurement equipment. This could be done by fabricating the electrode arrays and drive/sense electronics together as an IC.

Lastly, Chapter 6: Concept for High Speed Imaging System discussed potential components for using the high frequency EQS sensors for high-bandwidth imaging. Using a National Instruments VST in conjunction with an air bearing spindle and linear stage, this concept system could potentially use the sensors to measure at v_{Scan} = 94 mm/s with a rate of T_{Measure}^{-1} = 9 MHz. These two values are adequate to support the first two EQS entries in Table 1.1. However to operate at these speeds, the VST would need to make S-parameter measurements, and programming the VST to make S-parameter measurements was a major roadblock. Thus a last recommendation for future work is working with National Instruments to provide their VSTs with S-parameter measurement functionality. Alternatively, custom capacitance measurement circuitry like SCMs have could be designed and integrated into the sensor's drive electronics.

In conclusion, this thesis has provided an initial investigation into the use of EQS sensors for high speed imaging. These preliminary results suggest that this is a promising approach for future measurement tasks, such as imaging critical pho-

tomask defects. Further work in this area is justified for creating new measurement approaches.

Bibliography

[1] J. P. De Gyvez, *Integrated Circuit Defect-Sensitivity: Theory and Computational Models*. Norwell, MA: Kluwer Academic Publishers, 1992.

[2] C. H. Stapper, "Modeling of integrated circuit defect sensitivities," *IBM Journal of Research and Development*, vol. 27, no. 6, pp. 549–557, 1983.

[3] B. C. Kress and P. Meyrueis, *Applied Digital Optics: From Micro-optics to Nanophotonics*. West Sussex, UK: Wiley, 2009.

[4] B. L. Cannon, "Electroquasistatic sensors for surface and subsurface nano-imaging of integrated circuit features," Master's Thesis, Electrical Engineering and Computer Science, Massachusetts Institute of Technology, Cambridge, MA, 2010.

[5] R. Kumar, "High bandwidth microscale imaging," Master's Thesis, Electrical Engineering and Computer Science, Massachusetts Institute of Technology, Cambridge, MA, 2016.

[6] M. R. Rodgers, M. A. Wendman, and F. D. Yashar, "Application of the atomic force microscope to integrated circuit failure analysis," *Microelectronics Reliability*, vol. 33, no. 11, pp. 1947–1956, 1993.

[7] S. Dana and J. Bach, "Afm-based lithography metrology tool," U.S. Patent 6,392,229 B1, May 21, 2002.

[8] G. Binnig, C. F. Quate, and C. Gerber, "Atomic force microscope," *Physical review letters*, vol. 56, no. 9, pp. 930–933, 1986.

[9] G. Meyer and N. M. Amer, "Novel optical approach to atomic force microscopy," *Applied physics letters*, vol. 53, no. 12, pp. 1045–1047, 1988.

[10] T. Ando, N. Kodera, Y. Naito, T. Kinoshita, K. Furuta, and Y. Y. Toyoshima, "A high-speed atomic force microscope for studying biological macromolecules in action," *ChemPhysChem*, vol. 4, no. 11, pp. 1196–1202, 2003.

[11] J. R. Matey, "Scanning capacitance microscope," U.S. Patent 4,481,616, Nov. 6, 1984.

[12] J. R. Matey and J. Blanc, "Scanning capacitance microscopy," *Journal of Applied Physics*, vol. 57, no. 5, pp. 1437–1444, 1985.

[13] R. C. Palmer, E. J. Denlinger, and H. Kawamoto, "Capacitive-pickup circuitry for videodiscs," *RCA Review*, vol. 43, no. 1, pp. 194–211, 1982.

[14] Y. Sheiretov, "Deep penetration magnetoquasistatic sensors," PhD Thesis, Electrical Engineering and Computer Science, Massachusetts Institute of Technology, Cambridge, MA, 2001.

[15] N. F. Sheppard, D. R. Day, H. L. Lee, and S. D. Senturia, "Microdielectrometry," *Sensors and Actuators*, vol. 2, pp. 263–274, 1982.

[16] M. C. Zaretsky, "Parameter estimation using microdielectrometry with applications to transformer monitoring," PhD Thesis, Electrical Engineering and Computer Science, Massachusetts Institute of Technology, Cambridge, MA, 1987.

[17] P. A. von Guggenberg, "Application of interdigital dielectrometry to moisture and double layer measurements in transformer insulation," PhD Thesis, Electrical Engineering and Computer Science, Massachusetts Institute of Technology, Cambridge, MA, 1993.

[18] Y. Sheiretov and M. Zahn, "Dielectrometry measurements of moisture dynamics in oil-impregnated pressboard," *IEEE Transactions on Dielectrics and Electrical Insulation*, vol. 2, no. 3, pp. 329–351, 1995.

[19] D. E. Schlicker, "Imaging of absolute electrical properties using electroquasistatic and magnetoquasistatic sensor arrays," PhD Thesis, Electrical Engineering and Computer Science, Massachusetts Institute of Technology, Cambridge, MA, 2005.

[20] N. J. Goldfine, A. P. Washabaugh, and D. E. Schlicker, "High-resolution inductive array imaging of buried objects," in *SPIE Proceedings*, vol. 4038. International Society for Optics and Photonics, 2000, pp. 56–65.

[21] R. Kumar, T. Hamer, J. H. Lang, and D. L. Trumper, "Towards high-bandwidth capacitive imaging," in *2016 IEEE Sensors*, Oct. 2016, pp. 1–4.

[22] C. P. Hare and A. N. Erickson, "Software synchronization of multiple scanning probes," U.S. Patent 2005/0097944 A1, May 12, 2005.

[23] H. W. P. Koops, "Multi-probe test head and process using same," U.S. Patent 6,426,499 B1, July 30, 2002.

[24] P. Vettiger, G. Cross, M. Despont, U. Drechsler, U. Durig, B. Gotsmann, W. Haberle, M. Lantz, H. Rothuizen, R. Stutz, and G. Binnig, "The" millipede"-nanotechnology entering data storage," *IEEE Transactions on nanotechnology*, vol. 1, no. 1, pp. 39–55, 2002.

[25] M. Culpepper, "2.72: Elements of mechanical design lecture 05 - structures," Course Notes, Massachusetts Institute of Technology, 2014.

[26] R. G. Budynas and J. K. Nisbett, *Shigley's Mechanical Engineering Design*, 9th ed. New York, NY: McGraw-Hill Education, 2011.

[27] "AISI 1095 steel, annealed at 790°C (1450°F)," *MatWeb: The online materials information resource*, Automations Creations, Inc., 1997. [Online]. Available: www.matweb.com/search/DataSheet.aspx?MatGUID=82b0d5fe53214415b27997c49964fd00

[28] *Agilent Network Analyzer Basics*, 5965-7917E, Agilent Technologies, Aug. 2004. [Online]. Available: cp.literature.agilent.com/litweb/pdf/5965-7917E.pdf

[29] *Introduction to Network Analyzer Measurements*, National Instruments, 2012. [Online]. Available: download.ni.com/evaluation/rf/Introduction_to_Network_Analyzer_Measurements.pdf

[30] D. Anderson, L. Smith, and J. Gruszynski, *S-Parameter Techniques for Faster, More Accurate Network Design*, Test & Measurement Application Note 95-1, Hewlett-Packard, Nov. 1996. [Online]. Available: www.ieee.li/pdf/viewgraphs/s_parameter_techniques.pdf

[31] *Directional Couplers*, Mini-Circuits, Sept. 1999. [Online]. Available: www.minicircuits.com/app/COUP7-2.pdf

[32] "PXIe-5644R/5645R/5646R," National Instruments, 2016. [Online]. Available: sine.ni.com/nips/cds/view/p/lang/en/nid/210629

[33] E. Zenteno, M. Isaksson, D. Wisell, N. Keskitalo, and O. Andersen, "An envelope domain measurement test setup to acquire linear scattering parameters," in *Microwave Measurement Symposium, 2008 72nd ARFTG*. IEEE, 2008, pp. 54–57.

[34] *Directional Couplers and Bridges*, Agilent Technologies, Dec. 2000. [Online]. Available: www.livingston-products.com/products/pdf/152973_1_en.pdf

[35] S. J. J. Ludwick, "A rotary fast tool servo for diamond turning of asymmetric optics," PhD Thesis, Mechanical Engineering, Massachusetts Institute of Technology, Cambridge, MA, 1996.

[36] J. Neher, *Cable Diagram*, Engineering Drawing 29-57300-316, Professional Instruments Company, Aug. 1998.

[37] "Wiring devices - NEMA diagrams," in *2016 Fall Company and Product Summary*. AutomationDirect, Sept. 2016, pp. 192–196. [Online]. Available: www.automationdirect.com/static/specs/wiringdevicesnemawiring.pdf

[38] J. Neher, *Pin-Out, Spindle*, Engineering Drawing 29-57300-263, Professional Instruments Company, Oct. 1997, no. 3.

[39] *D4-A Operator's Manual*, Professional Instruments Company, Oct. 1997.

[40] J.-y. Chang, *Six Hints For Better Scope Probing*, Test & Measurement World EDN web cast, Agilent Technologies, Dec. 2007. [Online]. Available: www.keysight.com/upload/cmc_upload/All/Probing-6-Hints-Scopes-Dec12-2007-webcast.pdf?&cc=US&lc=eng

[41] *Eight Hints for Better Scope Probing*, Application Note 1603, Agilent Technologies, Oct. 2013. [Online]. Available: cp.literature.agilent.com/litweb/pdf/5989-7894EN.pdf

Appendix A

Vendors & Parts List

This appendix contains the parts used through out this project along their vendors and manufacturers.

DGI Supply
1480 South Wolf Road, Wheeling, IL 60090
Tel: (800) 923-6255
Url: www.dgisupply.com

Part	*Part No.*	*Notes*
DoALL gage block cleaner	RAM62200082	Cleaner for air bearing spindle

Heidenhain Corporation
222 Remington Road, Schaumburg, IL 60173
Tel: (847) 490-1191 E-mail: info@heidenhain.com
Url: www.heidenhain.com

Keysight Technologies, Inc.
formerly Agilent Technologies
1400 Fountaingrove Parkway, Santa Rosa, CA 95403
Tel: (800) 829-4444 E-mail: usa_orders@keysight.com
Url: www.keysight.com

Part	*Model*	*Notes*
Impedance analyzer	4395A	10 Hz to 500 MHz freq. range
Advanced Design System (ADS)		Software for circuit analysis

Koby Inc.
297 Lincoln Street, Marlboro, MA 01752
Tel: (508) 481-8348 E-mail: saleskobyfilters@aol.com
Url: www.kobyfilters.com

McMaster-Carr
200 New Canton Way, Robbinsville, NJ 08691
Tel: (609) 689-3000 E-mail: nj.sales@mcmaster.com
Url: www.mcmaster.com

Part	*Part No.*	*Notes*
Brass Yor-Lok tube fittings	5272K604	Fittings for air supply

Melles Griot
200 Dorado Place SE, Albuquerque, NM 87123
Tel: (505) 298-2550 E-mail: iopmarketplace@idexcorp.com
Url: www.mellesgriot.com

Part	*Model*	*Notes*
Micrometer-driven rotation stage	98 mm Dia.	10° range

Mini-Circuits
13 Neptune Avenue, Brooklyn, NY 11235
Tel: (718) 934-4500 E-mail: sales@minicircuits.com
Url: www.minicircuits.com

Connecting the EQS sensor to the VST:

Part	*Model*	*Notes*
Directional coupler	ZHDC-16-63+	65 MHz - 6 GHz freq. range
3 in. hand-flex cable	141-3SM+	SMA male to SMA male
4 in. hand-flex cable	141-4SMRSM+	SMA-right male to SMA male
Phase stable cable	KBL-2FT-PHS+	2.92 mm male to 2.92 mm male

Motion Control Systems Inc.
New River Industrial Park PO Box 115, New River, VA 24129
Tel: (540) 731-0540 E-mail: solution@motioncontrol.org
Url: www.motioncontrol.org

National Instruments Corporation
11500 Mopac Expressway, Austin, TX 78759
Tel: (512) 683-0100
Url: www.ni.com

Contact: Haley Nesmith

Part	*Model*	*Notes*
LabVIEW 2015		Visual programming language
PXIe chassis	PXIe-1082	2 GB/s slot bandwidth
PXIe controller	PXIe-8135	2.3 GHz quad-core
Vector signal transceiver (VST)	PXIe-5645R	65 MHz - 6 GHz freq. range
Two R series FPGA I/O cards	PXI-7854R	8 AI, 8 AO, & 96 DIO
Two R series cables	SHC68-68-RMIO	Cables for RMIO port
Two breakout boxes	SCB-68A	

Newport Corporation
1791 Deere Avenue, Irvine, CA 92606
Tel: (949) 863-3144
Url: www.newport.com

Part	*Model*	*Notes*
ULTRAlign XY linear stage	461-XY-M	13 mm range
Two vernier micrometers	SM-13	13 mm range
Triple divide Z axis translation stage	9064-Z	28 mm range
Vernier micrometer	SM-25	25 mm range

New Way Air Bearings
50 McDonald Boulevard, Aston, PA 19014
Tel: (610) 494-6700 E-mail: tclaffey@newwayairbearings.com
Url: www.newwayairbearings.com

Part	*Notes*
Custom linear air bearing stage†	Boxway air cross slide similar to P/N S4030501

† Part originally obtained by Steve Ludwick [35].

OSH Park LLC
543 3rd Street C12, Lake Oswego, OR 97034
Tel: (503) 616-2484 E-mail: support@oshpark.com
Url: www.oshpark.com

Part
Three buried trace EQS sensor PCBs
Six variable wavelength EQS sensor PCBs

Professional Instruments Company
7800 Powell Road, Hopkins, MN 55343
Tel: (952) 933-1222 E-mail: pico@airbearings.com
Url: www.airbearings.com

Contact: Jeff Perry

Air bearing spindle†:

Part	*Model*	*Notes*
Motorized air bearing spindle	4R Twin-Mount	
Rotary encoder[1]	ERO 1324	10,000 Count
PWM amplifier[2]	SA-1000	Conf. B1021-F
Desiccant pillows		

Chemical air dryer†:

Part	*Model*	*Notes*
D4-A chemical air dryer[3]	4074	
Two particulate filters[4]	F16-02-00A-B91	5 μm filter
Filter/regulator[4]	CB6-02-012A-E91	5 μm filter
Coalescing filter[4]	M16-02-000-A91	0.3 μm filter
Two activated carbon filters[5]	Junior King	0.5 μm filter
Replacement filter kit	Size 16	
Dry-O-Lite desiccant tablets[3]		12 lbs. bucket

† Parts originally obtained by Steve Ludwick [35]
1 Manufactured by Heidenhein Corporation.
2 Manufactured by Motion Control Systems Inc.
3 Manufactured by Van Air Systems.
4 Manufactured by Wilkerson Corporation.
5 Manufactured by Koby Inc.

Renishaw Inc.
5277 Trillium Boulevard, Hoffman Estates, IL 60192
Tel: (847) 286-9953 E-mail: usa@renishaw.com
Url: www.renishaw.com

Contact: Charlie Falco

Linear encoder for air bear stage:

Part	*Part No.*	*Notes*
TONiC linear readhead	T1001-30A	For RGSZ20 scale, 30 m long cable
TONiC digital interface	Ti4000A40A	5 nm resolution, 40 MHz min clock freq.
TONiC analog interface	Ti0000A00A	
TONiC RGSZ20 scale	A-9420-0100	1000 mm long, gold-plated, flexible scale
Scale applicator tool	A-9653-0182	
Scale end clamps	A-9523-4015	Clamps to hold down scale ends
TONiC P limit magnet	A-9653-0138	Serves as limit switch at one end
TONiC Q limit magnet	A-9653-0139	Serves as limit switch at other end

Rockwell Automation
formerly Anorad Corporation
1201 South Second Street, Milwaukee, WI 53204
Tel: (414) 382-2000 E-mail: anorad@anorad.com
Url: www.rockwellautomation.com/global/anorad

Air bearing stage linear motor†:

Part	*Part No.*	*Notes*
LEB-S4 linear motor coil	40491-C-S-T	
LEB linear motor magnet channel	42670	450 mm long
D.C. servo amplifier	73769	160 V Output
Motor/hall cable	72960-2	
Motor extension cable	73479-10	
Hall extension cable	73480-10	
Command extension cable	73481-3	

† Parts originally obtained by Steve Ludwick [35].

SMC Corporation of America
3810 Prospect Avenue Unit A, Yorba Linda, CA 92886
Tel: (714) 312-5419
Url: www.smcpneumatics.com

Filters for refrigerated air dryer:

Part	*Part No.*	*Notes*
Main line filter	AF40-N04-WZ-A	3 μm filter
Mist separator	AFM30-N03-WZ-A	0.3 μm filter
Micro mist separator	AFD30-N03-WZ-A	0.01 μm filter
Pressure regulator	AR30-N03G-NYZ-A	
Pressure switch	IS10M-30-6LP-A	0.2 - 0.6 MPa range
1/2 in. NPT piping adapter	E300-N04-A	For refrigerated dryer connection
1/4 in. NPT piping adapter	E300-N02-A	For chemical dryer connection
Five component interfaces	Y300-A	Connects filters together
Water separator	AMG350C-N04	Collects water from dryer

Topre Corporation
Asahi Building, 12-2, Nihonbashi 3-chome, Chuo-ku, Tokyo, 103-0027, Japan
Tel: 81 (3) 3271-0711
Url: www.topre.co.jp/en/

Part	*Model*
Refrigerated Air Dryer	TPD-5C

Van Air Systems
2950 Mechanic Street, Lake City, PA 16423
Tel: (814) 774-2631 E-mail: orders@vanairsystems.com
Url: www.vanairsystems.com

Wilkerson Corporation
8676 East M89 PO Box 901, Richland, MI 49083
Tel: (877) 321-4736 E-mail: pdnmktg@parker.com
Url: www.wilkersoncorp.com

Appendix B

Plumbing & Wiring Diagrams

This appendix contains diagrams for:

1. Wiring the air bearing spindle.
2. Plumbing the refrigerated air dryer.
3. Plumbing the chemical air dryer.

B.1 Spindle & Amplifier Wiring Diagrams

Power from Wall to Amplifier

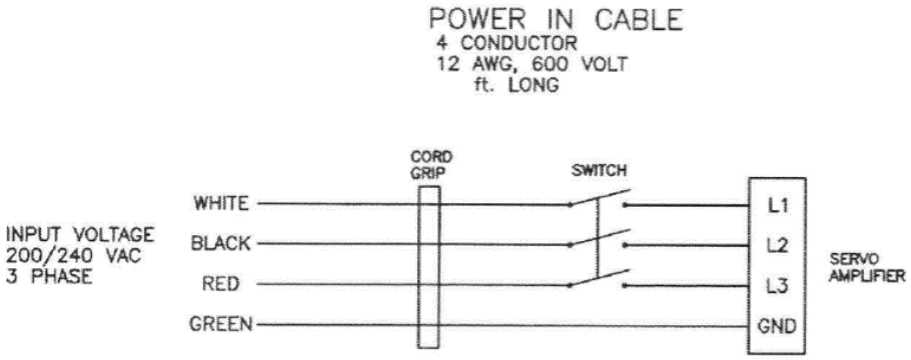

Figure B-1: Wiring diagram for power from the wall to the spindle's amplifier. Taken from [36].

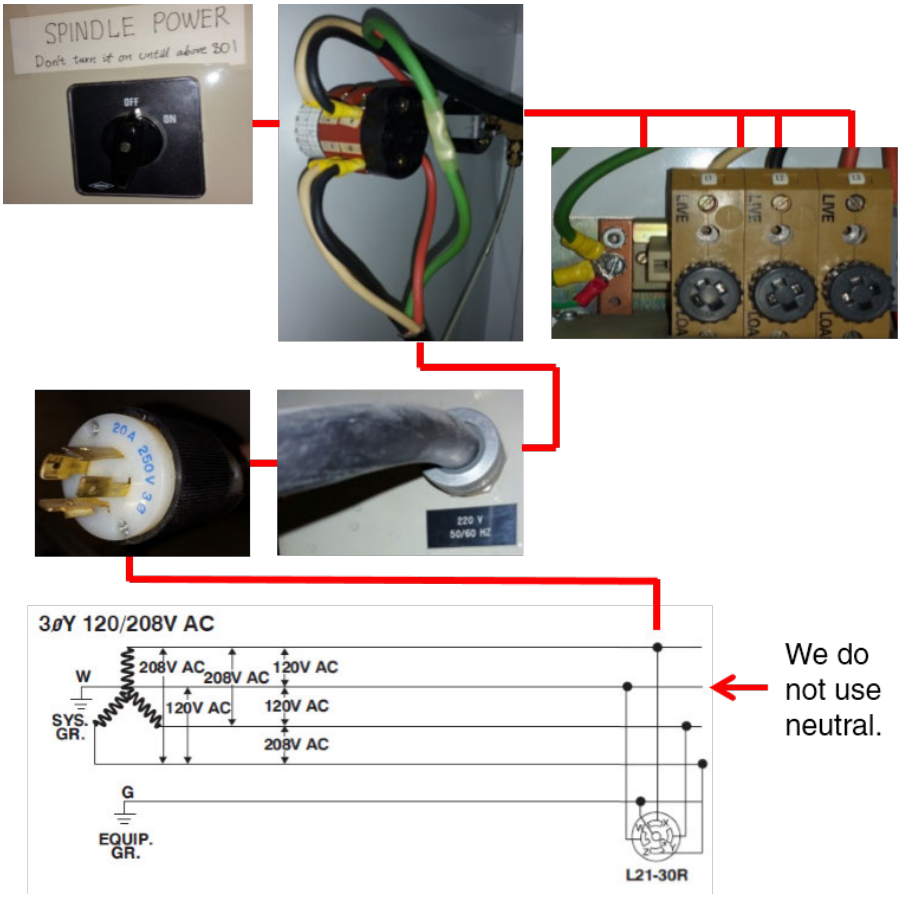

Figure B-2: Wiring for power from the wall to the spindle's amplifier. Wall wiring taken from [37].

Power from Amplifier to Motor

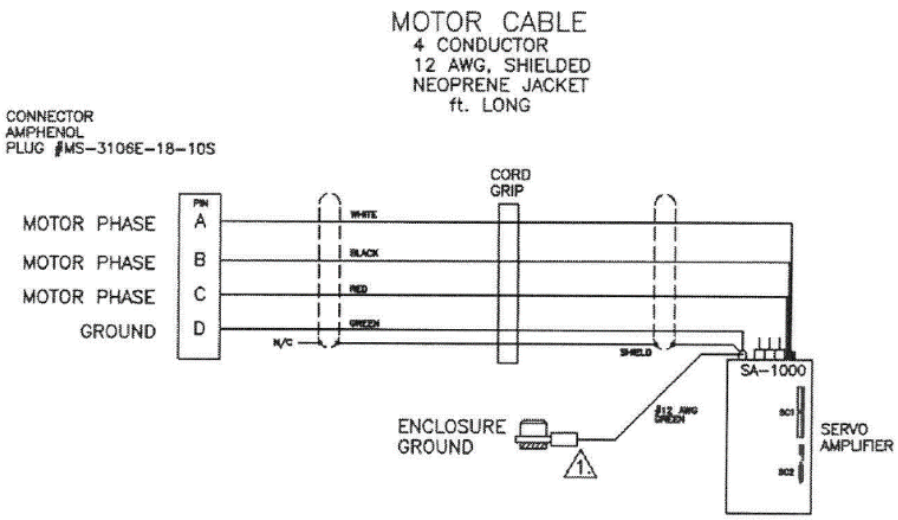

Figure B-3: Wiring diagram for power from the spindle's amplifier to its motor. Taken from [36].

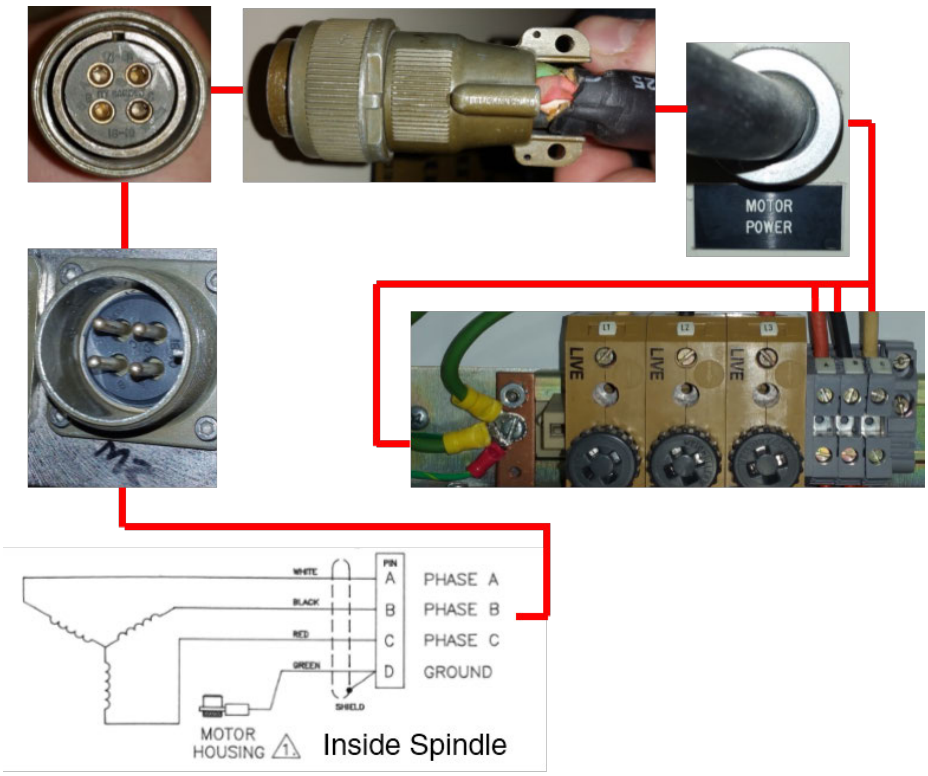

Figure B-4: Wiring for power from the spindle's amplifier to its motor. Motor wiring taken from [38].

Feedback Signal from Motor to Amplifier

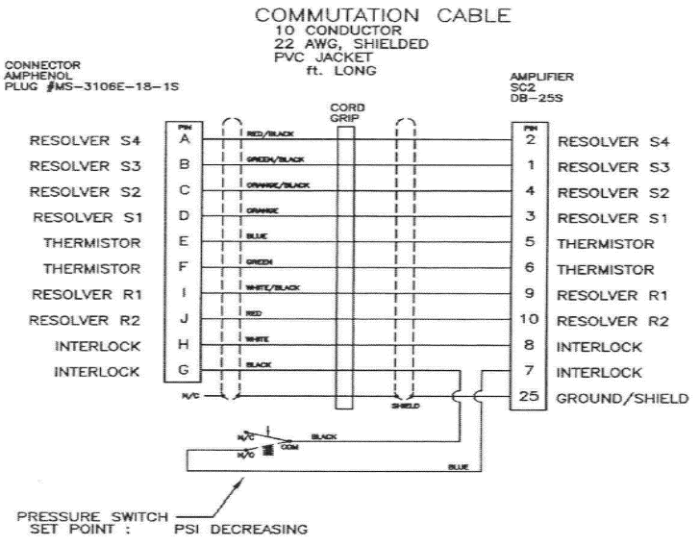

Figure B-5: Wiring diagram for feedback signal from the spindle's motor to its amplifier. Taken from [36].

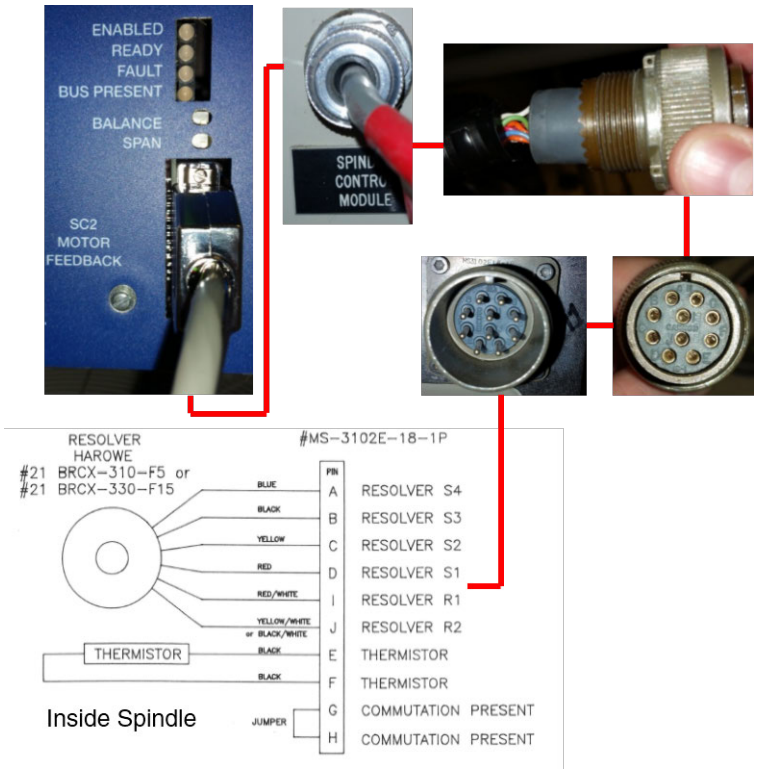

Figure B-6: Wiring for feedback signal from the spindle's motor to its amplifier. Resolver wiring taken from [38].

Command Signal from Controller to Amplifier

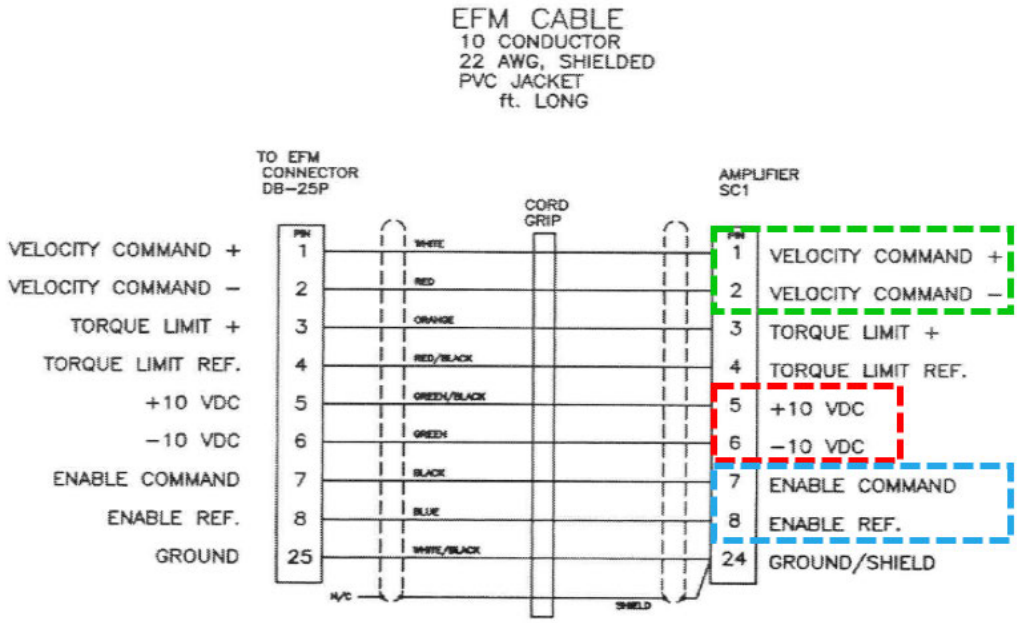

Figure B-7: Wiring diagram for command signal from the controller to the spindle's amplifier. Taken from [36].

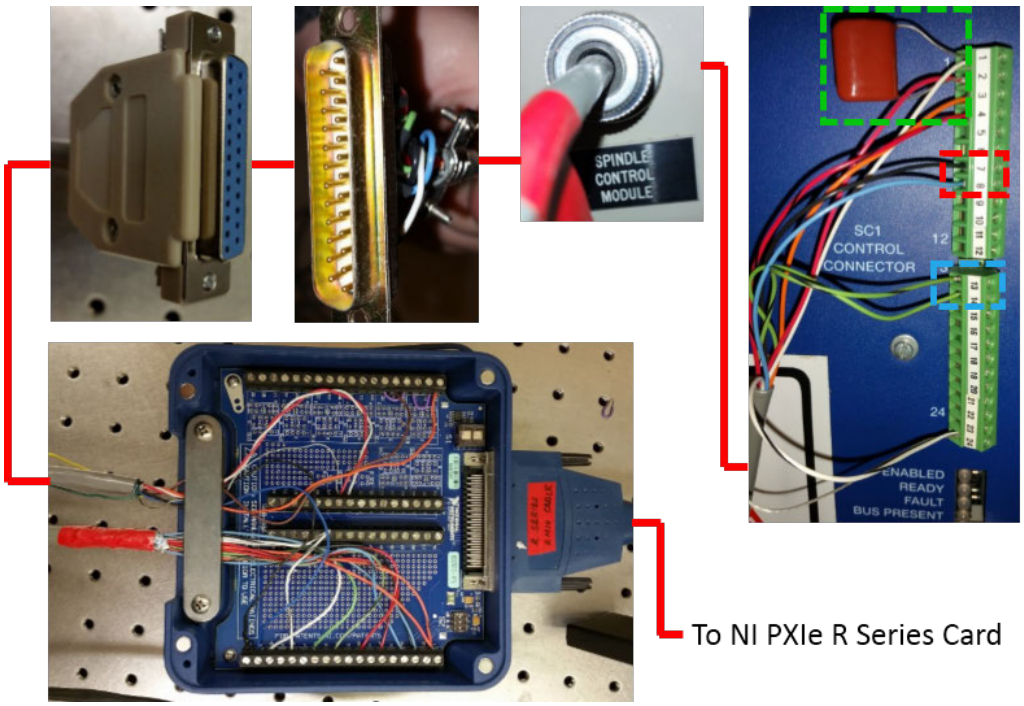

Figure B-8: Wiring for command signal from the controller to the spindle's amplifier.

Capacitor across the differential input terminals reduces high-frequency noise, which could produce drift in the set point (voltage at which the spindle speed is zero), introduce noise into the power supply output, or both.

$+10V$ } These outputs are not used so they are wired to pins 13 & 14, which are
$-10V$ } opens.

ENABLE COMMAND: 5 V Output
ENABLE REFERENCE: Digital Input
- Spindle Disabled: 5 V from ENABLE COMMAND
- Spindle Enabled: Grounded

Feedback Signal from Motor to Controller

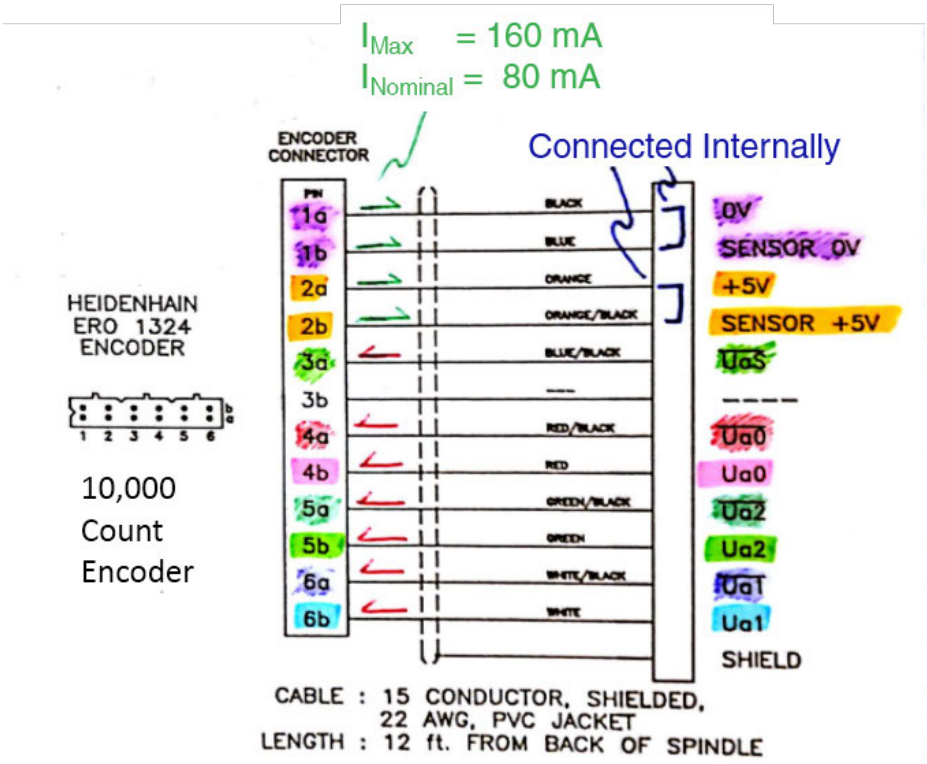

Figure B-9: Wiring diagram for feedback signal from the spindle's motor to the controller. Adapted from [38].

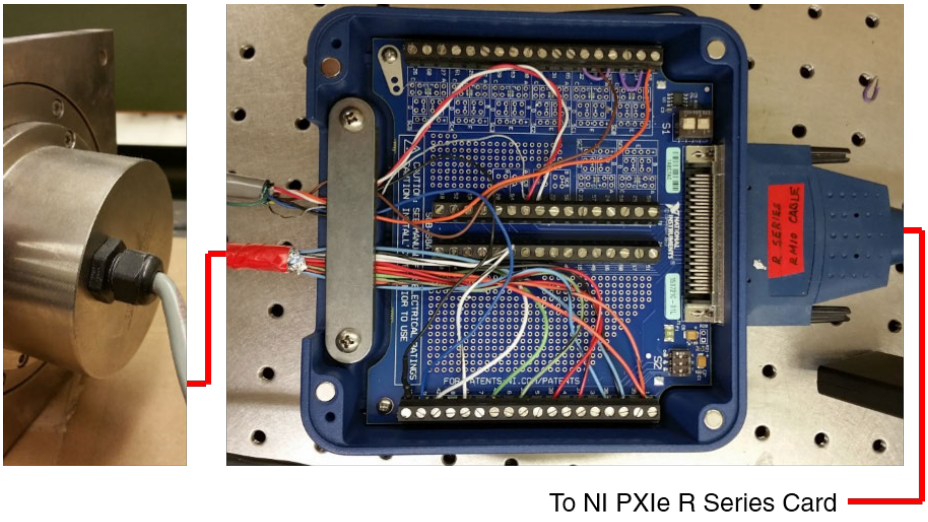

Figure B-10: Wiring for feedback signal from the spindle's motor to the controller.

Breakout Box

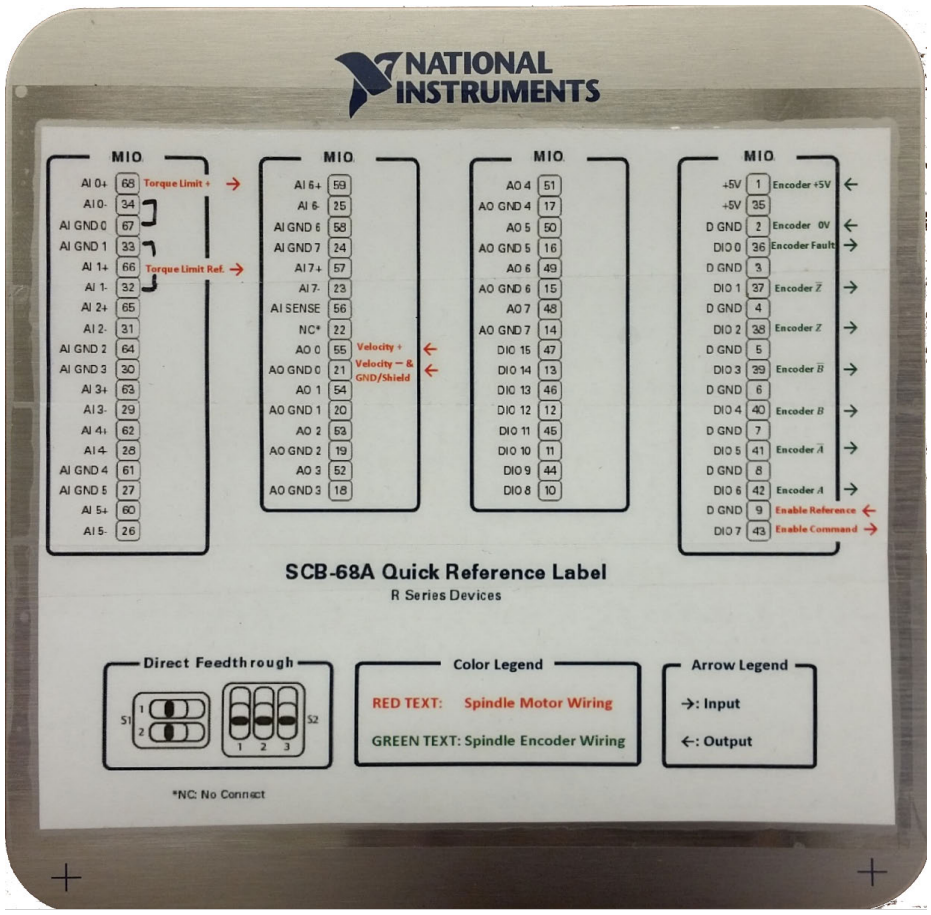

Figure B-11: Wiring diagram for breakout box connecting the controller to the spindle's amplifier and motor.

B.2 Air Supply Plumbing

Refrigerated Air Dryer Plumbing

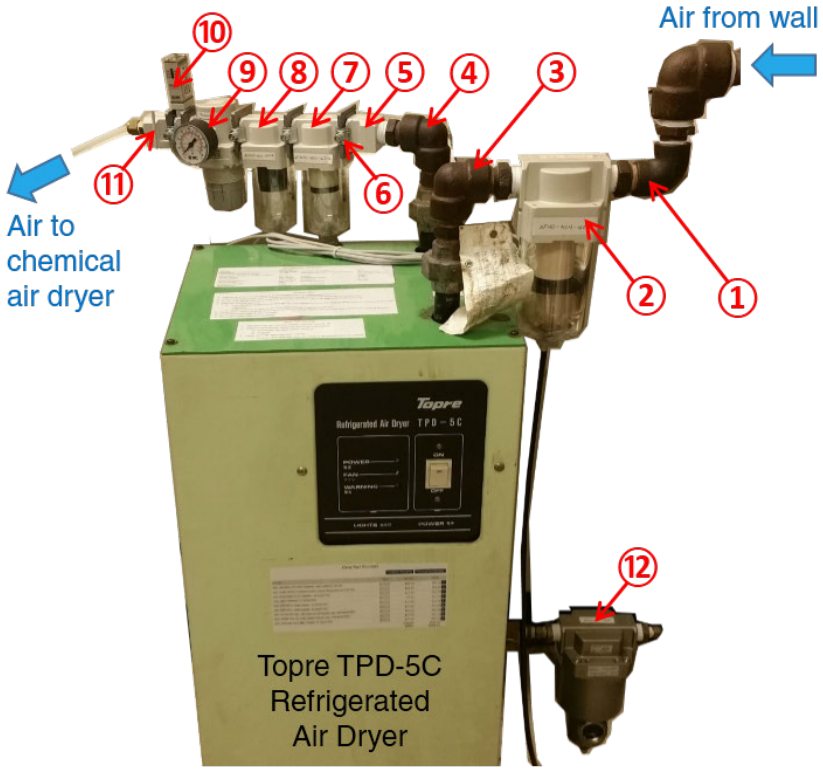

No.	*Part*	*Part No.*	*Notes*
1	1/2 in. NPT elbow		
2	Main line filter	AF40-N04-WZ-A	3 μm filter
3	1/2 in. NPT elbow		
4	1/2 in. NPT elbow		
5	1/2 in. NPT piping adapter	E300-N04-A	For refrigerated dryer connection
6	Component interfaces†	Y300-A	Connects filters together
7	Mist separator	AFM30-N03-WZ-A	0.3 μm filter
8	Micro mist separator	AFD30-N03-WZ-A	0.01 μm filter
9	Pressure regulator	AR30-N03G-NYZ-A	
10	Pressure switch	IS10M-30-6LP-A	0.2 - 0.6 MPa range
11	1/4 in. NPT piping adapter	E300-N02-A	For chemical dryer connection
12	Water separator	AMG350C-N04	Collects water from dryer

† A component interface is used between parts 5,7-11 each.

Figure B-12: Plumbing for the Topre TPD-5C refrigerated air dryer.

Chemical Air Dryer Plumbing

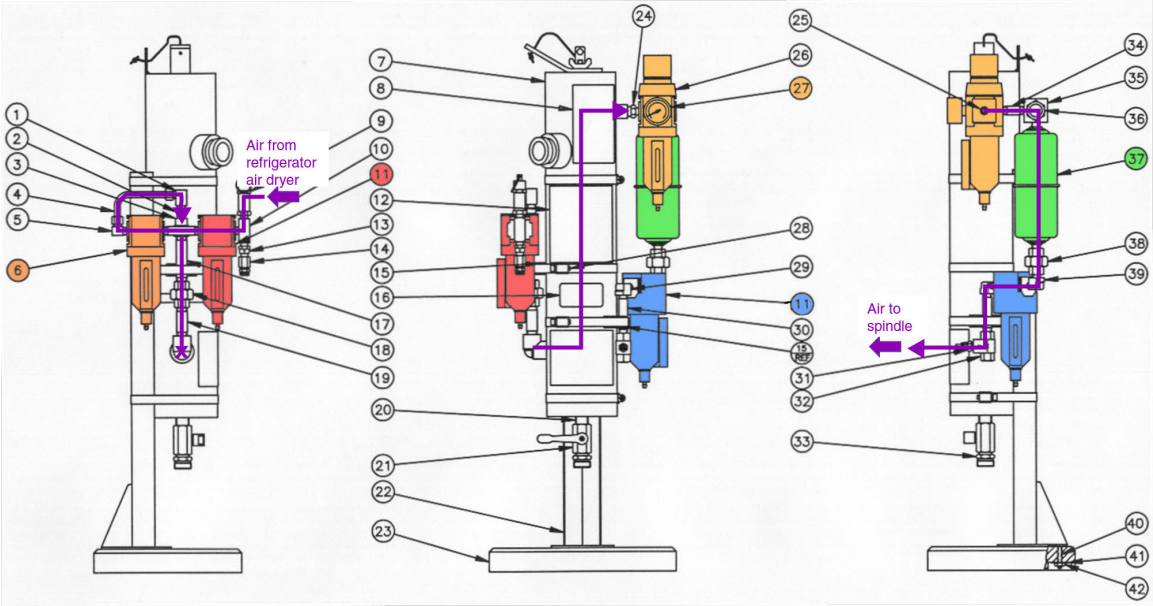

No.	*Part*	*Model*	*Notes*
11	Particulate filters	F16-02-00A-B91	5 μm filter
6	Coalescing filter	M16-02-000-A91	0.3 μm filter
27	Filter/regulator	CB6-02-012A-E91	5 μm filter
37	Activated carbon filter	Junior King	0.5 μm filter

Figure B-13: Plumbing for the D4-A chemical air dryer. Adapted from [39].

Appendix C

Debugging Drive Electronics

Though not discussed in this thesis, the electrode arrays' high frequency drive electronics needed significant debugging. This appendix presents considerations made and techniques found for debugging the electrode arrays' high frequency drive electronics as these considerations and techniques can be used for designing and debugging future high frequency circuits. First, considerations for high frequency oscilloscope measurements are discussed. Then debugging techniques are presented.

C.1 High Frequency Oscilloscope Measurement Considerations

While debugging high frequency circuits with an oscilloscope, one should check:

1. The size of probe's ground attachment.

2. Whether the probes used are active or passive.

3. The additional loading of the circuit caused by the probe.

4. The compensation of the probe.

5. The coupling of the probe.

Only considerations 1 & 5 are discussed further here. For more information on making high frequency oscilloscope measurements, [40, 41] are suggested readings.

As shown in Figure C-1, two common types of ground attachments for a single ended probe are a ground lead clip and tip and a ground spring. In applications where stay capacitances and inductances can greatly affect a circuit, such as a high frequency circuit, a ground spring should be used.

Oscilloscope probes can couple to outside noise. To reduce this noise in measurements, the probe can be wrapped around a ferrite core as shown in Figure C-2.

C.2 Debugging Techniques

To debug high frequency circuits, two techniques are particularly useful. Fist, the circuit can be mocked up above a copper clad board. The electrode arrays' high frequency drive electronics were prototyped with this method as shown in Figure C-3. The sheet of copper clad serves as a ground plane. This reduces the size of stray loops for components near the copper sheet. Second, a chunk of ferrite can be used to find the source of oscillations if the circuit is oscillating. When the ferrite approaches components in the oscillating loop of the circuit, that oscillating loop's inductance will increase. This will cause the frequency of the oscillations to change slightly, which can be detected by an oscilloscope. This technique is displayed in Figure C-4.

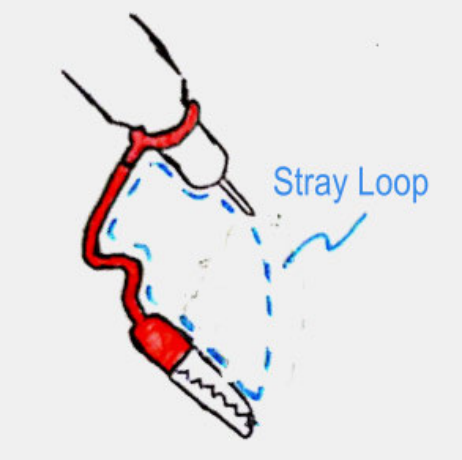

(a) Using a ground lead clip and tip produces significant stray inductance and capacitance.

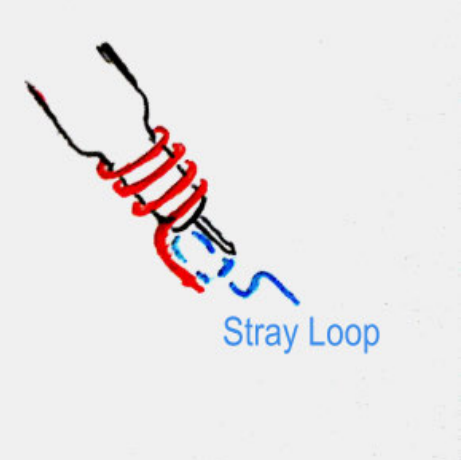

(b) Using a ground spring greatly reduces stray inductance and capacitance.

Figure C-1: Size of stray elements produced by the ground attachment of an oscilloscope probe. The smaller the stray loop, the less sensitive the measurement will be to outside noise and the cleaner dynamics it will have.

Figure C-2: Wrapping an oscilloscope probe around a ferrite core can further reduce outside noise picked up.

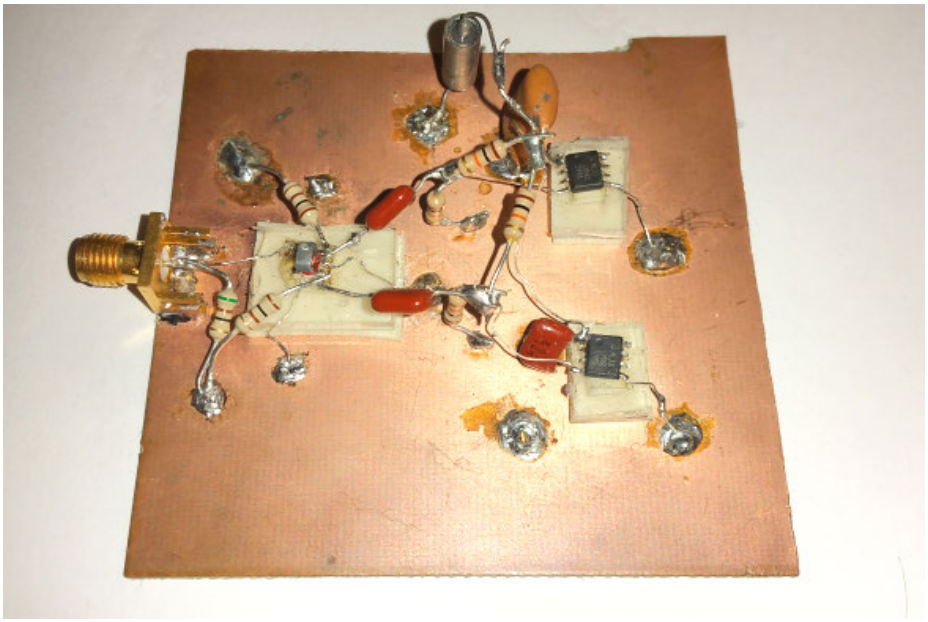

Figure C-3: Mock up board for the electrode array drive electronics. The sheet of copper clad below the components reduces stray loops.

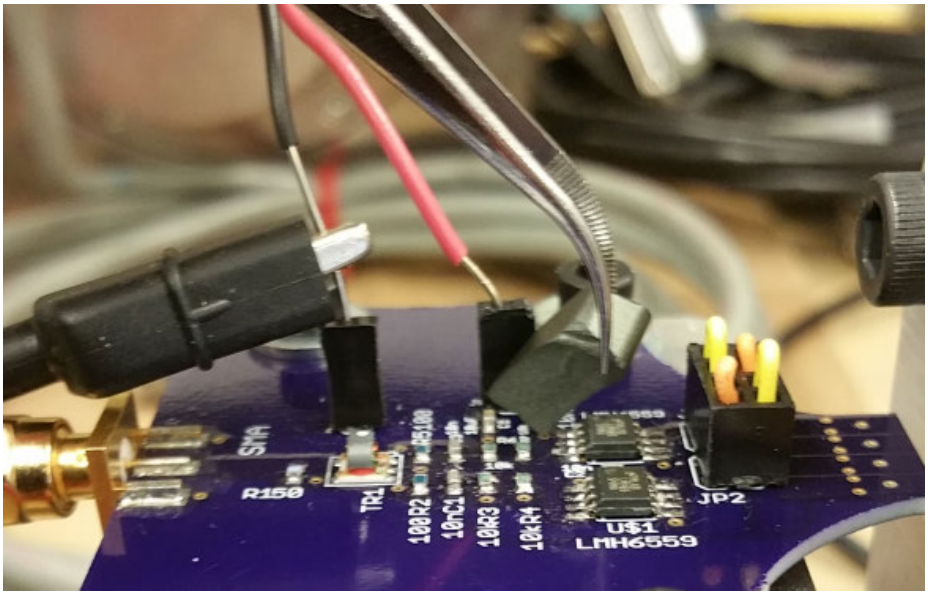

Figure C-4: A chunk of ferrite can be used to find an oscillating loop in a circuit. When the ferrite comes close a component in the oscillating loop, the inductance of the loop increases. This changes the oscillating loop's frequency by a small, but notable amount.